Czech Technical University in Prague
Faculty of Nuclear Sciences and Physical Engineering

**Department of Physical Electronics**
**Study program: Physical Electronics, spec. Computational physics**

# Model rozšířené magnetohydrodynamiky v kódu FLASH - testování a aplikace

# Model of extended magnetohydrodynamics in the FLASH code - testing and application

MASTER'S THESIS

| | |
|---|---|
| Author: | Bc. Jiří Löffelmann |
| Supervisor: | prof. Ing. Jiří Limpouch, CSc. |
| Consultant: | prof. Ing. Richard Liska, CSc. |
| Year: | 2024 |

ČESKÉ VYSOKÉ UČENÍ TECHNICKÉ V PRAZE
FAKULTA JADERNÁ A FYZIKÁLNĚ INŽENÝRSKÁ
*Katedra fyzikální elektroniky*

# ZADÁNÍ DIPLOMOVÉ PRÁCE

| | |
|---|---|
| *Student:* | **Bc. Jiří L ö f f e l m a n n** |
| *Studijní program:* | **Fyzikální elektronika** |
| *Specializace:* | **Počítačová fyzika** |
| *Akademický rok:* | **2022/2023** |
| *Název práce: (česky)* | **Model rozšířené magnetohydrodynamiky v kódu FLASH - testování a aplikace** |
| *Název práce: (anglicky)* | **Model of extended magnetohydrodynamics in the FLASH code - testing and application** |
| *Jazyk práce:* | **Angličtina** |

*Cíl práce:*

V nejnovější verzi výpočetního kódu FLASH je poprvé implementován model rozšířené magnetohydrodynamiky. Tento model umožňuje realisticky modelovat interakci laserového záření s plazmatem v silném vnějším i indukovaném magnetickém poli. Cílem diplomové práce je naučit s modelem zacházet, ověřit jeho funkčnost pomocí vhodně zvolených testů a použít ho pro vybrané simulace interakcí.

*Pokyny pro vypracování*

1. Prostudujte popis plazmatu v přiblížení rozšířené magnetohydrodynamiky (E-MHD). Seznamte se s modely anizotropního tepelného transportu. Seznamte se se zobecněnou rovnicí pro vývoj magnetického pole.
2. Seznamte se s implementací rozšířené magnetohydrodynamiky do kódu FLASH [1]. Vyzkoušejte jeho funkčnost na vhodně zvolených testovacích příkladech.
3. Pomocí kódu FLASH proveďte vybrané simulace interakce laserového záření s terči v indukovaném a v externím magnetickém poli.

*Doporučená literatura:*


1. FLASH User's Guide Version 4.7. Flash Center for Computational Science, University of Rochester, Dec 2022.
2. C. Walsh, J. Sadler, J. R. Davies, Updated magnetized transport coefficients: impact on laser-plasmas with self-generated or applied magnetic fields, Nucl. Fusion 61 (2021) 116025.
3. J. Sadler, C. A. Walsh, H. Li, Symmetric Set of Transport Coefficients for Collisional Magnetized Plasma, Phys. Rev. Lett. 126 (2021) 075001.
4. J. R. Davies, H. Wen, J. Y. Ji, E. D. Held, Transport coefficients for magnetic-field evolution in inviscid magnetohydrodynamics, Phys. Plasmas 28 (2021) 012305.
5. H. C. Watkins, R. J. Kingham, Magnetised thermal self-focusing and filamentation of long-pulse lasers in plasmas relevant to magnetised ICF experiments, Phys. Plasmas 25 (2018) 092701.
6. C. A. Walsh, J. P. Chittenden, D. W. Hilll, C. Ridgers, Extended-magnetohydrodynamics in under-dense plasmas, Phys. Plasmas 27 (2020) 022103.



*Jméno a pracoviště vedoucího práce:*

**prof. Ing. Jiří Limpouch, CSc.**
Katedra fyzikální elektroniky, Fakulta jaderná a fyzikálně inženýrská ČVUT v Praze

*Jméno a pracoviště konzultanta:*

**prof. Ing. Richard Liska, CSc.**
Katedra fyzikální elektroniky, Fakulta jaderná a fyzikálně inženýrská ČVUT v Praze


*Datum zadání:* 21. březen 2023

*Datum odevzdání:* leden 2024

Doba platnosti zadání je dva roky od data zadání.

.....

*Garant programu*

.....

*Vedoucí katedry*

.....

*Děkan*

ČESKÉ VYSOKÉ UČENÍ TECHNICKÉ V PRAZE Fakulta jaderná a fyzikálně inženýrská -3-

V Praze dne 21.3.2023

**Prohlášení**

Prohlašuji, že jsem svoji diplomovou práci vypracoval samostatně a použil jsem pouze podklady (literaturu, projekty, SW atd.) uvedené v přiloženém seznamu.

V Praze dne 8. 1. 2024 .....

.....
Bc. Jiří Löffelmann

**Acknowledgements**

I would like to express my gratitude to my supervisor prof. Ing. Jiří Limpouch, CSc. for kind and patient guidance and to my consultant prof. Ing. Richard Liska, CSc. for helpful suggestions.

Bc. Jiří Löffelmann

Název práce:
**Model rozšířené magnetohydrodynamiky v kódu FLASH - testování a aplikace**

Autor: Bc. Jiří Löffelmann

Studijní program: Fyzikální elektronika
Specializace: Počítačová fyzika
Druh práce: Diplomová práce

Vedoucí práce: prof. Ing. Jiří Limpouch, CSc.
Katedra fyzikální elektroniky, Fakulta jaderná a fyzikálně inženýrská, České vysoké učení technické v Praze

Konzultant: prof. Ing. Richard Liska, CSc.
Katedra fyzikální elektroniky, Fakulta jaderná a fyzikálně inženýrská, České vysoké učení technické v Praze

Abstrakt:
V této práci jsou provedeny simulace laserového plazmatu pomocí rozšířeného magnetohydrodynamického modelu (ExMHD). K numerickým simulacím interakcí mezi laserového záření s terčem ve vnějším magnetickém poli je použit kód FLASH. Je posouzen vliv a fyzikální význam jednotlivých procesů zahrnutých v modelu ExMHD. Modely transportu magnetizovaného plazmatu jsou důkladně prostudovány simulacemi jednotlivých jevů. Je představeno numerické schéma, založené na metodě konečných prvků, pro Nernstův efekt a je zkoumána vazba mezi termoelektrickými členy. Do ExMHD modelu je přidán proud horkých elektronů, který vede k vybuzení magnetického pole na čele plazmatické koróny. Toto pole je porovnáno se spontánním magnetickým polem vyvolaným Biermannovým efektem.
Klíčová slova: kód FLASH, laserové plazma, rozšírená MHD, zmagnetizované laserové plasma, externí magnetické pole

Title:
**Model of extended magnetohydrodynamics in the FLASH code - testing and application**

Abstract:
In this thesis, various simulations of laser-produced plasma are performed using the extended magnetohydrodynamic (ExMHD) model. The FLASH code is utilized to perform numerical simulations of laser-target interactions in an external magnetic field. The impact and physical meaning of individual effects included in the ExMHD is assessed. The magnetized plasma transport models are studied thoroughly in simulations focusing on single phenomena. A finite element numerical scheme for the Nernst effect is presented and coupling between the thermoelectric contributions is examined. Hot electron current is added into the ExMHD model, which leads to the generation of an angular magnetic field at the plasma corona front. This field is compared to the cross-gradient magnetic field induced by the Biermann effect.
Key words: FLASH code, laser-produced plasma, extended MHD, magnetized laser plasma, external magnetic field

# Nomenclature

| | |
|---|---|
| **MHD** | Magnetohydrodynamics |
| **1D** | one-dimensional |
| **2D** | two-dimensional |
| **3D** | three-dimensional |
| **FWHM** | Full width at half maximum |
| **CGS** | centimetre-gram-second |
| **ICF** | Inertial confinement fusion |
| **LHS** | Left-hand side |
| **RHS** | Right-hand side |
| **LTE** | local thermodynamic equilibrium |
| **QEOS** | Quotidian equation of state |
| **ExMHD** | Extended magnetohydrodynamics |
| **PIC** | Particle-in-Cell |
| **EOS** | Equation of state |
| **MFEM** | Modular finite element methods |
| **RK2** | Runge Kutta second order |

# Contents

# Introduction

Understanding the complex plasma dynamics is essential for a wide range of scientific and technological applications, including ICF. the pursuit of controlled nuclear fusion through the intense heating and compression of a fuel pellet using high-energy lasers. Numerical simulations play a crucial role in unravelling the intricate behaviour of plasmas. These simulations, based on fundamental physical principles, allow researchers to model and predict plasma dynamics under various conditions, providing invaluable insights for optimizing ICF and other plasma-related applications. ICF aims to replicate the conditions of nuclear fusion, the process that drives the sun and stars. It uses powerful lasers to heat and compress a small fuel capsule [1] to temperatures and pressures exceeding those found within the solar core. This promising path for achieving controlled nuclear fusion relies on the precise manipulation of high-energy lasers to compress and heat a target, initiating fusion reactions. The pursuit of sustainable and efficient fusion has led to a keen interest in optimizing ICF through a deep understanding of the underlying plasma dynamics. The intense energy released during fusion could potentially provide a clean and sustainable source of energy in the future.

As plasma dynamics is very complex, there is no general model that describes plasma in any condition. Instead, there are many different physical descriptions of plasma which are best applicable to distinct problems and plasma properties. They range from particle and kinetic to fluid models and describe the plasma on different space and time scales. In this work, we focus on the fluid description of plasma that provides knowledge about the global behaviour of plasma at large scales. For this reason, it is commonly used for plasma ablation from laser-heated targets [2] or for modelling astrophysical objects as stars and nebulas [3].

Magnetohydrodynamics (MHD) is a widely used framework for modelling plasma dynamics in a variety of conditions. It combines the principles of fluid dynamics with electromagnetic phenomena to describe the collective behaviour of plasmas [4]. MHD simulations have been instrumental in understanding and predicting plasma behaviour in ICF experiments and astrophysical phenomena. Moreover, this model is commonly used for studying laser-target interaction problems, for example, observation of strong self-generating magnetic fields [5] that are created during laser-target interaction or various instabilities [6, 7] that can substantially change the dynamics of laser plasma.

The recent experimental findings have underscored the potential of external magnetic fields in prolonging the confinement time. It has been experimentally and numerically shown that magnetic fields can significantly impact plasma behaviour, influencing plasma confinement [8], heat transport [9], and the formation of instabilities [10]. The idea of combining inertial and magnetic confinement is also being researched in a recent field of magneto-inertial fusion [11]. New methods [12] allow the creation of such a strong field that can be applied to laser-target interaction.

This thesis focuses on advancing our understanding of plasma dynamics through numerical simulations of laser-target interaction. The implementation of a hot electron model, an extension of the MHD model with thermoelectric terms, and simulations of laser target interactions in external magnetic fields form the core of our investigation. Moreover, the thermal and electrical conductivity models are modified to better handle the multi-phase nature of the laser-target interaction problem. We perform numerical simulation using multiphysics code FLASH [13], in which the extended magnetohydrodynamic (ExMHD) model [9] was just recently implemented. This simulation code solves differential equations on static mesh (Eulerian approach), using a finite-volume Godunov-type scheme [14]. It also includes a framework for laser-target simulations, making it a suitable option for studying laser plasma dynamics described by the ExMHD model. Through these explorations, this thesis aims to contribute valuable insights to the field of plasma physics, with implications for controlled nuclear fusion.

This thesis is organized as follows: in Chapter 1 the relevant literature is reviewed and the equations of the ExMHD model are described in detail. Chapter 2 explains the limitations of the model and conditions under which this description of plasma is applicable with reasonable accuracy. Two discussions of the numerical aspect of ExMHD model are discussed in Chapter 3. Chapter 4 shows different physical models of plasma, which are essential for obtaining a complete model of laser plasma, with the addition of the hot electron model. Finally, Chapter 5 presents simulation results together with a detailed analysis of the acquired numerical results with conclusions and suggestions for future work.

All equations presented in this thesis are in Gaussian CGS units. For temperature, we adopt commonly used unit eV for presentation of results and unit K in the theoretical part of this thesis. Laser intensity (irradiance) is in unit $\mathrm{W\,cm^{-2}}$.

# Chapter 1

# Extended magnetohydrodynamics

In this chapter the ExMHD model of magnetized collisional plasma is described in detail. The usual derivation of the fluid equations is introduced. This derivation is focused on stressing the assumptions and approximations that are made to arrive at magnetohydrodynamic model equations from the exact kinetic theory of plasma. Consequently, the extension of MHD model is introduced. It was derived by Braginskii [15] decades ago in a similar form, but only recently the numerically correct model of the transport coefficients was constructed [16, 17, 18]. Previously, the concrete extended MHD model that was commonly adopted was the one formulated by Braginskii or by Epperlein and Haines [19]. Both of these include fits of the transport coefficients to kinetic calculations but gave incorrect results for small magnetic fields [20, 18]. This is explained in more detail in Section 1.5.

For simplicity, viscosity is not considered in this work, although it affects the evolution of magnetic field and plasma. Moreover, constant ionization and an ideal gas equation of state are assumed in the derivation. Finally, in order to simplify the description and to focus mainly on the influence of magnetic field on plasma dynamics through the new terms in ExMHD model, radiation is not considered.

## 1.1 Kinetic theory and moment equations

In the kinetic theory, the plasma state is described by distribution function $f_a(t, \boldsymbol{r}, \boldsymbol{v})$ defined for each particle species (with different ionizations or masses), where $\boldsymbol{r}$ is position, $\boldsymbol{v}$ is velocity and $t$ is time. The evolution of this distribution function is given by the Boltzmann equation:

$$\frac{\partial f_a}{\partial t} + \nabla_{\boldsymbol{x}} \cdot (f_a \boldsymbol{v}) + \nabla_{\boldsymbol{v}} \cdot \left( \frac{f_a e_a}{m_a} \left( \boldsymbol{E} + \frac{1}{c} \boldsymbol{v} \times \boldsymbol{B} \right) \right) = C_a, \tag{1.1}$$

where $e_a$ is charge and $m_a$ is mass of the particle species $a$, $\boldsymbol{E}$ represent electric field, $\boldsymbol{B}$ represent magnetic field, $c$ is speed of light and lastly $C_a$ includes all collisional effects. The description of collisions in plasma is very complex and usually includes many approximations even in the kinetic form (Fokker-Planck equation). The kinetic theory assumes smooth distribution, the electric and magnetic fields are averaged over a large number of particles in considered macroscopic volume. This description is the foundation for kinetic numerical methods, for example, Vlasov or particle-in-cell (PIC) code [21]. They provide higher precision at higher computational cost and therefore in practice are applicable on small time and space scales. Kinetic

methods are adopted for instance in simulations of charged particle acceleration [22] or atomistic processes like ionization dynamics [23].

The goal of the fluid model is to describe plasma using macroscopic quantities such as density, velocity and internal energy. The prescriptions of the time evolution of these quantities are derived by integrating the Boltzmann equation [24]. The resulting relations are in the form of moment equations (conservations of mass, momentum and energy) for a species of type $a$:

$$\frac{\partial\left(m_a n_a\right)}{\partial t}+\nabla\cdot\left(m_a n_a \boldsymbol{V}_a\right)=0, \tag{1.2a}$$

$$\frac{\partial\left(m_a n_a \boldsymbol{V}_a\right)}{\partial t}+\nabla\cdot\left(m_a n_a \boldsymbol{V}_a\boldsymbol{V}_a\right)+\nabla\cdot\underline{\underline{P_a}}=e_a n_a\left(\boldsymbol{E}+\frac{1}{c}\boldsymbol{V}_a\times\boldsymbol{B}\right)+\boldsymbol{R}_a, \tag{1.2b}$$

$$\frac{\partial\left(\frac{1}{2}m_a n_a \boldsymbol{V}_a^2+\frac{3}{2}n_a k_B T_a\right)}{\partial t}+\nabla\cdot\left(\left(\frac{1}{2}m_a n_a \boldsymbol{V}_a^2+\frac{3}{2}n_a k_B T_a+\underline{\underline{P_a}}\right)\boldsymbol{V}_a+\boldsymbol{q}_a\right)= \\ =e_a n_a \boldsymbol{E}\cdot\boldsymbol{V}_a+\boldsymbol{R}_a\cdot\boldsymbol{V}_a+Q_a, \tag{1.2c}$$

where $m_a$ is mass, $n_a$ is number density, $\boldsymbol{V}_a$ is fluid velocity, $\underline{\underline{P_a}}$ is pressure tensor, $\boldsymbol{R}_a$ represents mean change of momentum of particles of species $a$ due to collisions with other particles (further called *collision force*), $T_a$ is temperature, $\boldsymbol{q}_a$ is heat flux density, $Q_a$ stands for mean change of internal energy of particle species $a$ due to collisions with other particles. The term $\boldsymbol{V}_a\boldsymbol{V}_a$ denotes the tensor product of two vectors ($\boldsymbol{V}_a\otimes\boldsymbol{V}_a$), but the operator sign is omitted here. This notation for the tensor product is used in the whole thesis.

Temperature is defined for collisional plasma in local thermal equilibrium (LTE) proportional to particles velocity variations: $k_B T_a=\frac{m_a}{3}\langle(v-V_a)^2\rangle$, where $k_B$ is Boltzmann constant. The pressure tensor can be simplified using the so-called Chapman-Enskog procedure [25] that separates the isotropic part of the tensor (scalar pressure) and viscosity tensor:

$$\underline{\underline{P_a}}=P_a\underline{\underline{I}}+\underline{\underline{\pi_a}}, \tag{1.3}$$

where $\underline{\underline{I}}$ is identity tensor. In further derivations and also in performed simulations, the viscosity term $\underline{\underline{\pi_a}}$ is neglected. This approach is commonly adapted to simplify the fluid model and justified for strongly collisional plasma [26].

Multiplying the equation (1.2b) by $\boldsymbol{V}_a$ and using equation (1.2a), gives an equation for the evolution of kinetic energy of particle species $a$:

$$\frac{\partial\left(\frac{1}{2}m_a n_a \boldsymbol{V}_a^2\right)}{\partial t}+\nabla\cdot\left(\frac{1}{2}m_a n_a \boldsymbol{V}_a^2\boldsymbol{V}_a\right)+\boldsymbol{V}_a\cdot\nabla P_a=e_a n_a\boldsymbol{E}\cdot\boldsymbol{V}_a+\boldsymbol{R}_a\cdot\boldsymbol{V}_a. \tag{1.4}$$

By subtracting equation (1.4) from (1.2c) the evolution of internal energy is obtained:

$$\frac{\partial\varepsilon_a}{\partial t}+\nabla\cdot\left(\varepsilon_a\boldsymbol{V}_a+\boldsymbol{q}_a\right)+P_a\nabla\cdot\boldsymbol{V}_a=Q_a, \tag{1.5}$$

where $\varepsilon_a = \frac{3}{2} n_a k_B T_a$ is internal energy density of the species $a$. The equations (1.2) form a multi-fluid model. In this model, the motion of electrons and ions are separate. This allows one to model more complex physical phenomena such as the decoupling of electron and ion motion, and various anisotropic effects [27]. Compared to the mono-fluid model, described in the following section, multi-fluid methods need to adopt small time steps as charge separation produces plasma waves of high frequency.

## 1.2 Derivation of extended-MHD model

In this section, the final form of the extended MHD model is derived from the moment equations presented in the previous section. The derivation is done by summing over all particle species and introducing averaged physical quantities:

$$\rho = \sum_a m_a n_a, \quad \boldsymbol{V} = \frac{\sum_a m_a n_a \boldsymbol{V}_a}{\sum_a m_a n_a}, \quad P = \sum_a P_a, \tag{1.6}$$

$$\boldsymbol{j} = \sum_a e_a n_a \boldsymbol{V}_a, \quad \rho_c = \sum_a e_a n_a, \tag{1.7}$$

where $\rho$ is fluid density, $\boldsymbol{V}$ is fluid velocity, $P$ is scalar pressure, $\boldsymbol{j}$ is current density and $\rho_c$ is charge density. The last equation in (1.6) is not generally correct as the pressure tensor is defined using the average (fluid) velocity of one population and that average can differ between multiple populations. Nevertheless, because of the collisional plasma assumption, all populations have velocities close to fluid velocity $\boldsymbol{V}$ and this approximation of total pressure in (1.6) is valid [26].

Further, constant ionization is assumed for simplicity. It corresponds to considering plasma with species of only two types: electrons $e$ and ions $i$. The assumption is valid in high-temperature plasmas. Additionally, relations $n_e = Z n_i$ (for *quasi-neutral* plasma) and $e_i = -Z e_e$ hold. Here $e_e = -e$ stands for electron charge, where $e$ is the elementary charge, and $Z$ is the ionization number. Moreover, the notation $\boldsymbol{u} = \boldsymbol{V}_e - \boldsymbol{V}_i$ is used, which implies $\boldsymbol{j} = -e n_e \boldsymbol{u}$. By summing each equation in (1.2) over species $e, i$, following set of equations is obtained:

$$\frac{\partial \rho}{\partial t} + \nabla \cdot (\rho \boldsymbol{V}) = 0, \tag{1.8a}$$

$$\frac{\partial (\rho \boldsymbol{V})}{\partial t} + \nabla \cdot (\rho \boldsymbol{V} \boldsymbol{V}_i + m_e n_e \boldsymbol{V}_e \boldsymbol{u}) + \nabla P = \rho_c \boldsymbol{E} + \frac{1}{c} \boldsymbol{j} \times \boldsymbol{B}, \tag{1.8b}$$

$$\frac{\partial \mathcal{E}}{\partial t} + \nabla \cdot \left( (\mathcal{E} + P) \boldsymbol{V}_i + \boldsymbol{q} + (\mathcal{E}_e + P_e) \boldsymbol{u} \right) = \boldsymbol{E} \cdot \boldsymbol{j}, \tag{1.8c}$$

where $\mathcal{E}_e = \varepsilon_e^{kin} + \varepsilon_e^{int} = \frac{1}{2} m_e n_e \boldsymbol{V}_e^2 + \frac{3}{2} n_e k_B T_e$, $\mathcal{E} = \mathcal{E}_e + \mathcal{E}_i$ and $\boldsymbol{q} = \boldsymbol{q}_e + \boldsymbol{q}_i$. Similarly,

summation of equation (1.4) and (1.5) over species $e, i$, gives:

$$\frac{\partial \varepsilon^{kin}}{\partial t} + \nabla \cdot \left(\varepsilon^{kin}\boldsymbol{V}_i + \varepsilon_e^{kin}\boldsymbol{u}\right) + \boldsymbol{V}_i \cdot \nabla P + \boldsymbol{u} \cdot \nabla P_e = \boldsymbol{E} \cdot \boldsymbol{j} + \boldsymbol{R}_e \cdot \boldsymbol{u}, \tag{1.9}$$

$$\frac{\partial \varepsilon^{int}}{\partial t} + \nabla \cdot \left(\varepsilon^{int}\boldsymbol{V}_i + \left(\varepsilon_e^{int} + P_e\right)\boldsymbol{u} + \boldsymbol{q}\right) + P\nabla \cdot \boldsymbol{V}_i - \boldsymbol{u} \cdot \nabla P_e = -\boldsymbol{R}_e \cdot \boldsymbol{u}, \tag{1.10}$$

where $\varepsilon^{kin} = \varepsilon_e^{kin} + \varepsilon_i^{kin} = \frac{1}{2}m_e n_e \boldsymbol{V}_e^2 + \frac{1}{2}m_i n_i \boldsymbol{V}_i^2$. The goal is to arrive at a set of mono-fluid equations, therefore, $\boldsymbol{V}_e$ needs to be eliminated from the equations. This can be achieved by exploiting the fact that electron mass is small compared to ion mass $m_e \ll m_i \implies \boldsymbol{V}_i \approx \boldsymbol{V} \implies \boldsymbol{V}_e \approx \boldsymbol{u} + \boldsymbol{V}$. The electron inertia term $(\nabla \cdot (m_e n_e \boldsymbol{V}_e \boldsymbol{u}))$ in equation (1.8b) can be neglected when compared to ion inertia. Equivalently, the term $\nabla \cdot \left(\varepsilon_e^{kin}\boldsymbol{u}\right)$ in (1.9) is small compared to the term containing total kinetic energy. Moreover, for quasi-neutral plasma, the charge density is $\rho_c \approx 0$.

Before presenting the conservation equations in final form, relations for electric $\boldsymbol{E}$ and magnetic $\boldsymbol{B}$ fields, together with relation for current density $\boldsymbol{j}$, are introduced. When using mono-fluid equations, one has only information about mean fluid velocity and it is not possible to calculate current density directly. Electric and magnetic fields are governed by Maxwell's equations:

$$\nabla \cdot \boldsymbol{E} = \rho_c, \quad \nabla \times \boldsymbol{E} = -\frac{1}{c}\frac{\partial \boldsymbol{B}}{\partial t}, \tag{1.11}$$

$$\nabla \cdot \boldsymbol{B} = 0, \quad \nabla \times \boldsymbol{B} = \frac{4\pi}{c}\boldsymbol{j} + \frac{1}{c}\frac{\partial \boldsymbol{E}}{\partial t}. \tag{1.12}$$

In the non-relativistic limit, the displacement current in the Maxwell-Ampère's equation in (1.12) can be neglected (electromagnetic field is instantaneously at equilibrium) [26]. That also implies $\nabla \cdot \boldsymbol{j} = 0$, as $\nabla \cdot \nabla \times \boldsymbol{F} = 0$ holds for any vector field $\boldsymbol{F}$. Then, the charge continuity equation:

$$\frac{\partial \rho_c}{\partial t} + \nabla \cdot \boldsymbol{j} = 0, \tag{1.13}$$

implies stationary charge distribution. Therefore, plasma remains in a quasi-neutral state and $\rho_c \approx 0$. The second equation in (1.11) prescribes the time evolution of the magnetic field. Equations (1.12) state divergence-free conditions for magnetic field and the second equation can be used to calculate current density.

Contrary to the usual approach, the electric field cannot be calculated from Poisson's equation as plasma has a tendency to remain close to a neutral charge state. This problem is typically resolved by deriving *generalized Ohm's equation* from the second moment equation for ions and electrons (usually done for fully ionized plasma [24, 28] and ionization is then treated for the transport coefficients). In this thesis, a different line of reasoning, which leads to the same equation for the electric field, is used. It is demonstrated that this form of the electric field is consistent with approximations that give final mono-fluid conservation equations.

Applying all the described approximations, the following two temperature mono-fluid conservation equations of laser plasma are obtained:

$$\frac{\partial \rho}{\partial t} + \nabla \cdot (\rho \boldsymbol{V}) = 0, \tag{1.14a}$$

$$\frac{\partial (\rho \boldsymbol{V})}{\partial t} + \nabla \cdot (\rho \boldsymbol{V}\boldsymbol{V}) + \nabla P = \frac{1}{c}\boldsymbol{j} \times \boldsymbol{B}, \tag{1.14b}$$

$$\frac{\partial \mathcal{E}}{\partial t} + \nabla \cdot \left( (\mathcal{E} + P)\, \boldsymbol{V} + \boldsymbol{q} + \left(\varepsilon_e^{int} + P_e\right) \boldsymbol{u} \right) = \boldsymbol{E} \cdot \boldsymbol{j}, \tag{1.14c}$$

which are supplemented with equations for kinetic and internal energy:

$$\frac{\partial \varepsilon^{kin}}{\partial t} + \nabla \cdot \left( \varepsilon^{kin} \boldsymbol{V} \right) + \boldsymbol{V} \cdot \nabla P + \boldsymbol{u} \cdot \nabla P_e = \boldsymbol{E} \cdot \boldsymbol{j} + \boldsymbol{R}_e \cdot \boldsymbol{u}, \tag{1.15}$$

$$\frac{\partial \varepsilon^{int}}{\partial t} + \nabla \cdot \left( \varepsilon^{int} \boldsymbol{V} + \left(\varepsilon_e^{int} + P_e\right) \boldsymbol{u} + \boldsymbol{q} \right) + P \nabla \cdot \boldsymbol{V} - \boldsymbol{u} \cdot \nabla P_e = -\boldsymbol{R}_e \cdot \boldsymbol{u}. \tag{1.16}$$

Two of the equations (1.14c), (1.15) and (1.16) are redundant.

Multiplying the equation (1.14b) by $\boldsymbol{V}$, one obtains the time evolution of kinetic energy of the fluid:

$$\frac{\partial \left( \frac{1}{2} \rho \boldsymbol{V}^2 \right)}{\partial t} + \nabla \cdot \left( \frac{1}{2} \rho \boldsymbol{V}^2 \boldsymbol{V} \right) + \boldsymbol{V} \cdot \nabla P = -\boldsymbol{j} \cdot \left( \frac{1}{c} \boldsymbol{V} \times \boldsymbol{B} \right). \tag{1.17}$$

If the approximation $\varepsilon^{kin} \approx \frac{1}{2} \rho \boldsymbol{V}^2$ is considered, the equations (1.15) and (1.17) are consistent for following form of electric field:

$$\boldsymbol{E} = -\frac{1}{c} \boldsymbol{V} \times \boldsymbol{B} + \frac{1}{e n_e c} \boldsymbol{j} \times \boldsymbol{B} - \frac{1}{e n_e} \nabla P_e + \frac{1}{e n_e} \boldsymbol{R}_e. \tag{1.18}$$

As was stated before, generalized Ohm's equation derived from the second moment equation leads to the equation of the same form as (1.18). For this electric field, equations (1.15) and (1.17) are equivalent and their sum is equal to the equation (1.14c).

## 1.3 Energy conservation

In this thesis, plasma created by heating of a solid target by an intense laser is assumed. The laser energy is absorbed in plasma by numerous mechanisms, although only inverse Bremsstrahlung is considered here (see Chapter 4). This inflow of energy into the system is indicated by adding $Q_L$ to the RHS of the equations (1.14c) and (1.16). The total energy in the system consists of the kinetic energy of the fluid, internal and magnetic field energy (in the non-relativistic case electric energy is negligible when compared to magnetic energy):

$$\mathcal{E}_{tot} = \frac{1}{2} \rho \boldsymbol{V}^2 + \varepsilon^{int} + \frac{1}{8\pi} \boldsymbol{B}^2, \tag{1.19}$$

where $\varepsilon^{int} = \frac{3}{2} n_e k_B T_e + \frac{3}{2} n_i k_B T_i$. The previous section presented a conservation equation for the first two energies. Magnetic energy evolution can be obtained by multiplying the induction equation in (1.11) by $\boldsymbol{B}$:

$$\frac{1}{8\pi}\frac{\partial \boldsymbol{B}^2}{\partial t} + \nabla \cdot \left(\frac{c}{4\pi}\boldsymbol{E} \times \boldsymbol{B}\right) = -\boldsymbol{j} \cdot \boldsymbol{E}. \tag{1.20}$$

The addition of equations (1.14c) and (1.20) gives total energy conservation equation:

$$\frac{\partial \mathcal{E}_{tot}}{\partial t} + \nabla \cdot \left(\left(\frac{1}{2}\rho \boldsymbol{V}^2 + \varepsilon^{int} + P\right)\boldsymbol{V} + \frac{c}{4\pi}\boldsymbol{E} \times \boldsymbol{B} + \boldsymbol{q} + \left(\varepsilon_e^{int} + P_e\right)\boldsymbol{u}\right) = Q_L. \tag{1.21}$$

This equation (in conservative form) shows that the system is conserving total energy with only the source of heating by laser.

Lastly, the energy transfer between different energy types is examined in more detail. By eliminating $\boldsymbol{E}$ from the energy conservation equations using Ohm's equation (1.18), the following equations are obtain ($\boldsymbol{E}$ in the Poynting vector on LHS of (1.20) is left for simplicity):

$$\frac{1}{2}\frac{\partial\left(\rho \boldsymbol{V}^2\right)}{\partial t} + \nabla \cdot \left(\frac{1}{2}\rho \boldsymbol{V}^2 \boldsymbol{V} + P\boldsymbol{V}\right) = P\nabla \cdot \boldsymbol{V} - \frac{1}{c}\boldsymbol{j} \cdot (\boldsymbol{V} \times \boldsymbol{B}), \tag{1.22a}$$

$$\frac{1}{8\pi}\frac{\partial \boldsymbol{B}^2}{\partial t} + \nabla \cdot \left(\frac{c}{4\pi}\boldsymbol{E} \times \boldsymbol{B}\right) = \frac{1}{c}\boldsymbol{j} \cdot (\boldsymbol{V} \times \boldsymbol{B}) + \frac{1}{en_e}\boldsymbol{j} \cdot (\nabla P_e - \boldsymbol{R}_e), \tag{1.22b}$$

$$\frac{\partial \varepsilon^{int}}{\partial t} + \nabla \cdot \left(\varepsilon^{int}\boldsymbol{V} + \frac{1}{en_e}\boldsymbol{j}\left(\varepsilon_e^{int} + P_e\right) + \boldsymbol{q}\right) = -P\nabla \cdot \boldsymbol{V} + \frac{1}{en_e}\boldsymbol{j} \cdot (-\nabla P_e + \boldsymbol{R}_e), \tag{1.22c}$$

where the substitution for $\boldsymbol{u} = \frac{1}{en_e}\boldsymbol{j}$ was used and the term $Q_L$ was omitted here. Looking at the RHS of equations (1.22), one can analyse how energy is transferred between its individual types. The kinetic and magnetic energies are exchanged via the action of magnetic force ($\boldsymbol{F}_m \sim \boldsymbol{V} \times \boldsymbol{B}$), whereas for the kinetic and internal energy the transfer happens through pressure dilatation (the term $P\nabla \cdot \boldsymbol{v}$) [29]. Finally, for the magnetic and internal energy, this is done by the action of electron pressure and collision forces (last two terms on RHS of equations (1.22b) and (1.22c)).

In laser plasma, energy relaxation times between ions $\tau_{ii}^E$ and between electrons and ions $\tau_{ei}^E$ are significantly higher than relaxation time between electrons $\tau_{ee}^E$ (about $\frac{m_i}{2m_e} \approx 10^3 - 10^4$ times higher) [30]. Additionally, laser energy is absorbed mostly by electron fluid, therefore electron and ion temperatures can be quite different and it is more reasonable to solve equations of electron and ion internal energy separately instead of equation (1.16):

$$\frac{\partial \varepsilon_e^{int}}{\partial t} + \nabla \cdot \left(\varepsilon_e^{int}\boldsymbol{V} + \left(\varepsilon_e^{int} + P_e\right)\boldsymbol{u} + \boldsymbol{q}_e\right) + P_e\nabla \cdot \boldsymbol{V} - \boldsymbol{u} \cdot \nabla P_e - \boldsymbol{R}_e \cdot \boldsymbol{u} = Q_L - Q_{ei}, \tag{1.23a}$$

$$\frac{\partial \varepsilon_i^{int}}{\partial t} + \nabla \cdot \left(\varepsilon_i^{int}\boldsymbol{V} + \boldsymbol{q}_i\right) + P_i\nabla \cdot \boldsymbol{V} = Q_{ei}, \tag{1.23b}$$

where $Q_{ei}$ is heat exchanged during collisions of electrons with ions and the term $\boldsymbol{R}_e \cdot \boldsymbol{u}$ in equation (1.23a) represents heat generated due to electron-ion collisions that result from ordered movement - electrical current in plasma. The term $\boldsymbol{R}_e \cdot \boldsymbol{u}$ in reality also contributes to the heating of ions, however, this contribution is about $\frac{m_e}{m_i}$ smaller and thus can be neglected [15]. In collisions, electrons lose a small part of their ordered velocity that is subsequently transferred into heat. This term is also referred to as *Ohm's heating*.

For the model equations to be solvable, the relations for pressure $P$, heat flux density $\boldsymbol{q}$, current density $\boldsymbol{j}$ and friction force $R_e$ need to be introduced. This is resolved by introducing approximated so-called *closure equations* that are usually derived from kinetic theory with the assumption of the local Maxwellian distribution of particle velocities or are motivated by experimental results and empirical theories.

## 1.4 Closure equations

In the MHD model, outlined in previous sections, the state of plasma is described by five physical quantities (moments of distribution $f_a$): density $\rho$, fluid velocity $\boldsymbol{V}$, electron and ion internal energies $\varepsilon_e^{int}$, $\varepsilon_i^{int}$ and magnetic field $\boldsymbol{B}$. The equations also include higher moments (heat fluxes $\boldsymbol{q}_e, \boldsymbol{q}_i$) and other quantities (pressure $P$, collisional force $R_e$, energy exchange $Q_{ei}$ and laser heat source $Q_L$) that need to be expressed in terms of the plasma state quantities. By achieving that, one obtains a complete set of solvable partial differential equations. In this section, it is described in detail how these quantities are usually approached and commonly used approximative relations are presented. The closure relations are essential in the fluid modelling of laser-produced plasmas and can significantly influence the plasma behaviour [31]. The discussion of the heat exchange and laser heat source can be found in Chapter 4.

Firstly, the relations between pressure, temperature and density are presented. This relationship is called *equation of state* (EOS) and its form is well known for different types of fluids. In this thesis, the ideal gas equation of state is adopted in the following form for electrons and ions:

$$P_e = \varepsilon_e^{int} (\gamma - 1), \quad P_i = \varepsilon_i^{int} (\gamma - 1), \tag{1.24}$$

where $\gamma$ is the ratio of specific heats. The ExMHD equations presented in previous sections did not include temperatures explicitly, but the electron temperature will appear in the collisional force term. For high plasma temperatures, the ideal gas equation of state is a good approximation for plasma. However, for high densities and lower temperatures, the quantum mechanical effect of degenerate electron gas becomes significant and a more complicated EOS needs to be adopted [32]. One of the most widely used EOS is SESAME. It is based on both theoretical models and experimental results and includes tabulated state functions for more than 150 different materials [33]. Another commonly used tabulated equation of state is

QEOS, which is funded on the Thomas-Fermi model and well-approximated plasma behaviour for wide ranges of temperatures and densities [34].

Transport equations, and thus relations for heat fluxes and collisional force, are derived from kinetic theory by many authors [35, 15, 36]. The validity of those derivations differs and they are accurate for different ionization, density and temperature ranges. The widely used relations are from [15] or [19]:

$$\boldsymbol{q}_e = \boldsymbol{q}_T^e + \boldsymbol{q}_{\boldsymbol{u}}^e = -\frac{n_e k_B T_e \tau_{ei}}{m_e} \underline{\underline{\kappa}} \cdot \nabla T_e - \frac{k_B T_e}{e} \underline{\underline{\beta}} \cdot \boldsymbol{j}, \tag{1.25a}$$

$$\boldsymbol{R}_e = \boldsymbol{R}_T + \boldsymbol{R}_{\boldsymbol{u}} = -\frac{k_B}{e} \underline{\underline{\beta}} \cdot \nabla T_e + \frac{m_e}{e^2 n_e \tau_{ei}} \underline{\underline{\alpha}} \cdot \boldsymbol{j}, \tag{1.25b}$$

where $\underline{\underline{\kappa}}, \underline{\underline{\beta}}$ and $\underline{\underline{\alpha}}$ are the so-called *transport coefficients* that are fitted to results of kinetic calculations as functions of ionization $Z$ and magnetization (Hall parameter):

$$\chi = \frac{e|\boldsymbol{B}|\tau_{ei}}{m_e c} = \omega_{ce}\tau_{ei}, \tag{1.26}$$

$\tau_{ei}$ is mean electron-ion collision time and $\omega_{ce}$ is electron cyclotron frequency.

The collisional force $\boldsymbol{R}_e$ consists of friction force $\boldsymbol{R}_{\boldsymbol{u}}$ and thermal force $\boldsymbol{R}_T$. The friction force results from ordered velocity $\boldsymbol{u}$ (electrical current $\boldsymbol{j}$). When electrons and ions move against each other with velocity $\boldsymbol{u}$, they collide in time $\sim \tau_{ei}$ and lose or gain their ordered velocity and consequently their momentum. The collision rate is higher for slower electrons than for faster electrons.

The thermal force is the consequence of temperature gradients together with dependence of collision frequency on temperature ($\tau_{ei} \sim v_{T_e}^3 \sim T_e^{3/2}$). Let's imagine electrons passing through a cross-section from left to right and from right to left along the magnetic field (or $\boldsymbol{B} = 0$). If electrons and ions are at rest $\boldsymbol{V_e} = \boldsymbol{V}_i = 0$, the number of electrons coming from left and right is approximately the same. Now, when electrons coming from the left have a higher average temperature, they experience smaller amount of collisions with ions compared to colder electrons coming from the right. This leads to the resultant net force in the direction of colder electrons ($\boldsymbol{R}_T \sim -\nabla T_e$).

The components of electron heat flux $\boldsymbol{q}_e$ are closely related to the components of the collisional force. This is known as a *principle of symmetry of the kinetic coefficients* (or the *Onsager principle*) [15]. Using this principle, it can be shown that from knowledge of the term $\boldsymbol{R}_{\boldsymbol{u}}$, the component of heat flux proportional to velocity $\boldsymbol{u}$ can be found. This is the term $\boldsymbol{q}_{\boldsymbol{u}}^e$ and it is again the consequence of the dependence of collision frequency on temperature. In the coordinate system where $V_e = 0$, electron fluxes are in balance. However, a higher amount of hot (fast) electrons move in the direction of $\boldsymbol{u}$ and a higher amount of cold electrons move in the opposite direction. Consequently, the energy fluxes are not balanced, resulting in net heat flux $\boldsymbol{q}_{\boldsymbol{u}}$. This can be explained by realising that electrical current is predominantly carried by hot electrons (along the magnetic field).

The last component $\boldsymbol{q}_T$ of the heat flux vector is known as Fourier's law of heat conduction and it is a symmetric counterpart of the thermoelectric force $\boldsymbol{R}_T$.

The appearance of tensor transport coefficients corresponds to more complicated motions of charged particles in a magnetic field, which give rise to similar mechanisms that are different for distinct directions with respect to the magnetic field. A more detailed description is given in the following section.

One can also use ion heat conduction here only in the form of Fourier's law:

$$\boldsymbol{q}_i = \boldsymbol{q}_{\boldsymbol{T}}^i = -\frac{n_i k_B T_i \tau_{ie}}{m_i} \underline{\underline{\kappa}}^i \cdot \nabla T_i, \tag{1.27}$$

but it is not considered in this work ($\boldsymbol{q}_i = 0$ is assumed in performed simulations). Transport coefficients $\underline{\underline{\kappa}}^i$ are generally different from $\underline{\underline{\kappa}}$ [37]. This is a common approach, as ion heat conduction is negligible compared to the combined effect of electron heat conduction and electron-ion heat exchange [30].

## 1.5 Transport coefficients

This section further investigates the form of transport coefficients, how they are calculated and what are their physical interpretations. By substituting the expression (1.25b) into the Ohm's equation (1.18), following form of electric field is obtained:

$$\boldsymbol{E} = -\frac{1}{c}\boldsymbol{V} \times \boldsymbol{B} + \frac{1}{en_e c}\boldsymbol{j} \times \boldsymbol{B} - \frac{1}{en_e}\nabla P_e + \frac{m_e}{e^2 n_e \tau_{ei}} \underline{\underline{\alpha}} \cdot \boldsymbol{j} - \frac{k_B}{e} \underline{\underline{\beta}} \cdot \nabla T_e. \tag{1.28}$$

All the contributing terms to the electric field in equation (1.28) are explained in more detail in Chapter 2.

As already mentioned, transport coefficients contain complex dependencies on magnetic field direction and magnitude, ionization and collision frequency. Each tensor coefficient can be rewritten into three scalar coefficients corresponding to contribution in different directions with respect to the magnetic field. With definition of direction of magnetic field $\boldsymbol{b} = \frac{\boldsymbol{B}}{|\boldsymbol{B}|}$, the tensors can be expanded into:

$$\underline{\underline{\alpha}} \cdot \boldsymbol{j} = \alpha_\parallel (\boldsymbol{j} \cdot \boldsymbol{b}) \boldsymbol{b} + \alpha_\perp \boldsymbol{b} \times (\boldsymbol{j} \times \boldsymbol{b}) - \alpha_\wedge \boldsymbol{b} \times \boldsymbol{j}, \tag{1.29a}$$

$$\underline{\underline{\beta}} \cdot \nabla T_e = \beta_\parallel (\nabla T_e \cdot \boldsymbol{b}) \boldsymbol{b} + \beta_\perp \boldsymbol{b} \times (\nabla T_e \times \boldsymbol{b}) - \beta_\wedge \boldsymbol{b} \times \nabla T_e, \tag{1.29b}$$

$$\underline{\underline{\kappa}} \cdot \nabla T_e = \kappa_\parallel (\nabla T_e \cdot \boldsymbol{b}) \boldsymbol{b} + \kappa_\perp \boldsymbol{b} \times (\nabla T_e \times \boldsymbol{b}) - \kappa_\wedge \boldsymbol{b} \times \nabla T_e, \tag{1.29c}$$

where the $\parallel$ subscript represents contribution in $\boldsymbol{b}$ direction, $\perp$ subscript represents contribution perpendicular to $\boldsymbol{b}$ and the $\wedge$ subscript is contribution that is perpendicular to both $\boldsymbol{b}$ and $\nabla T_e$. The contributions of the coefficients into different directions are illustrated in Figure 1.1 for the $\underline{\underline{\beta}}$ tensor.

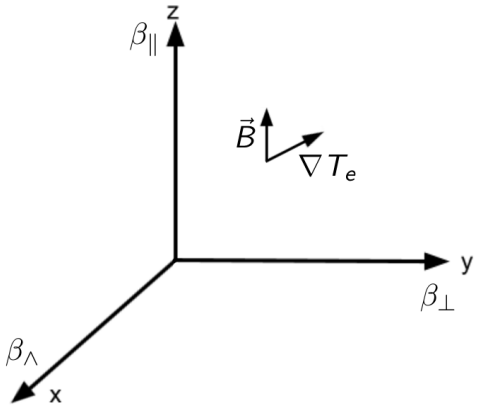


Figure 1.1: Decomposition of $\underline{\underline{\beta}}$ tensor into three components based on the direction of magnetic field and temperature gradient $\nabla T_e$. In this example, both vectors $\boldsymbol{B}$ and $\nabla T_e$ lie in the $yz$ plane.

An interesting fact to note is that the cross terms (last terms on the LHS of equations (1.29)) lead to transport, which is perpendicular to either current density or temperature gradient. This is the direct consequence of curved trajectories of charged particles and can only happen for non-zero magnetic fields. Indeed, the coefficients $\alpha_\wedge, \beta_\wedge$ and $\kappa_\wedge$ tend to zero for small magnetic field. These cross coefficients correspond to $\boldsymbol{F} \times \boldsymbol{B}$ drift, where $\boldsymbol{F}$ is either friction or thermal force. On the contrary, strong magnetic fields will limit transport in the perpendicular direction to the magnetic field. This means that for high values of $|\boldsymbol{B}|$, $\alpha_\parallel \gg \alpha_\perp, \beta_\parallel \gg \beta_\perp$ and $\kappa_\parallel \gg \kappa_\perp$ hold. These physical intuitions can be observed in Figure 1.2, where the dependence of the coefficients of magnetization is plotted (except for the $\underline{\underline{\alpha}}$ coefficients).

An important step, crucial for recognising the impact of each term on magnetic field transport and generation, is to transform Ohm's equation and consequently, the induction equations in the form where the action of each term can be clearly interpreted and ultimately calculated more accurately. This was done by [18, 17] and they showed that the rearrangement of the terms allows one to notice that some contributions to transport processes actually depend not directly on coefficients defined in (1.29), but rather on the differences between them. By defining a new set of coefficients:

$$\delta_\perp = \frac{\alpha_\wedge}{\chi}, \quad \gamma_\perp = \frac{\beta_\wedge}{\chi}, \quad \delta_\wedge = \frac{\alpha_\perp - \alpha_\parallel}{\chi}, \quad \gamma_\wedge = \frac{\beta_\parallel - \beta_\perp}{\chi}, \tag{1.30}$$

Ohm's equation can be transformed into the following form [18]:

$$\boldsymbol{E} = -\frac{1}{c}\boldsymbol{V}_B \times \boldsymbol{B} + D_\parallel \nabla \times \boldsymbol{B} - \frac{1}{en_e}\nabla P_e - \frac{k_B}{e}\beta_\parallel \nabla T_e, \tag{1.31a}$$

$$\boldsymbol{V}_B = \boldsymbol{V} - (1+\delta_\perp)\frac{\boldsymbol{j}}{en_e} + \delta_\wedge \frac{\boldsymbol{j}\times\boldsymbol{b}}{en_e} - \gamma_\perp \frac{k_B \tau_{ei}}{m_e}\nabla T_e + \gamma_\wedge \frac{k_B \tau_{ei}}{m_e}\nabla T_e \times \boldsymbol{b}, \tag{1.31b}$$

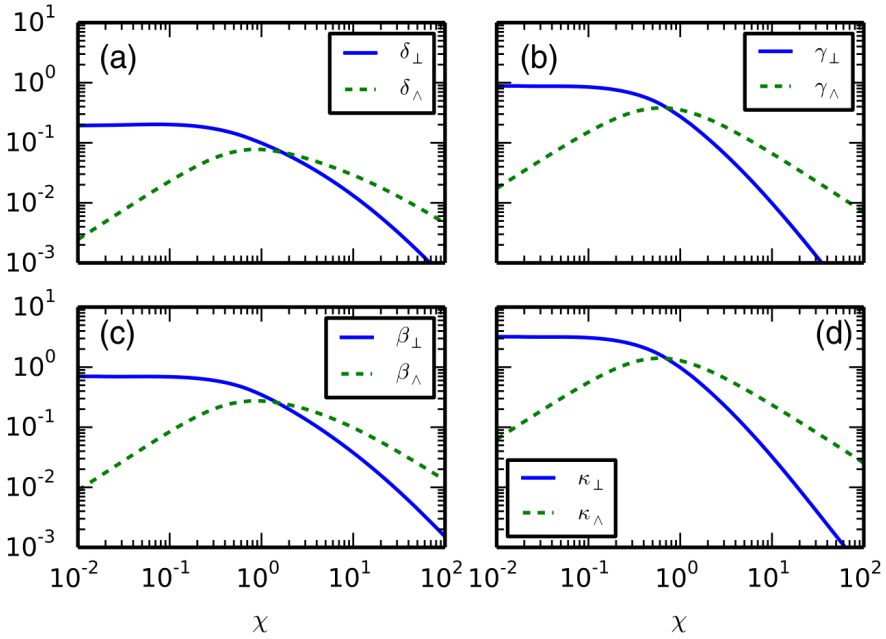


Figure 1.2: The symmetric form of the transport coefficients for $Z = 1$. (a) The Hall coefficients $\delta_\perp$ and $\delta_\wedge$. (b) The Nernst coefficients $\gamma_\perp$ and $\gamma_\wedge$. (c) The thermoelectric coefficients $\beta_\perp$ and $\beta_\wedge$. (d) The Spitzer coefficients $\kappa_\perp$ and $\kappa_\wedge$. This figure was taken from [18].

where the parallel magnetic diffusion coefficient is defined as:

$$D_\parallel = \frac{m_e c}{4\pi e^2 n_e \tau_{ei}} \alpha_\parallel. \tag{1.32}$$

Similarly, the expression for the heat flux can be transformed into:

$$\boldsymbol{q}_e = n_e k_B T_e \boldsymbol{V}_q, \tag{1.33a}$$

$$\boldsymbol{V}_q = -\beta_\perp \frac{\boldsymbol{j}}{e n_e} + \beta_\wedge \frac{\boldsymbol{j} \times \boldsymbol{b}}{e n_e} - \left(\beta_\parallel - \beta_\perp\right) \frac{(\boldsymbol{j} \cdot \boldsymbol{b})\, \boldsymbol{b}}{e n_e} - \tag{1.33b}$$

$$- \kappa_\parallel \frac{k_B \tau_{ei}}{m_e} (\boldsymbol{b} \cdot \nabla T_e)\, \boldsymbol{b} - \kappa_\perp \frac{k_B \tau_{ei}}{m_e} \boldsymbol{b} \times (\nabla T_e \times \boldsymbol{b}) - \kappa_\wedge \frac{k_B \tau_{ei}}{m_e} \boldsymbol{b} \times \nabla T_e. \tag{1.33c}$$

These relations look even more complicated, nevertheless, the physical meaning of each term can be clearly interpreted. In the transformed Ohm's equation (1.31a) most of the terms are contained in the magnetic field advection velocity $\boldsymbol{V}_B$, which is defined by (1.31b). This term indeed leads to advection, therefore it can be inferred, which parts of the thermoelectric and friction force terms contribute to the advection of the magnetic field. As was stated before, some of the contributions actually depend on the difference of previous coefficients (they depend directly on $\gamma_\wedge$ and $\delta_\wedge$). Further, the term corresponding to the diffusion of the magnetic field, which includes coefficient $D_\parallel$, was separated. Finally, the last two terms on the RHS of the equation (1.31a) result in the generation of the magnetic field. The first

of them is well known as *the Biermann battery* (see Section 2.6) and the second corresponds to *Seebeck effect* (see Section 2.7).

Concerning the heat flux, the equation (1.33a) shows that all terms can be written as contributions to temperature advection velocity (1.33c). It should be noted that compared to the velocity $\boldsymbol{V}_B$, the advection velocity $\boldsymbol{V}_q$ has additional contributions in the direction of the magnetic field. This is due to the fact that an advection of the magnetic field in its direction is not possible.

In order to obtain functional dependence for the transport coefficients in the form (1.30), one could measure different effects or terms experimentally and fit a function to the experimental data [9]. However, to setup experiments like this is quite complicated and has not yet been done. The adopted and more feasible option is to take advantage of approximate kinetic calculations using the Fokker-Planck equation [18]. In [18] and [17] rational functions were used for the transport coefficients to fit the calculated kinetic data with an error up to around 1 %. These fits acknowledge the importance of defining new coefficients (1.30) as a difference of the original ones (1.29) and accurately predict values of the cross coefficients $\delta_\wedge$ and $\gamma_\wedge$ for small magnetic fields (magnetizations $\chi \leq 1$). The comparison of the Epperlein and Haines fits with the ones from Sadler [18] are shown in Figure 1.3.

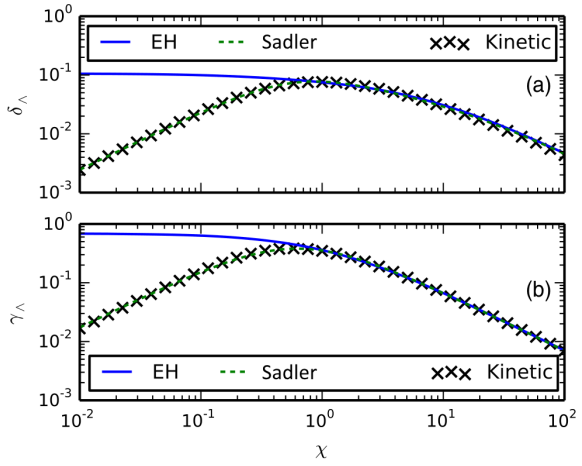


Figure 1.3: Plots of the kinetic (a) $\delta_\wedge$ cross-Hall and (b) $\gamma_\wedge$ cross-Nernst transport coefficients for $Z = 1$. The results of Epperlein and Haines (EH) [19] (blue solid line) are only accurate for $\chi > 1$. The results from Sadler (green dashed line) [18]. This figure was taken from [18].

To summarize this chapter, a derivation of the extended-MHD model equations was presented and the energy transfer between its individual types was discussed in this model. Further, the closure relations that enable one to obtain a solvable set of equations were introduced and their physical meaning and interpretations were described. The next chapter delves deeper and examines the ExMHD in more detail, explains the physical meaning of each term and presents different variations of the MHD model. However, the main focus will be on realising the importance of each

different term for the case of modelling high energy density plasmas, specifically plasma created by the interaction of laser with a solid target.

# Chapter 2

# ExMHD model for laser plasma

In the previous chapter, the extended-MHD model was presented in its full form, which corresponds to the model known from the work of Braginskii [15], and includes modifications introduced in recent papers [17, 18]. The ExMHD model is quite complex and includes many terms which contribute to the dynamics of the laser plasma fluid in different ways. This chapter describes in detail how it is used for modelling laser plasmas. Firstly, the limitations of the model are outlined and the plasma conditions, for which it is sensible to apply this model, are specified. Secondly, the known MHD waves that appear in this description of plasma are summarized. And lastly, the physical meanings and interpretations of the different terms in the model are introduced.

The state of plasma is typically described by many parameters. Those relevant to the following discussion are introduced in Section 2.1. The parameters are then very useful in estimation which terms in the model contribute more and thus dictate the plasma evolution. Further sections then separately describe parts of the model that are typically connected to a physical effect. In practice, it is not uncommon to neglect some of the terms in the full ExMHD model when sensible for considered plasma configuration. The most commonly used simplifications of the ExMHD model are thus also included in the description.

## 2.1 Laser plasma scales

In simulations, carried out in this thesis, a laser pulse with a maximal intensity of $1.2 \times 10^{15}\,\mathrm{W\,cm^{-2}}$ with wavelength $\lambda_L = 0.438\,\mu\mathrm{m}$ and time profile corresponding to FWHM of 400 ps is considered. The laser interacts with solid aluminium target (of density $2.7\,\mathrm{g\,cm^{-2}}$) with radius $400\,\mu\mathrm{m}$ and thickness $60\,\mu\mathrm{m}$. As seen from results in previous works [38, 39] and also from results in Section 5.3, electron temperature, ion temperature and number density in the core of the plasma corona reach values of orders $T_e \sim 10^3$ eV $\approx 10^8$ K, $T_i \sim 10^1 - 10^3$ eV and $n_e \sim 10^{19} - 10^{24}$ cm$^{-3}$ (corresponding to densities of orders $\rho \sim 10^{-5} - 1\,\mathrm{g\,cm^{-3}}$) respectively. Considered magnetic fields are of orders $|\boldsymbol{B}| = B \sim 0 - 10^6$ G $= 10^{-4} - 10^2$ T. Let $\omega_s \sim 10^{10}$ s$^{-1}$ and $k_s \sim 10^2$ cm$^{-1}$ be the characteristic scales of the performed simulations.

In plasma, Debye length is defined as:

$$\lambda_D = \sqrt{\frac{k_B T_e}{4\pi n_e e^2}}, \tag{2.1}$$

and describes the distance at which the electric field is shielded by charged particles in the sense that Coulomb interaction is cancelled at larger distances and collective effects dominate. Charge separation in plasma on large scales (compared to $\lambda_D$) has oscillatory character at the electron plasma frequency:

$$\omega_{pe} = \sqrt{\frac{4\pi e^2 n_e}{m_e}}. \tag{2.2}$$

Plasma is considered to be *quasi-neutral* when time and space scales are larger than electron plasma frequency and Debye length:

$$\omega_{pe} \gg \omega_s, \quad \lambda_D \ll k_s^{-1}. \tag{2.3}$$

This can be understood as any charge separation in plasma is balanced by electron motion in time $\omega_{pe}^{-1}$ and on space scale $\lambda_D$. For considered regime, $\lambda_D \sim 10^{-8} - 10^{-5}$ cm and $\omega_{pe} \sim 10^{13} - 10^{16}$ s$^{-1}$ hold. It is thus clear that laser-produced plasma can be typically assumed quasi-neutral.

One of the key distinctions is between *collisional* or *collisionless* plasma as a measure of the amount of collisions that occur inside the plasma. It is important to note that the collision rate is usually measured in relation to some other considered process that has its own frequency. Collisions in plasma are understood by means of Coulomb interaction between individual charged particles. Plasma is said to be collisionless when it is sufficiently dilute and collisions are rare. This is typical for example in interstellar and other space plasmas. The dynamics of particles are then influenced only by the collective field that the particles create and can be accurately modelled using the Vlasov equation. Dense plasmas, typical for laboratory experiments, are usually collisional. Therefore, the particle trajectories are determined not only by the collective field but also by binary particle interactions. The electron-electron collision time has the following approximate form [30]:

$$\tau_e \approx 2.7 \frac{T_e^{\frac{3}{2}}}{n_e \ln \Lambda}, \tag{2.4}$$

where $\ln \Lambda$ is Coulomb logarithm, which for considered temperatures and densities takes values of order $\ln \Lambda \sim 1 - 10$. Scaling for electron-ion collision time is similar (see equation (4.1)):

$$\tau_{ei} \approx \frac{1}{Z\sqrt{2}} \tau_e \approx 1.4 \frac{T_e^{\frac{3}{2}}}{Z n_e \ln \Lambda}. \tag{2.5}$$

The Coulomb logarithm is generally different, but of the same order, for distinct types of collisions, however, these relations are only used for the estimation of characteristic laser-plasma parameters.

The importance of collisions can be quantified by the Knudsen number [26], which is defined either by using electron-ion collision frequency $\tau_{ei}$ when considering time variations $\omega_s$:

$$K_n' = \omega_s \tau_{ei}, \tag{2.6}$$

or by using the electron mean free path $\lambda_{mpfe}$ when considering space variations $k_s$:

$$K_n = k_s \lambda_{mpfe}, \tag{2.7}$$

where the mean free path is defined as the average distance travelled by a particle between two subsequent collisions at thermal velocity:

$$\lambda_{mfpe} = v_{T_e} \tau_{ei}, \tag{2.8}$$

where $v_{T_e} = \sqrt{\frac{k_B T_e}{m_e}}$ is the electron thermal velocity.

As mentioned before, the laser plasma is typically collisional and indeed both inequalities $K_n \sim 10^{-4} - 10^{1} \ll 1$ and $K_n' \sim 10^{-4} - 10^{1} \ll 1$ hold for assumed parameters, except for more dilute $n_e \sim 10^{19} - 10^{20}$ cm$^{-3}$ parts of the expanding plasma, where the Knudsen numbers are $K_n, K_n' \approx 1$ or larger. Thus, plasma is collisional in the overcritical region of the corona, while in the subcritical low-density region of the corona, it is not. This exception of model exactness was discussed in [38] and holds in the laser plasma close to the surface of the corona. This limitation, which implies that the transport models (1.25) is incorrect, is known in hydrodynamic simulations of laser-produced plasmas [1, 40] and is further discussed in Section 2.8.

Also, it is useful to quantify the effects of magnetic fields on plasma behaviour. A strong magnetic field can significantly influence transport processes in plasma when electron gyrofrequency:

$$\omega_{ce} = \frac{eB}{m_e c} \tag{2.9}$$

is of order or larger than collision rate $\omega_{ce} \approx \nu_e$ or equivalently when electron Larmor radius:

$$r_e = \frac{v_{T_e}}{\omega_{ce}} \tag{2.10}$$

becomes comparable to electron mean free path $r_e \approx \lambda_{mfpe}$. In the presence of a magnetic field, electrons move along a cycle with a Larmor radius. If the magnetic field is small enough, particles travel only a small part of the cycle between two subsequent collisions. Consequently, the trajectories are almost the same as in the case of zero magnetic fields. However, a strong magnetic field confines the electron movement to small radii $r_e$ in a perpendicular direction to the magnetic field. This will be illustrated in more detail in the following sections.

Another parameter concerning the magnetic field is computed as a fraction of pressure and magnetic field pressure. The Lorentz force can be rewritten as a gradient of the magnetic pressure tensor:

$$\frac{1}{c}\boldsymbol{j} \times \boldsymbol{B} = \frac{1}{4\pi} \nabla \cdot \left( \boldsymbol{B}\boldsymbol{B} - \frac{1}{2}\boldsymbol{B}^2 \underline{\underline{I}} \right) = \nabla \cdot \underline{\underline{P_B}}. \tag{2.11}$$

Considering only the isotropic magnetic pressure (second part of the tensor), the momentum equation (1.14b) is obtained in the following form:

$$\frac{\partial(\rho \boldsymbol{V})}{\partial t} + \nabla \cdot (\rho \boldsymbol{V}\boldsymbol{V}) + \nabla(P + P_B) = 0, \tag{2.12}$$

where $P_B = \frac{1}{2}B^2$. From equation (2.12), one can infer that the Lorentz force will dominate plasma fluid evolution when:

$$\beta = \frac{P}{P_B} < 1. \tag{2.13}$$

For the assumed laser plasma configuration, the $\beta$ parameter is significantly higher than 1. Only for lower densities ($n_e \sim 10^{19} - 10^{20}$ cm$^{-3}$) and very strong magnetic field $B = 10^6$ G $= 10^2$ T, it is obtained $\beta \approx 1$. Therefore, the magnetic field significantly influences the hydrodynamic motion of the expanding plasma only in case of a strong magnetic field of order 1 MG = 100 T.

## 2.2 MHD waves

In this section, waves that can form in plasma, which is described by the first two equations from (1.14) together with the induction equation:

$$\frac{\partial \rho}{\partial t} + \nabla \cdot (\rho \boldsymbol{V}) = 0, \tag{2.14a}$$

$$\frac{\partial(\rho \boldsymbol{V})}{\partial t} + \nabla \cdot (\rho \boldsymbol{V}\boldsymbol{V}) + \nabla(P + P_B) = 0, \tag{2.14b}$$

$$\frac{\partial \boldsymbol{B}}{\partial t} = -c\nabla \times \boldsymbol{E} = \nabla \times (\boldsymbol{V} \times \boldsymbol{B}), \tag{2.14c}$$

are introduced. Only the part electric field $\boldsymbol{E} = -\frac{1}{c}\boldsymbol{V} \times \boldsymbol{B}$ that leads to magnetic advection along the fluid motion is inserted into (2.14c). This set of equations is known as *ideal MHD* model of plasma, where one assumes zero electrical resistivity and other terms in the generalized Ohm's equations are neglected. More waves that result from different contributions to the electric field (1.18) are included in the following sections.

In plasma with zero magnetic fields, there are three kinds of waves [30] that can propagate through the medium: electromagnetic, electron plasma and ion-sound waves. The first two are high-frequency waves and are not included in the MHD model. Propagation of laser is handled in the approximation of geometrical optics (Section 4.4). Electron plasma waves, also known as *Langmuir waves*, correspond to the fast motion of electrons with respect to static ions. In this thesis, plasma is treated as a single fluid, therefore this type of process is neglected. The ion waves are low-frequency acoustic waves that travel with phase velocity:

$$c_s = \sqrt{\gamma \frac{Z k_B T_e}{m_i}}. \tag{2.15}$$

These waves are implicitly included as a solution to the equations of mass (2.14a) and momentum (2.12) conservation. In considered laser plasma, typical ion wave speeds are of order $c_s \sim 10^8$ cm s$^{-1}$.

By including magnetic field into the hydrodynamic equations (1.14), one obtains two other waves that can be excited in the plasma. The first wave, so-called *Alfvén wave*, propagates along magnetic field lines $\boldsymbol{B}$ at constant velocity:

$$v_A = \frac{B}{\sqrt{4\pi\rho}}. \tag{2.16}$$

Alfvén waves are a consequence of magnetic pressure acting on plasma fluid in a similar way as ion waves result from disturbances in hydrodynamic pressure. The $\beta$ parameter can also be calculated using both of these velocities:

$$\beta = \frac{c_s^2}{v_A^2}. \tag{2.17}$$

Therefore, from the result in the previous section, the Alfvén velocity reaches values $v_A \approx 10^8$ cm s$^{-1}$ in the lower density part of plasma corona in a strong magnetic field of order 1 MG.

The second type of wave is the last solution to the system of equations (2.14) and can be understood as a combination of ion and Alfvén waves [29]. It travels at phase velocity:

$$v_\pm^{MS} = \frac{1}{2}\sqrt{c_s^2 + v_A^2 \pm \sqrt{\left(c_s^2 + v_A^2\right)^2 - 4c_s^2 v_A^2 \frac{k_\parallel^2}{k^2}}}, \tag{2.18}$$

where $k$ is wave number, $\boldsymbol{k}$ points to the direction in which the wave propagates and $k_\parallel$ is the contribution of the wave vector along the magnetic field direction. There are actually two magnetosonic waves travelling at different velocities. For special case of propagation along the magnetic field $k = k_\parallel$, (2.18) reduces to the ion $v_+^{MS} = c_s$ and Alfvén wave $v_-^{MS} = v_A$. In the case $k = k_\perp$, the second wave disappears ($v_-^{MS} = 0$) and the first one corresponds to a modified sound wave.

To conclude this section, waves that appear in the MHD model are important for the construction of numerical schemes as they dictate how fast can disturbances travel in the modelled system.

## 2.3 Anisotropic thermal conduction

A particle propagates in plasma with thermal velocity until it collides with some other particle. Temperature gradients in plasma fluid then naturally lead to diffusion of thermal energy in the gradient direction through random particle motion. The amount of diffusion depends on the rate of collisions, which significantly changes

the particles' direction. This physical process is summarized by the Fourier's law of heat conduction (for electrons):

$$\boldsymbol{q}_T^e = -\frac{n_e k_B T_e \tau_{ei}}{m_e} \underline{\underline{\kappa}} \cdot \nabla T_e, \tag{2.19}$$

and is the first part of the full electron heat transport (1.25a). In conclusion, ion thermal conduction can be neglected. From the equation (1.27) and relation between ion-electron and electron-ion collisions [30]:

$$\tau_{ie} \approx \frac{m_i}{Z^2 m_e} \tau_{ei}, \tag{2.20}$$

and assuming $\underline{\underline{\kappa}} \approx \underline{\underline{\kappa}}^i$, one obtains for $n_e = Z n_i$:

$$\frac{q_T^e}{q_T^i} \approx Z^3 \frac{T_e \nabla T_e}{T_i \nabla T_i} \approx Z^3 \frac{T_e^2}{T_i^2}, \tag{2.21}$$

where the approximation $\nabla T \approx \frac{T}{L_T}$ was made and similar characteristic length scales of electron and ion temperature gradients ($L_{T_e} \approx L_{T_i}$) were assumed. As electron temperature in laser-heated plasma of considered plasma configuration is significantly higher, $\boldsymbol{q}_T^e$ will dominate the thermal transport.

The expression (2.19) is valid only for small temperature gradients when temperature scale length $L_{T_e} \ll \lambda_{mfpe}$. For large temperature gradients, the thermal transport is non-local and thermal transport expression (2.19) strongly overestimates thermal flux. As fluid modelling of non-local thermal conductivity is difficult, a flux limiter for $\boldsymbol{q}_T^e$ is used. In case of $\lambda_{mfpe} > 10^{-2} L_{T_e}$, the thermal transport is significantly reduced, thus an inhibition factor $f_T$ is introduced, defined as a fraction of actual heat flux and free streaming flux:

$$q_f^T = n_e k_B T_e v_e = n_e k_B T_e \left( \frac{k_B T_e}{m_e} \right)^{\frac{1}{2}}. \tag{2.22}$$

Typical values based on the experimental measurement are from the range of $0.05 - 0.1$ for laser-produced plasmas. The limited flux is then, in the case of the FLASH code, calculated using Larsen's interpolation [13], which for the isotropic case is of the following form:

$$\boldsymbol{q}_T^e = -D \nabla T_e, \quad D = \left( \left( \frac{1}{\kappa} \right)^2 + \left( \frac{|\nabla T_e|}{|f_T q_f^T|} \right)^2 \right)^{-\frac{1}{2}}. \tag{2.23}$$

In the anisotropic case, the $\kappa_\parallel$ coefficient is limited using (2.23) and other coefficients $\kappa_\perp$ and $\kappa_\wedge$ are rescaled accordingly in order to retain the anisotropic character of the transport.

Magnetic field limits heat transport in the perpendicular direction to its field lines. Thus, the amount of transport generally differs in longitudinal and transverse

directions. This is expressed by the tensor form of heat transport coefficient $\underline{\underline{\kappa}}$. It was already shown in the previous chapter that the tensor can be rewritten into components based on the direction of the magnetic field:

$$\boldsymbol{q}_T^e = -\frac{n_e k_B T_e \tau_{ei}}{m_e} \left( \kappa_\parallel \left( \boldsymbol{b} \cdot \nabla T_e \right) \boldsymbol{b} - \kappa_\perp \boldsymbol{b} \times \left( \nabla T_e \times \boldsymbol{b} \right) - \kappa_\wedge \boldsymbol{b} \times \nabla T_e \right). \tag{2.24}$$

The parallel coefficient $\kappa_\parallel$ is constant and depends only on average ionization $Z$. For small magnetic fields, $\kappa_\perp \approx \kappa_\parallel$ and for strong magnetic fields that result in magnetization of order $\chi \approx 1$ and higher, transverse coefficients scale as $\kappa_\perp \sim \chi^{-2}$.

The presence of a magnetic field in plasma leads to thermal transport in a new direction that is transverse to both the temperature gradient and the field itself. This type of thermal conduction is known as *Righi-Leduc effect* or as the *thermal Hall effect* since there is an analogy with the electrical version of this effect (Section 2.5). Naturally, for a weak magnetic field, this effect is insignificant and the transport coefficient scales as $\kappa_\wedge \sim \chi$. The maximum is reached for magnetization around $\chi \approx 1$ and for stronger fields, the scaling is inverted: $\kappa_\wedge \sim \chi^{-1}$.

## 2.4 Resistive MHD

In this and the following sections, the role of individual terms in Ohm's equation (1.28) and consequently in the induction equation, which dictates the evolution of the magnetic field, is discussed. When currents flowing perpendicularly to the magnetic field can be neglected and the pressure and temperature gradient sources (see RHS of the equation (1.18)) are small, Ohm's equation can be written in the approximate form:

$$\boldsymbol{E} = -\frac{1}{c} \boldsymbol{V} \times \boldsymbol{B} + \underline{\underline{\eta}} \cdot \boldsymbol{j}. \tag{2.25}$$

Last term in (2.25) that includes magnetic resistivity (electric resistivity in a magnetic field):

$$\underline{\underline{\eta}} = \frac{m_e}{e^2 n_e \tau_{ei}} \underline{\underline{\alpha}}, \tag{2.26}$$

causes the magnetic field to diffuse. When inserted into the induction equation, it is obtained:

$$\frac{\partial \boldsymbol{B}}{\partial t} = \nabla \times \left( \boldsymbol{V} \times \boldsymbol{B} - c \underline{\underline{\eta}} \cdot \boldsymbol{j} \right) \tag{2.27}$$

Magnetic diffusion can be physically understood by noticing that the electric current accompanying the magnetic field is affected by collisions, which cause a broadening of the current-carrying region. There is an analogy to classical diffusion: velocity and direction of colliding electrons change slightly in a random fashion, which spreads out the current lines.

Moreover, in this process, electrons lose part of their ordered velocity that drives the electrical current. This induces energy transfer (seen in (1.22) and (1.23a)) from

magnetic field energy into electrons internal energy:

$$\frac{\partial \varepsilon_e^{int}}{\partial t} = \boldsymbol{R_u} \cdot \boldsymbol{u} = \frac{1}{en_e} \boldsymbol{j} \cdot \left( \underline{\underline{\eta}} \cdot \boldsymbol{j} \right) \equiv \frac{1}{en_e} \underline{\underline{\eta}} : \boldsymbol{jj}. \tag{2.28}$$

For isotropic magnetic resistivity $\eta$ (assuming small magnetization $\eta = \eta_\parallel = \eta_\perp$), the heating term simplifies to the better-known form of Ohm's heating:

$$\frac{\partial \varepsilon_e^{int}}{\partial t} = \frac{\eta}{en_e} \boldsymbol{j}^2. \tag{2.29}$$

It is possible to quantify the importance of magnetic diffusion utilizing the magnetic Reynolds number [32]:

$$R_m = \frac{4\pi\omega_s}{\eta c^2 k_s^2} = \tau_B \omega_s, \quad \tau_B = \frac{4\pi}{\eta c^2 k_s^2}, \tag{2.30}$$

where $\tau_B$ is magnetic diffusion time. When the magnetic Reynold number is large the magnetic field diffuses very slowly thus the diffusion can be neglected and one can use the ideal MHD model introduced in the previous section. Resistivity actually scales only with electron temperature (not with electron number density), therefore $\tau_B$ also depends only on temperature and for $T_e \approx 10^3$ eV it gives $\tau_B \sim 10^{-7}$ s. Thus, for considered laser-plasma scales, magnetic diffusion should not be neglected in considered simulations as $\tau_B \omega_s \approx 10^3$.

Returning to anisotropic resistivity and rewriting the equation (2.27) using the relation (1.29a), following form of the induction equation is obtained:

$$\frac{\partial \boldsymbol{B}}{\partial t} = \nabla \times \left( \boldsymbol{V} \times \boldsymbol{B} - c\eta_\parallel \left( \boldsymbol{j} \cdot \boldsymbol{b} \right) \boldsymbol{b} - c\eta_\perp \boldsymbol{b} \times \left( \boldsymbol{j} \times \boldsymbol{b} \right) + c\eta_\wedge \boldsymbol{b} \times \boldsymbol{j} \right). \tag{2.31}$$

Furthermore, using the expression $\boldsymbol{j} = \left( \boldsymbol{j} \cdot \boldsymbol{b} \right) \boldsymbol{b} + \boldsymbol{b} \times \left( \boldsymbol{j} \times \boldsymbol{b} \right)$, one arrives at:

$$\frac{\partial \boldsymbol{B}}{\partial t} = \nabla \times \left( \boldsymbol{V} \times \boldsymbol{B} - c\eta_\parallel \boldsymbol{j} - c \left( \eta_\perp - \eta_\parallel \right) \boldsymbol{b} \times \left( \boldsymbol{j} \times \boldsymbol{b} \right) + c\eta_\wedge \boldsymbol{b} \times \boldsymbol{j} \right). \tag{2.32}$$

This is the transformation of the transport coefficients, which was briefly introduced in Section 1.5, and allows one to separate usual resistive diffusion $c\eta_\parallel \boldsymbol{j}$ from the other two terms that contribute to magnetic field advection. The last two terms on RHS of equation (2.32) are actually closely related to the Hall effect and can be interpreted as its collisional corrections [9]. The contribution along the magnetic field and in a direction perpendicular to $\boldsymbol{j}$ depends on the difference between the parallel and transverse coefficients. For small magnetizations, this term is negligible as $\eta_\perp$ approaches $\eta_\parallel$.

## 2.5 Hall effect

The examination of the terms contained in the ExMHD model continues with the Hall effect. This physical effect is a consequence of the magnetic (or Lorentz) force,

that acts in the perpendicular direction to the velocity of charged particles. The resulting term in the generalized Ohm's equation is Hall electric field $\frac{1}{en_e c}\boldsymbol{j} \times \boldsymbol{B}$. If only the Hall term is considered and together with the convective term $\frac{1}{c}\boldsymbol{v} \times \boldsymbol{B}$, one obtains the Hall-MHD model (supposing magnetic diffusion and other terms can be neglected):

$$\frac{\partial \boldsymbol{B}}{\partial t} = \nabla \times \left( \boldsymbol{V} \times \boldsymbol{B} - \frac{1}{en_e}\boldsymbol{j} \times \boldsymbol{B} \right) = \nabla \times \left( \boldsymbol{V}_e \times \boldsymbol{B} \right), \tag{2.33}$$

where the relation for electron velocity is used $\boldsymbol{V}_e = \frac{1}{en_e}\left(\boldsymbol{j} - en_e \boldsymbol{V}_i\right)$ with $\boldsymbol{V}_i \approx \boldsymbol{V}$. Similarly, as in the ideal MHD model, in Hall-MHD the magnetic field is *frozen-in* and moves together with the electron fluid.

Inserting Hall electric field into the equation (1.20), one can notice there is no energy source associated with the Hall effect, as $\boldsymbol{E} \cdot \boldsymbol{j} \sim (\boldsymbol{j} \times \boldsymbol{B}) \cdot \boldsymbol{j} = 0$ is always true. Thus, this term only contributes to the advection of magnetic field energy through Poynting vector $\frac{c}{4\pi}\boldsymbol{E} \times \boldsymbol{B}$ and does not alter electron internal energy.

Dimensional analysis shows that this term can be ignored when [26]:

$$\frac{\omega}{k^2} \gg v_A d_i, \tag{2.34}$$

where $d_i$ is ion inertial length:

$$d_i = \frac{c}{\omega_{pi}}, \tag{2.35}$$

where $\omega_{pi}$ is ion plasma frequency. For assumed simulation parameters following scales are estimated: $\frac{\omega}{k^2} \sim 10^3\ \mathrm{cm^2\,s^{-1}}$ and $v_A d_i \sim \frac{B}{n_e} \approx 10^{-1} - 10^6\ \mathrm{cm^2\,s^{-1}}$. In conclusion, the Hall effect is significant and should be included in the physical model for the strong magnetic field of orders $B \sim 1\,\mathrm{MG}$ and less dense parts of the plasma corona. Nevertheless, this term is neglected in simulations conducted in this thesis. The reason is the limitations on computational time steps that are a consequence of fast waves that can be excited in the Hall-MHD model.

The Hall electric field contribution to the induction equation introduces two new types of waves that need to be handled by the numerical scheme. Both waves are solely oscillations of magnetic field vector and can be derived as in [41] from the modified form of Hall electric field in the induction equation:

$$\frac{\partial \boldsymbol{B}}{\partial t} = -\frac{1}{en_e}\nabla \times (\boldsymbol{j} \times \boldsymbol{B}) + \frac{1}{en_e^2}\nabla n_e \times (\boldsymbol{j} \times \boldsymbol{B}). \tag{2.36}$$

The first term on the RHS of the expression (2.36) leads to so-called *Whistler waves* that propagate at phase velocity:

$$v_{wh} = v_A \frac{k_\parallel c}{\omega_{pi}} = v_A k_\parallel d_i, \tag{2.37}$$

where $k_\parallel = (\boldsymbol{k} \cdot \boldsymbol{b})\,\boldsymbol{b}$. This relation implies that the velocity will exceed Alfvén's velocity when the spatial scale of the perturbation is smaller than the ion inertial

length: $k_{\parallel} d_i > 1$. Estimated scale of ion inertial length is $d_i \sim 10^{-4} - 10^{-1}$ cm and simulation scale size is $k_s^{-1} \approx 10^{-2}$ cm. Thus, for lower densities, the Whistler wave speed is higher than the Alfvén velocity.

The second type of wave is known as *Hall drift wave* and it propagates in inhomogeneous plasma in the $\boldsymbol{k} \parallel \boldsymbol{B} \times \nabla n_e$ direction. The corresponding phase velocity for this wave can be derived in the following form [41]:

$$v_{hd} = v_A \frac{c}{\omega_{pi} L_{n_e}} = v_A \frac{d_i}{L_{n_e}}, \tag{2.38}$$

where $L_{n_e} = \frac{n_e}{|\nabla n_e|}$ is characteristic length of electron density gradient. Similarly, the Hall drift waves propagate faster than Alfvén waves for $d_i > L_{n_e}$. Density gradient scales in laser plasma can vary depending on specific problems. However, shock wave formation is common and at its front, the density gradient reaches very high values. This could result in very fast Hall drift waves close to the discontinuity in the density profile. In performed simulations using the FLASH code, large computed $v_{hd}$ velocities and the creation of strong oscillations in the magnetic field profile (together with oscillations in electron temperature) behind the shock wave propagating into the low-density helium gas are observed. This is elaborated on in Chapter 5, but this problem is not further investigated in this thesis and the Hall effect contribution is neglected in the ExMHD model.

## 2.6 The Biermann battery

In plasma, any pressure imbalance results in a force that accelerates particles in the direction of the pressure gradient. Because electron mass is around three orders of magnitude smaller than ion mass, the acceleration of electrons is substantially higher and this results in charge separation and formation of the electric field $\boldsymbol{E}_B$ that balances the pressure forces. It is well known [42, 32] that this source of a magnetic field is important for laser-target interaction. Near the edges of the plasma corona, expanding from the target surface, the temperature gradient is dominantly radial while the density gradient is dominantly axial. As is shown in this chapter and simulations, the misalignment of these gradients results in the formation of a toroidal magnetic field.

The contribution of the Biermann electric field to the induction equation is given by:

$$\frac{\partial \boldsymbol{B}}{\partial t} = -c \nabla \times (\boldsymbol{E}_B) = \nabla \times \left( \frac{c}{e n_e} \nabla P_e \right). \tag{2.39}$$

The RHS of the equation (2.39) can be further modified by the application of the curl operator:

$$\frac{\partial \boldsymbol{B}}{\partial t} = -\frac{c}{e n_e^2} \nabla n_e \times \nabla P_e = -\frac{c k_B}{e n_e} \nabla n_e \times \nabla T_e, \tag{2.40}$$

where the equation of state for ideal gas $P_e = n_e k_B T_e$ was used in the second equality.

A magnetic field is generated at the expense of internal electron energy. This can be intuited from the last two equations in (1.22) and from equation (1.23a), where the energy transfer between magnetic and interval energy is mediated by the term $\frac{1}{en_e}\boldsymbol{j}\cdot\nabla P_e$. The source of magnetic energy corresponds to the difference in work done by pressure gradient on electrons and ions [6].

The Biermann battery term can be neglected compared to the convection term $\frac{1}{c}\boldsymbol{V}\times\boldsymbol{B}$ in Ohm's equation when [26]:

$$k_s^2 r_e^2 \ll 1. \tag{2.41}$$

For assumed parameters of the laser-plasma problem, it was estimated $k_s^2 r_e^2 \sim 1{-}10^4$, thus this term significantly contributes to the evolution of the magnetic field and influence transverse magnetized heat transport.

Coupling between induction equation (2.40) and electron internal energy conservation equation (1.23a) introduces a new kind of wave [43]. For this so-called *thermal-magnetic wave* (in more recent literature [44] the name *thermomagnetic wave* is used) perturbation theory in cylindrical coordinates gives the following phase velocity:

$$v_{tm} = \sqrt{\frac{\gamma-1}{\gamma}}\frac{d_i}{L'_{n_e}}c_s, \tag{2.42}$$

where $L'_{n_e} = \frac{n_e}{|\partial_r n_e|}$. Similarly, as in the case of Hall drift waves, the thermomagnetic waves become faster than sound waves on scales smaller than ion inertial length. Therefore, one can again expect these faster waves in a more dilute part of the plasma corona.

## 2.7 Thermoelectric terms

The final term that contributes to the generalized Ohm's equation is the thermal force $\boldsymbol{R}_T$. As was shown in Section 1.4, this force is closely related to the electric-current driven heat transport term $\boldsymbol{q_u}$. By writing only the thermoelectric terms to the magnetic induction equation and using coefficients transformations (1.30), one obtains:

$$\frac{\partial \boldsymbol{B}}{\partial t} = \nabla\times(\boldsymbol{V}_N\times\boldsymbol{B}) + \nabla\times\left(\frac{ck_B}{e}\beta_\parallel\nabla T_e\right), \tag{2.43a}$$

$$\boldsymbol{V}_N = -\gamma_\perp\frac{k_B\tau_{ei}}{m_e}\nabla T_e + \gamma_\wedge\frac{k_B\tau_{ei}}{m_e}\nabla T_e\times\boldsymbol{b}, \tag{2.43b}$$

where $\boldsymbol{V}_N$ is the Nernst advection velocity. The first term with $\gamma_\perp$ corresponds to the Nernst effect, which is a well-known phenomenon in metals and superconductor physics [45]. In metals, this effect creates an electrical field as a consequence of the temperature gradient. In plasma, this term moves (advects) the magnetic field against temperature gradients with velocity given by the first part of (2.43b). Thus,

the magnetic field motion is not just dictated by the fluid motion. Additionally, in the presence of an external magnetic field, the electric field appears also in the transverse direction to both temperature gradient and magnetic field. This effect, analogous to the Righi-Leduc effect in heat transport, is called the Anomalous Nernst effect, but in plasma physics literature is known as Cross-field Nernst [9]. The term including $\beta_{\parallel}$ coefficient relates to the Seebeck effect and produces an electric field along the temperature gradient, independent of magnetic field direction and strength (as $\beta_{\parallel}$ is constant). This term, similar to the Biermann battery, leads to the generation of a magnetic field when $\nabla\beta_{\parallel} \times \nabla T_e$.

The thermoelectric force induces energy exchange through term $\frac{1}{en_e}\boldsymbol{j} \cdot \boldsymbol{R}_T \sim \boldsymbol{j}\cdot\nabla T_e$ between the magnetic field and electron internal energy (see equations (1.22)). Contrary to the Ohm's heating term $\sim \boldsymbol{j} \cdot \boldsymbol{j}$, which is always positive, the heat generation via thermoelectric force is reversed when either $\boldsymbol{j}$ or $\nabla T_e$ changes sign. The analogous effect in metals is known as the Thomson effect.

Similarly as for the heat flux coefficients, one can utilize flux limiter (2.23) for the thermoelectric transport. For the Nernst advection, the equivalent free streaming flux (electric field) is:

$$\boldsymbol{q}_f^N = \frac{k_B}{e}\underline{\underline{\beta}} \cdot \boldsymbol{V}_e. \tag{2.44}$$

As will be shown in Section 5.2, it is reasonable to use the same inhibition fraction (flux limiter coefficient) as for the heat flux $f_N = f_T$. However, no literature discussing the flux limitation of thermoelectric transport was found.

Assuming $Z = 1$ and collision frequency in form (2.4), following relation holds for the heat flux and thermoelectric coefficients [20]:

$$\frac{\kappa_\perp}{\gamma_\perp} \approx \frac{\kappa_\wedge}{\gamma_\wedge} \approx \frac{5}{2}. \tag{2.45}$$

This relationship between magnetic (2.43b) and thermal (1.33c) advection velocities, which result from temperature gradients, can be interpreted as the magnetic field is only frozen into the movement of faster electrons. The magnetic field thus advects against temperature gradient, as more fast electrons move in that direction.

The Nernst terms, contained in the Nernst velocity $\boldsymbol{V}_N$, lead to so-called *Nernst thermomagnetic wave* that can significantly alter the evolution of magnetic field in laser plasmas [44]. This wave travels with phase velocity $\boldsymbol{V}_N$ and its effect on magnetic field transport is illustrated in simulations in Section 5.1.2. Correspondingly to the Biermann battery, the Seebeck term will also be accompanied by thermomagnetic waves.

## 2.8 Instabilities

In this section, a summary of known instabilities in laser-produced plasma is given. The focus is on various thermomagnetic instabilities that arise from terms in the

extended-MHD description of plasma. Generally, instability is a non-linear process, in which perturbations are not damped, but rather grow exponentially.

Concerning laser-induced plasmas, an instability involving an interplay between magnetic field generation (via the cross-gradients term $\nabla T_e \times \nabla n_e$) and magnetized thermal transport has been predicted [46]. This so-called *thermomagnetic instability* is believed to be one of the main mechanisms that create filamentary structures in coronal plasmas [6]. Specifically, the instability is induced by coupling between the Biermann and Righi-Leduc terms in the ExMHD model. The filaments, sometimes called jets [5], are also explained by thermal flux inhibition that increases the strength of generated fields and in turn the growth of the instability. It can be shown [6] that this instability only occurs at high temperatures and low densities, which arises for:

$$\frac{\lambda_{mpfe}}{d_e} \gg 1, \tag{2.46}$$

where $d_e = \frac{c}{\omega_{pe}}$ is the electron inertial length. For the considered plasma configuration (outlined in Section 2.1), it was estimated that $d_e \sim 10^{-3} - 10^{-6}$ cm and $\frac{\lambda_{mpfe}}{d_e} \sim 10^2 - 10^5$. This explains the complications encountered when performing laser-target simulations with the full ExMHD model using the FLASH code (see Section 5.3).

A very similar, but different type of instability that does not require magnetic field generation is described in [47]. This instability is driven by both Nernst and Righi-Leduc terms, and is also accompanied by travelling waves similar to the thermomagnetic waves derived in [43], where the Nernst effect was neglected.

Other studied instability in [48] arises from plasma motion and perturbations in the density profile. This instability also produces a filamentary magnetic field in the low-density part of the plasma corona but does not require the Righi-Leduc heat flow. The filaments are created when magnetic pressure is of a similar order as plasma pressure: $\beta \approx 1$.

Despite all these findings, which provide an explanation of the filamentary character of laser plasma corona observed in experiments, a recent thorough study [40] showed that the magnetic-field generating instabilities may be less important than initially thought. As was shown in Section 2.1, the magnetohydrodynamic model has its limitations in plasma conditions relevant to laser fusion. This was quantified by the Knudsen number $K_n$, which showed that the electron mean free path reaches the same or higher orders than the simulation scale length in the hot and less dense region of the plasma corona. Therefore, the ExMHD transport models are not accurate as non-local effects become important. The stabilization of the thermomagnetic instability is demonstrated in [40] by utilizing kinetic simulations. It is shown, that due to non-local transport, the Biermann battery field generation is highly reduced. Furthermore, magnetic fields reach smaller magnitudes as a result of their rapid Nernst advection with the heat flow.

In conclusion, the ExMHD model may overestimate magnetic field generation

and the susceptibility of laser plasmas to thermomagnetic instability. In this thesis, the instability is avoided by considering only the Biermann battery term or Righi-Leduc in laser-target simulations.

# Chapter 3

# Numerical aspects of ExMHD

In this chapter, selected numerical aspects of the ExMHD model are described. The first section discusses numerical problems with the Biermann battery effect and shows two implementations of this effect in the FLASH code. The second section presents a numerical scheme for the Nernst effect using the finite element method.

## 3.1 The Biermann battery

The Biermann battery effect has been successfully included in numerical simulations to explore the generation of the magnetic field in an astrophysical and also ICF context. It has been shown in [49] and thoroughly described in [7] that the Biermann term in the ExMHD model must be treated more carefully as naive implementation fails to converge in the presence of a plasma shock wave. As described in this section, the more wary approach involves shock capturing, limiting the field generation where strong gradients appear in the plasma and modifying the expressions for the Biermann electric field. However, even with those modifications, there are still some limitations that need to be considered.

In [7], the following reformulation of the Biermann term in the equation (2.40) is suggested with the assumption of the ideal gas equation of state $P_e = n_e k_B T_e$:

$$\boldsymbol{E}_B = -\frac{k_B}{e} T_e \nabla \ln P_e, \quad \frac{\partial \boldsymbol{B}}{\partial t} = \frac{c k_B}{e} \nabla T_e \times \nabla \ln P_e. \tag{3.1}$$

The reason for this modification is the presence of electron thermal conduction, which ensures that electron temperature $T_e$ is continuous at the shock, whereas $n_e$ is not. The Biermann electric field also contributes to the total energy equation (1.21) through the flux of electromagnetic energy (Poynting vector) $\frac{c}{4\pi}\boldsymbol{E} \times \boldsymbol{B}$. With the assumption of non-zero resistivity, a justification is presented in [7] that the Biermann source term contributions to the induction equations and total energy equation in the modified form (3.1) is mathematically well defined even at discontinuities and gives correct field across the shock without need for flux limiter. The incorrect behaviour is the result of numerical discretization of differential equations together with the straight-forward form of the Biermann battery term (RHS of the equation (2.40)). The limitation of this derivation is the assumption of strong enough electron thermal conduction (but appropriate for laser-plasma).

The FLASH code currently contains two distinct implementations of the Biermann effect included in the ExMHD model. The first so-called *source-version* im-

plementation evolves the magnetic field by simply adding the contribution of the source Biermann term on the RHS of the equation (2.40) during the time step $\Delta t$ together with limiting the electron density and pressure gradients using the *minmod* limiter:

$$\Delta \boldsymbol{B} = \Delta t \frac{c}{e n_e^2} minmod(\nabla n_e) \times minmod(\nabla P_e). \tag{3.2}$$

As the total energy of the magnetic field increases, it has to be transformed from one of the other types of energy. In the FLASH code [13], magnetic energy increase is compensated by a decrease of electron internal energy (this is justified in energy conservation equations (1.22) shown in Section 1.3). This implementation was used in the preceding work [38] and is also used here as it provides a possibility to simulate laser-plasma interaction with reasonable time steps while giving expected results. However, this implementation does not converge on the shock front and therefore using better implementation would be more rigorous. The problems at the shocks are mitigated by using a shock detection tool, to find regions with large density gradients and neglecting the Biermann battery effect in them.

The second implementation, named *flux-version*, computes fluxes corresponding to the contribution of the Biermann effect in the induction equation and total energy equation using the modified form of the Biermann battery term (3.1). The fluxes are then used in a finite-volume numerical scheme to evolve total and internal energies and magnetic fields. Energy transfer in the second version is handled by a more physical argument [13]. The presence of the Biermann electric field is the direct consequence of the electron pressure and the full electron enthalpy transport needs to be taken into account:

$$\frac{\partial \varepsilon_e^{int}}{\partial t} + \nabla \cdot \left( \varepsilon_e^{int} \boldsymbol{V}_e \right) + P_e \nabla \cdot \boldsymbol{V}_e \approx \tag{3.3a}$$

$$\approx \frac{\partial \varepsilon_e^{int}}{\partial t} + \nabla \cdot \left( \varepsilon_e^{int} \left( \boldsymbol{V} - \frac{\boldsymbol{j}}{e n_e} \right) \right) + P_e \nabla \cdot \left( \boldsymbol{V} - \frac{\boldsymbol{j}}{e n_e} \right) = 0, \tag{3.3b}$$

where the approximation $\boldsymbol{V}_e = \boldsymbol{u} + \boldsymbol{V}_i \approx \boldsymbol{u} + \boldsymbol{V}$ was used. The equation (3.3) corresponds to the equation 1.23a, which also includes other ExMHD terms. This version of the implementation introduces a new kind of wave - the thermomagnetic wave (see Section 2.6). This wave and corresponding phase velocity need to be taken into account when the time step limit is calculated. For assumed laser-plasma parameters, the time step is significantly reduced and simulation is not feasible with available computational resources. In addition, this implementation also uses shock detection and does not apply the Biermann effect on the shock wave fronts.

In conclusion, the Biermann battery is a complex term in the ExMHD model. It is not only non-linear but contains a cross-product of two gradients, making it hard to handle at discontinuities which appear in the laser-produced plasmas. Although there has been advancement in the development of numerical schemes for the Biermann term, the FLASH code still does not include implementation that would robustly deal with the Biermann effect explicitly on shock wave fronts.

## 3.2 Thermoelectric terms in finite element framework

This section shows an implementation of the Nernst effect terms in the induction and electron internal energy conservation equation. A novel high-order finite element scheme is derived for these contributions, with the motivation of adding the Nernst effect into the PETE2 numerical code [50]. This scheme is then used to study the coupling between the Nernst advection terms in detail (see Section 5.2). The MFEM library [51] is used for the implementations.

From the equations (1.31) and (1.33) only the contribution of the thermoelectric force are separated and inserted into the induction equation and equation (1.31):

$$\rho c_v \frac{\partial T_e}{\partial t} = -\nabla \cdot (\boldsymbol{V}_T T_e)\,, \tag{3.4a}$$

$$\frac{\partial \boldsymbol{B}}{\partial t} = \nabla \times (\boldsymbol{V}_B \times \boldsymbol{B})\,, \tag{3.4b}$$

where the contribution parallel to the magnetic field (Seebeck effect) was neglected and thus set $\underline{\underline{\beta}}' = \underline{\underline{\beta}} - \beta_\parallel \underline{\underline{I}}$. The scheme for the terms generating magnetic fields is more complex [52] and not addressed here. Additionally, the Ohm's heating term $\boldsymbol{E}_N \cdot \boldsymbol{j}$ is not considered here. The advection velocities are then given by:

$$\boldsymbol{V}_B = \frac{ck_B}{e|\boldsymbol{B}|}\underline{\underline{\beta}}' \cdot \nabla T_e = \frac{ck_B}{e|\boldsymbol{B}|}\left(-\beta_\wedge \nabla T_e + \left(\beta_\parallel - \beta_\perp\right)(\nabla T_e \times \boldsymbol{b})\right), \tag{3.5}$$

$$\boldsymbol{V}_T = \frac{k_B}{e}\underline{\underline{\beta}} \cdot \boldsymbol{j} = \frac{k_B}{e}\left(\beta_\wedge \boldsymbol{j} \times \boldsymbol{b} - \left(\beta_\parallel - \beta_\perp\right)(\boldsymbol{j} \times \boldsymbol{b}) \times \boldsymbol{b}\right). \tag{3.6}$$

Using the expansion (1.29b) the $\boldsymbol{V}_T$ can be rewritten into:

$$\boldsymbol{V}_T = \frac{ck_B}{e|\boldsymbol{B}|}\underline{\underline{\beta}}' \cdot \left(\nabla \cdot \underline{\underline{P_B}}\right), \tag{3.7}$$

where $\underline{\underline{P_B}} = \frac{1}{4\pi}\left(\boldsymbol{B}\boldsymbol{B} - \frac{1}{2}\boldsymbol{B}^2\underline{\underline{I}}\right)$ represents the magnetic pressure tensor. The magnetic field components need to be handled separately in the finite element framework. A 2D cartesian geometry is considered. The case where only the $B_z$ (perpendicular to the 2D domain) is non-zero is presented here, which also corresponds to the configuration used for simulation in Section 5.2. With this, the temperature advection velocity simplifies to:

$$\boldsymbol{V}_T = -\frac{ck_B}{4\pi e|\boldsymbol{B}|}\beta_\wedge \nabla B_z. \tag{3.8}$$

For finite element scheme formulation, it is useful to write the model equations (3.4) in the integral form:

$$\int_V \rho c_v \frac{\partial T_e}{\partial t} dV = -\int_V \nabla \cdot (\boldsymbol{V}_T T_e)\, dV, \tag{3.9}$$

$$\int_V \frac{\partial B_z}{\partial t} dV = -\int_V \left[\nabla \times (\boldsymbol{V}_B \times \boldsymbol{B})\right]_z dV, \tag{3.10}$$

where $V$ is the volume with elements $dV$ and $[.]_z$ represents the $z$ component of a vector. Further, the model equations are considered in weak form:

$$\int_\Omega \rho c_v \frac{\partial T_e}{\partial t}\varphi d\Omega = -\int_\Omega \nabla\cdot(\boldsymbol{V}_T T_e)\,\varphi d\Omega = \tag{3.11}$$

$$= -\int_\Omega T_e \boldsymbol{V}_T\cdot\nabla\varphi dV + \oint_{\partial\Omega}(\{T_e\} + \frac{1}{2}(\boldsymbol{V}_T\cdot\boldsymbol{n})[T_e])\boldsymbol{V}_T\cdot\boldsymbol{n}[\varphi]dl, \tag{3.12}$$

$$\int_\Omega \frac{\partial B_z}{\partial t}\varphi d\Omega = -\int_V [\nabla\times(\boldsymbol{V}_B\times\boldsymbol{B})]_z\,\varphi dV, \tag{3.13}$$

where $\Omega$ is considered domain, the test function is chosen from the Lebesgue space $\varphi \in L_2(\Omega)$, $\boldsymbol{n}$ is the normal vector to the element edge, $\{.\}$ represents average value at element edges and $[.]$ represents a jump of the specified quantity value in the normal direction to the element edges. The trial functions for electron temperature and magnetic field component $B_z$ are also from $L_2(\Omega)$. The integral in (3.11) was expanded using the chain rule for $\nabla$ and the divergence theorem. The term $\{T_e\} + \frac{1}{2}(\boldsymbol{V}_T\cdot\boldsymbol{n})[T_e]$ represents upwinding modification of calculation $T_e$ along the element edges. This is necessary for obtaining a stable scheme for the advection terms. The electric field $\boldsymbol{E} = \boldsymbol{V}_B\times\boldsymbol{B}$ is calculated by:

$$\int_\Omega \boldsymbol{E}\cdot\boldsymbol{\xi} = \int_\Omega (\boldsymbol{V}_B\times\boldsymbol{B})\cdot\boldsymbol{\xi}, \tag{3.14}$$

where the test functions $\boldsymbol{\xi}$ and the trial functions for $\boldsymbol{E}$ are from the Sobolev space of curl-equipped functions $H_{curl}$. Using this trial space for the electric field allows one to calculate $\nabla\times\boldsymbol{E}$ in (3.13) directly. The upwinding for the magnetic field $B_z$ is performed in the (3.14) calculation. At the element edges, tangential vector $\boldsymbol{V}_B\times\boldsymbol{B}$ is selected from the element in the $-\boldsymbol{V}_B$ direction. Finally, the advection velocities are calculated according to:

$$\int_\Omega \boldsymbol{V}_B\cdot\boldsymbol{\psi}d\Omega = \int_\Omega \frac{ck_B}{e|\boldsymbol{B}|}\left(\underline{\underline{\beta}}'\cdot\nabla T_e\right)\cdot\boldsymbol{\psi}d\Omega + \oint_{\partial\Omega}\left\{\frac{ck_B}{e|\boldsymbol{B}|}\underline{\underline{\beta}}'\cdot\boldsymbol{n}\cdot\boldsymbol{\psi}\right\}[T_e]\,dl, \tag{3.15}$$

$$\int_\Omega \boldsymbol{V}_T\cdot\boldsymbol{\psi}d\Omega = -\int_\Omega \frac{ck_B}{4\pi e|\boldsymbol{B}|}(\beta_\wedge\nabla B_z)\cdot\boldsymbol{\psi}d\Omega - \oint_{\partial\Omega}\left\{\frac{ck_B}{4\pi e|\boldsymbol{B}|}\beta_\wedge\boldsymbol{n}\cdot\boldsymbol{\psi}\right\}[B_z]\,dl, \tag{3.16}$$

where the test function $\boldsymbol{\psi}$ and trial function for the velocities are from the Sobolev space of divergence-equipped functions $H_{div}$.

As was already specified, following the Galerkin approach, the trial functions that approximate the primary variables $T_e$, $B_z$, $\boldsymbol{E}$, $\boldsymbol{V}_B$ and $\boldsymbol{V}_T$ are chosen from the identical spaces as corresponding test functions. After the integration, one obtains a set of ordinary differential equations that can be integrated by classical RK2 method [52].

The advantage of the finite element method is that an arbitrary order of domain discretization can be chosen. The presented scheme is ready to be added to the

numerical scheme shown in [50] (implemented in PETE2 code), which discretizes the resistive MHD equations, while keeping its conservative character. The calculation of the electric field is consistent with the calculation in the scheme. Thus, the model can be extended with the Nernst and Cross-Nernst effects.

# Chapter 4

# Laser plasma models

This chapter introduces some of the laser plasma models that are needed for the ExMHD model presented in Chapter 1. Concretely, these are collision frequency, electron-ion relaxation and laser absorption models. Additionally, a modification of the thermal and electrical conductivity that takes into account the multi-phase nature of laser-target simulations is demonstrated.

## 4.1 Collision frequency

The transport coefficient (see Section 1.5), electron-ion relaxation $Q_{ei}$ and the laser absorption model contain electron-ion collision frequency. In this section, an approximate model is given for this collision frequency. In the limit of ideal plasma, the following expression derived by Spitzer-Härm [35] is an accurate approximation for high plasma temperatures:

$$\nu_{SH} = \frac{4}{3}\sqrt{2\pi}\frac{Ze^4 m_e n_e}{(m_e k_B T_e)^{\frac{3}{2}}}\ln\Lambda, \tag{4.1}$$

where $\ln\Lambda$ represents Coulomb logarithm for electron-ion collisions and is defined with modification for low temperatures [36]:

$$\ln\Lambda = \max\left(2, \ln\left(\sqrt{1+\left(\frac{b_{max}}{b_{min}}\right)^2}\right)\right), \tag{4.2}$$

where $b_{max}$ and $b_{min}$ are the maximum and minimum impact parameters given by [53]:

$$b_{max} = \frac{v_{T_e}}{\omega_{pe}}, \quad b_{min} = \max\left(\frac{Ze^2}{k_B T_e}, \frac{\hbar}{\sqrt{m_e k_B T_e}}\right), \tag{4.3}$$

where $\hbar$ is Planck's constant.

For low temperatures and high densities, the $\nu_{SH}$ diverges giving unphysical values. For laser-target problems, a consistent model of collision frequency for wide ranges of temperatures and densities should be used. The following model, presented in [54], include electron degeneracy for temperatures lower than Fermi temperature:

$$T_F = \frac{\left(3\pi^2 n_e \hbar^3\right)^{\frac{2}{3}}}{2m_e k_B}, \tag{4.4}$$

and electron-phonon interaction for ion temperatures below melting point:

$$\nu_{el-phon} = 2k_S \frac{e^2 k_B T_i}{\hbar^2 v_F}, \tag{4.5}$$

where $\nu_{el-phon}$ is electron-phonon collision frequency in the limit of a cold solid and

$$v_F = \hbar \frac{\sqrt[3]{3\pi^2 n_e}}{m_e} \tag{4.6}$$

is Fermi velocity. The modified collision frequency is then defined as harmonic mean:

$$\nu_E^{-1} = \nu_{SH}^{-1} + \nu_{el-phon}^{-1}. \tag{4.7}$$

This modification of the Spitzer-Härm collision frequency gives accurate values for low temperatures, however, still overestimates for intermediate temperatures. In [54] it is shown that the electron means the free path is for the maximal value of $\nu_E$ significantly smaller than interatomic distance, thus the following criterion is employed:

$$\nu_E < \frac{v_e}{r_0} = v_e \left( \frac{4\pi n_i}{3} \right)^{\frac{1}{3}}, \tag{4.8}$$

where $r_0$ is ion sphere radius and $v_e$ is characteristic electron velocity, proposed in form:

$$v_e = \left( v_F^2 + \frac{k_B T_e}{m_e} \right)^{\frac{1}{2}}. \tag{4.9}$$

The constant $k_S$ can be estimated by measuring the reflectivity of cold solid target [54]. For aluminium approximate value is $k_S \approx 9.4$.

A multi-phase modification of the transport coefficients is suggested here for the ExMHD model by using the modified collision frequency $\nu_E$. This can be achieved in a similar fashion as for the flux limiting (see Section 2.3). Parallel transport terms containing $\tau_{ei}$ are calculated in the multi-phase transport model using both $\nu_{SH}$ and $\nu_E$ and then combined according to relation (4.7) and limited using (4.8). The other two components are rescaled by the fraction of the original and modified parallel transport coefficient. This preserves the anisotropy of the transport.

## 4.2 Electron-ion relaxation

A simple model for electron-ion energy relaxation (in equations (1.23)) based on the corresponding relaxation time is commonly adopted for laser-plasma simulations:

$$Q_{ei} = \rho \frac{c_{v,e}}{\tau_{ei}^E} \left( T_i - T_e \right), \tag{4.10}$$

where $\tau_{ei}^E$ is the electron-ion energy relaxation time and $c_{v,e}$ is the electron specific heat capacity.

## 4.3 Anomalous resistivity

The hot electron current (see Section 4.4.1) and the model of anomalous resistivity are considered. This is motivated by [55], where the importance of increased resistivity in a low-density region of plasma corona on magnetic field generation is demonstrated. It results from the formation of ion-sound instability [56], which occurs in highly heated and low-density plasma. A simplified version of the model from [55] is considered here. The total resistivity is assumed in the form of the sum of collisional resistivity $\eta_c$ and the anomalous resistivity $\eta_a$:

$$\eta = \eta_c + \eta_a, \tag{4.11}$$

where the $\eta_a$ is calculated using a simplified relation:

$$\eta_a \approx 10^{-2} \frac{8.17 \times 10^6}{4\pi} \sqrt{\frac{A}{10^3 \rho Z}}. \tag{4.12}$$

In this form, the anomalous resistivity is implemented inside the newly added ExMHD model in the FLASH code.

## 4.4 Laser absorption

Many physical phenomena lead to laser beam absorption in plasma. However, for fluid plasma simulations, usually, only the collisional absorption mechanism, known as *inverse Bremsstrahlung*, is considered [42]. The decrease in intensity $I$ of a laser beam travelling through a slab of plasma follows:

$$\frac{\mathrm{d}I}{\mathrm{d}z} = -\kappa_{ib} I, \tag{4.13}$$

where spacial damping rate $\kappa_{ib}$ can be approximated using simple model of collisional absorption [30]:

$$\kappa_{ib} = \frac{n_e}{n_c} \nu_{ei}, \tag{4.14}$$

where $n_c$ is critical density defined as:

$$n_c = \frac{m_e \omega_L^2}{4\pi e^2}, \tag{4.15}$$

where $\omega_L$ is laser frequency. The model electron-ion collision frequency can be employed either in Spitzer form [35] (as done in the FLASH code) or in a more complicated form (see Section 4.1).

In laser-heated plasma, electrons absorb laser energy in electron-ion collisions through the inverse Bremsstrahlung process (see Section 4.4). The rate of laser

energy deposition into electrons internal energy directly depends on the electron-ion collision frequency $\nu_{ei} = \frac{1}{\tau_{ei}}$ (in the simplified model (4.14)). As laser energy is absorbed entirely by electrons and the collision time for energy exchange between electrons is $\frac{m_i}{2m_e}$ larger than $\tau_{ei}$, electron temperature in subcritical corona is typically $\sim 2$ times larger than ion temperature. Thus, two temperature models are used here and in most fluid simulations of laser-produced plasmas (see equations (1.23) and (4.10)). Moreover, collisional absorption leads to super-Maxwellian electron distribution for high-Z plasmas [57] as the laser is absorbed predominantly by low energy electrons and electron-electron collisions are not frequent enough ($\nu_{ee} \sim \frac{\nu_{ei}}{Z}$) to establish Maxwellian distribution. This effect is difficult to include in the fluid model and is omitted here.

In the FLASH code, laser propagation through plasma is implemented in an approximation of geometrical optics. Multiple rays are created by dividing the laser beam area into segments. Each ray then carries a fraction of the beam power and its trajectory is calculated by considering the refraction of the ray on the computational cell interfaces [13, 38]. The ray then either passes through the domain or is reflected back at the critical surface.

### 4.4.1 Hot electrons

The second type of absorption mechanism is based on collisionless phenomena. It is known that all of the collisionless absorption mechanisms lead to overheating of a small population of electrons [58]. These suprathermal (hot) electrons have much higher energies compared to the rest of the electrons. The typical distribution of electron energies is illustrated in Figure 4.1. Two populations of electrons can be recognized: cold electrons with average energy of 5 keV and hot electrons with average energy 75 keV.

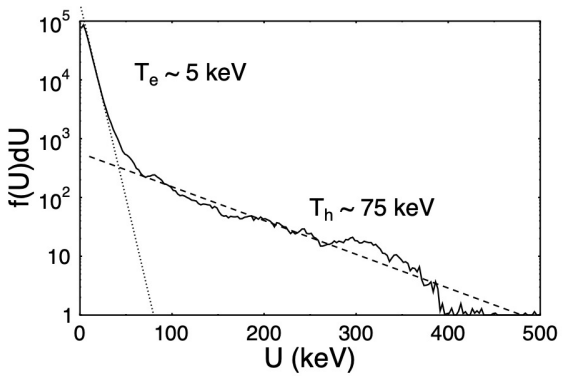


Figure 4.1: Typical bi-Maxwellian electron distribution resulting from absorption of the laser beam by collisionless mechanisms. This example resulted from a 1.5D PIC simulation using the BOPS code with a laser irradience $5 \times 10^{16}$ W/cm$^2\mu$m$^2$ incident at $45°P$ onto a plasma with $\frac{n_e}{n_c} = 3$ and $\frac{L}{\lambda} = 0.2$. This figure is taken from [58].

In recent experiments, it was shown that hot electrons can have a significant influence on the spontaneous generation of the magnetic field [59]. Only resonance absorption is considered as the source of hot electrons and sources due to parametric instabilities like stimulated Raman scattering and two-plasmon decay are omitted. The resonance absorption is the only collisionless process that can be observed for a wide range of laser intensities. The hot electrons are created near the critical density surface and are accelerated both into the dense target and outside the plasma corona. Hot electrons have a naturally larger mean free path than cold electrons and thus penetrate the plasma at greater distances. This results in a hot electron current (one of the two) flowing from the critical density surface in the direction opposite to the incoming laser beam. This direct current has been observed experimentally in [59].

In [55], the addition of hot electron current to the magnetohydrodynamic model is suggested. It is also shown that this addition can be done by simply adding the hot electron current to the resistive one (although the resulting model is not self-consistent). The ExMHD model presented in Chapter 1 contains current density $\boldsymbol{j}$. Thus, the external current density $\boldsymbol{j}_h$ (corresponding to the hot electron current) can be added to the current density $\boldsymbol{j}$ of the plasma (resistive current) according to:

$$\boldsymbol{j}_c = \boldsymbol{j} + \boldsymbol{j}_h = \frac{c}{4\pi}\nabla \times \boldsymbol{B}, \tag{4.16}$$

where $\boldsymbol{j}_c$ is the new total current density that includes the hot electron current density as an external source for the plasma fluid. The final step is to insert $\boldsymbol{j}$ from (4.16) into the ExMHD equations.

A simple model of the hot electron current density is now presented. Assuming that the absorbed laser energy is entirely carried away by the hot electrons leads to the following energy balance equation [58]:

$$\eta_a I_0 = \beta n_h v_h \frac{1}{2} m_e v_h^2, \tag{4.17}$$

where $I_0$ is laser intensity at the critical surface, $n_h$ is the hot electron number density, $\eta_a$ is absorption fraction (fraction of the laser energy that is absorbed by hot electrons), $\beta = \sqrt{\frac{2}{\pi}}$ is a constant that arises from the assumption of 1D Maxwellian distribution of hot electron velocities:

$$v_h = \sqrt{\frac{k_B T_h}{m_e}}, \tag{4.18}$$

where $T_h$ is the hot electron temperature. From equation (4.17), the hot electron number density can be expressed:

$$n_h = \frac{\eta_a I_0}{\beta v_h \frac{1}{2} m_e v_h^2}. \tag{4.19}$$

For hot electron temperature, the following scaling for long pulses is adopted from [58]:

$$T_h^{FKL} \approx 14 \left(I_{16} \lambda_\mu^2 T_e\right)^{\frac{1}{3}} \text{ keV}, \tag{4.20}$$

where $I_{16}$ is laser intensity in $10^{16}$ W cm$^{-2}$, $T_e$ is electron temperature in keV and $\lambda_\mu$ is laser wavelength in $\mu$m. Finally, the hot electron current density is calculated using [59]:

$$j_z = -en_h v_h, \tag{4.21}$$

where $j_z$ is the $z$ component of the hot electron current density $\boldsymbol{j}_h$. The absorption fraction $\eta_a$ can be estimated utilizing the results of experiments with similar conditions (for instance [60]).

## 4.5 External magnetic field

As shown in [8], an applied external magnetic field can prolong the confinement time of the indirect ICF confinement approach. Thus, external magnetic fields could be a promising avenue of exploration. However, magnetized plasma dynamics is increasingly more complicated and can suffer from increased sensibility to instabilities [10]. A developing field of *magnetoinertial fusion* aims to combine inertial and magnetic confinement approached [11] in order to achieve thermonuclear fusion. In conclusion, magnetized plasma investigation is at the front of the fusion research and numerical simulations accurately describing plasma at these conditions are needed to improve our understanding of magnetized plasma dynamics.

In [12], a concept of generating a large axial magnetic field using laser-driven capacitor-coil assembly is presented. The capacitor-coil can be used together with the main laser pulse to synchronously generate a magnetic field. In simulations performed in this thesis, an external magnetic field is assumed to be applied before the laser pulse so that it is uniform before the pulse arrives at the target.

# Chapter 5

# Results of numerical simulations

In this chapter, different simulations of laser-produced plasmas using the ExMHD model are presented. The multiphysics numerical code FLASH was used to conduct the simulations. This code includes the full ExMHD model described in Chapters 1 and 2. The laser energy deposition and propagation are implemented using the ray-tracing method (see Section 4.4) and only the inverse Bremsstrahlung absorption process is considered. We implemented a modification of multi-phase modification transport models according to Section 4, in order to better handle the multi-phase nature of laser-target simulations. For better orientation, relations between common laser focus parameters are included here:

$$\mathrm{FWHM} = \sigma\sqrt{8\ln 2}, \quad r_f = \sigma\sqrt{2\ln 5}, \quad r_0 = \sigma\sqrt{2}, \tag{5.1}$$

where FWHM represents the full width at half maximum, $\sigma$ is standard deviations of Gaussian distribution, $r_f$ is the radius of the focus spot (corresponding to the surface area where 80 % of the laser pulse energy is focused) and $r_0$ is the parameter used in the FLASH code.

## 5.1 ExMHD model tests

This section presents results of test problems that are motivated by problems suggested and simulated in article [9]. The aim of these tests is to assess the functionality of the ExMHD model implementation in the FLASH code and study the model under simplified conditions. The setups of these problems used in this thesis are very similar, however, does not match exactly. Each of the problems focuses on one of the terms in the extended-MHD model and thus provides an intuition for better understanding the terms' impact on laser plasma dynamics. While the full ExMHD model is used in these simulations, the problems are constructed so that only one effect dominates the plasma dynamics. The considered plasma conditions and problem setups provide a basic framework for the experimental measurement of selected transport coefficients.

In these problems, the laser propagates through a deuterium gas with a sub-critical density of $\rho_0 = 6.5 \times 10^{-5}\,\mathrm{g\,cm^{-3}}$. The initial temperature of the gas is set to 10 eV. For smaller temperatures $T_e < 1\,\mathrm{eV}$, the inverse Bremsstrahlung model (4.14) gives physically incorrect (too high) absorption rates and the laser beam deposits all its energy before passing the computational region. This is a limitation of the absorption model for cold and low-density plasma. Thus, preheated gas is

considered for which the model (4.14) is applicable. The ionized electron density is significantly smaller than the critical density $\frac{n_e}{n_c} \approx 0.02$, therefore the gas is underdense and the absorption rate is small. Laser energy is 50 J, wavelength is 1.055 $\mu$m and laser spatial profile is Gaussian with a standard deviation of $\sigma = 75\,\mu$m, which corresponds to FWHM $\doteq 177\,\mu$m. Laser beam duration is 0.5 ns with 0.1 ns linear rise, followed by constant time profile. Applied magnetic field magnitudes are in the range $B_0 = 0 - 5$ T and differ for each test problem based on the required conditions. In all simulations in this section, thermal and thermoelectric transport is limited with flux-limiter coefficients $f_T = f_N = 0.1$ (see Section 5.2). Further, the ideal gas equation of state with $\gamma = 5/3$ is used.

The first test problem evaluates the anisotropic thermal conduction for different values of the external magnetic field. The second and third test problems examine the advection of the magnetic field due to Nernst and cross-field Nernst terms. The last of the test problems focuses on the Righi-Leduc effect.

### 5.1.1 Anisotropic thermal conduction

In the following simulations, the laser propagates along the $z$ axis. A uniform magnetic field is applied in the direction perpendicular to the propagation of the laser (parallel to the $x$ axis). Laser deposits a small fraction of its energy (up to 5 %), symmetrically heating the subcritical gas. Four simulations were performed in computational domain of size 800 $\mu$m $\times$ 800 $\mu$m $\times$ 50 $\mu$m on 3D 128 $\times$ 128 $\times$ 4 uniform mesh with 262144 laser beam rays.

Figure 5.1 shows 2D $x - y$ slices of the electron temperature profile at the end of the laser pulse ($t = 0.5$ ns). The simulations were performed with different magnitudes of the external magnetic field to assess the impact of the field on heat conduction in the transverse direction. In the case of zero magnetic fields, the electron in the gas heats up to about 224 eV and the temperature is angularly symmetric as expected. Application of the magnetic field narrows the temperature profile along the $y$ axis and the maximum temperature in the center increases due to reduced transverse heat flux. The stronger the magnetic field, the higher the maximum temperature and the narrower temperature profile is observed. The temperature reaches 255 eV and 314 eV in the 1 T and 5 T case, respectively. Magnetization approaches values of order $\chi \approx 1$ for the 1 T case, while higher magnetizations ($\chi \geq 10$) are reached for field magnitudes 3 T and 5 T, where the temperature profile also elongates in the longitudinal direction. This is caused by increased temperature gradients due to heat confinement in the centre of the laser beam.

These results are in agreement with the physical intuition of magnetized thermal transport and with the results in the article [20], although there are slight differences as the focus of the laser is not the same.

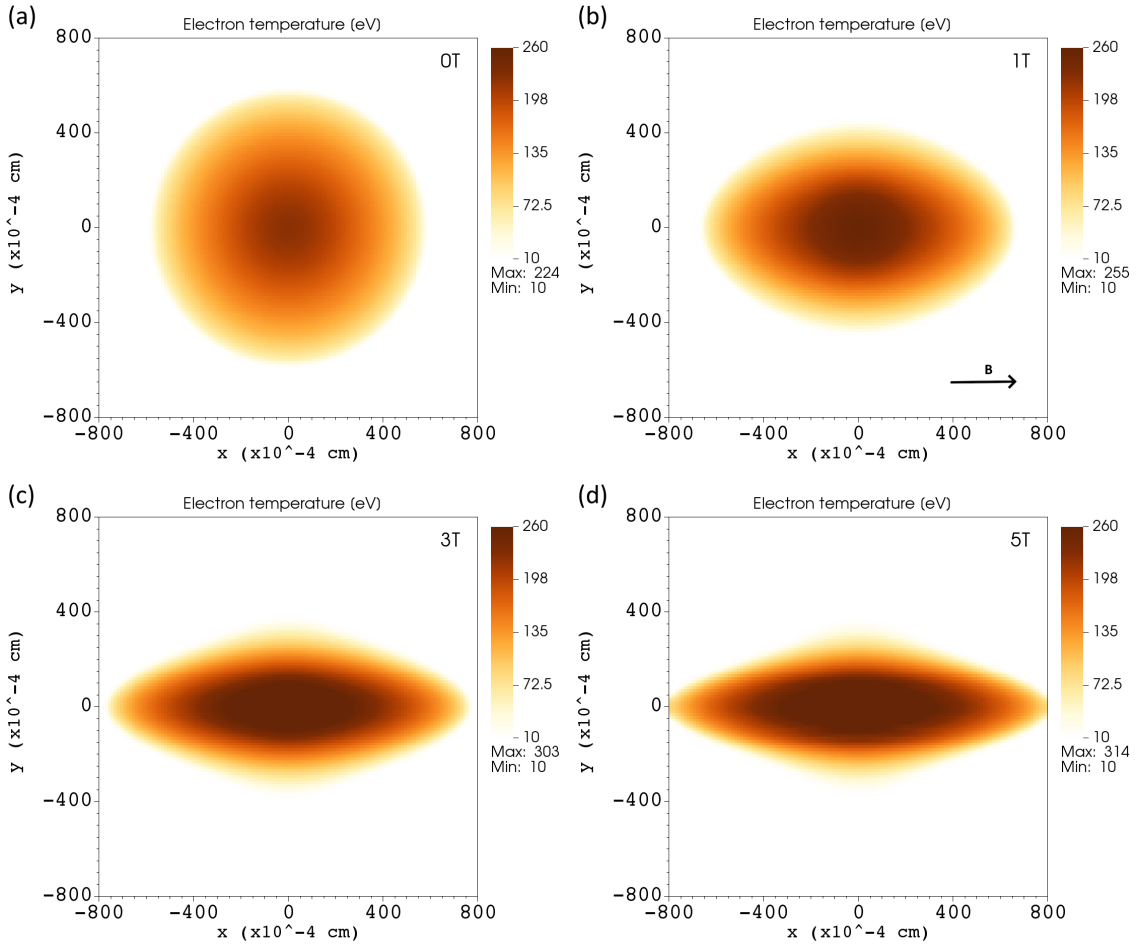


Figure 5.1: The result of anisotropic conduction test problem for different values of external magnetic field using full ExMHD model. Presented images are 2D $x - y$ slices of electron temperature profile at time $t = 0.5\,\mathrm{ns}$. External magnetic field is applied with different magnitudes in the $x$ direction: (a) 0 T, (b) 1 T, (c) 3 T and (d) 5 T.

### 5.1.2 Nernst effect

The Nernst effect test problem was simulated in 2D cylindrical geometry. The simulation was performed in computational domain of size $720\,\mu\mathrm{m} \times 1500\,\mu\mathrm{m}$ on 3D $256 \times 512$ uniform mesh with 32768 laser beam rays. Laser propagates in the $-z$ direction, in which also the uniform magnetic field of magnitude 1 T is applied. The heating of the gas in turn decreases the absorption rate and makes the plasma more transparent to the laser beam. This leads to almost uniform heating along the $z$ direction. Due to the Nernst effect, the magnetic field advects in the $-\nabla T_e$ direction and its magnitude decrease in the hotter part of the laser-heated region (close to the $z$ axis).

Figure 5.2 shows a magnetic field advected away from the heated gas and compressed at the edge of the temperature profile where it reaches the magnitude of 2 T. Maximum electron temperature is 316 eV and absorbed heat is radially transported up to $x = 360\,\mu$m. The decrease of magnetization in the hotter region leads to a further increase of the Nernst velocity, as $\gamma_\perp$ goes to $\gamma_\parallel$ for $\chi \ll 1$ (see Figure 1.2). Consequently, this results in near complete cavitation of the magnetic field in the laser-heated region. For the considered configuration, the advection due to plasma motion can be neglected compared to the Nernst effect. This is demonstrated in Figure 5.2(b), where the simulation was performed without including the Nernst term in the ExMHD model.

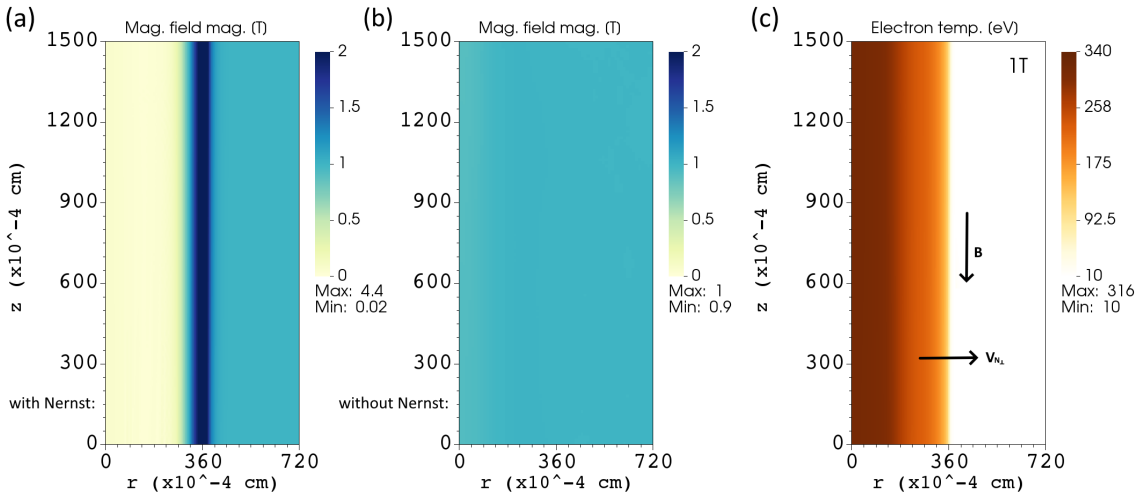


Figure 5.2: The result of Nernst effect test problem, with 1 T external magnetic field, using full ExMHD model at time $t = 0.5$ ns. (a) magnetic field magnitude with the Nernst effect. (b) magnetic field magnitude without the Nernst effect. (c) electron temperature profile with the Nernst effect.

### 5.1.3 Cross-field Nernst

The Cross-field Nernst test problem is similar to the previous problem. The simulation was again performed in computational domain of size $720\,\mu\text{m} \times 1500\,\mu\text{m}$ on 3D $256 \times 512$ uniform mesh with 32768 laser beam rays. However, the focus of the laser is modified for this problem, in order to obtain a non-zero gradient of electron temperature in the direction of the magnetic field. The focus is the same at $z = 1500\,\mu$m (FWHM $\doteq 177\,\mu$m), but the laser beam diverges so that the focus increases to FWHM $\doteq 399\,\mu$m at $z = 0\,\mu$m. The magnitude of the applied magnetic field is 3 T in $-z$ direction.

The cross-field Nernst term acts in the transverse direction to both the magnetic field and temperature gradient. The resulting effect, shown in Figure 5.3, is an angular twisting of the magnetic field in the same region where the magnetic field is

compressed by the Nernst term. The magnetic field compression at the edge of the temperature profile can be also observed, as in the previous section, with stronger compression for larger $z$ values due to increasing temperature gradient in the $z$ direction. However, the cavitation is not as strong due to increased temperature and thus magnetization close to the $z$ axis. Electron temperature reaches higher values (around 550 eV) than in the previous problem. This can be attributed to decreased transverse heat transport due to a stronger applied magnetic field.

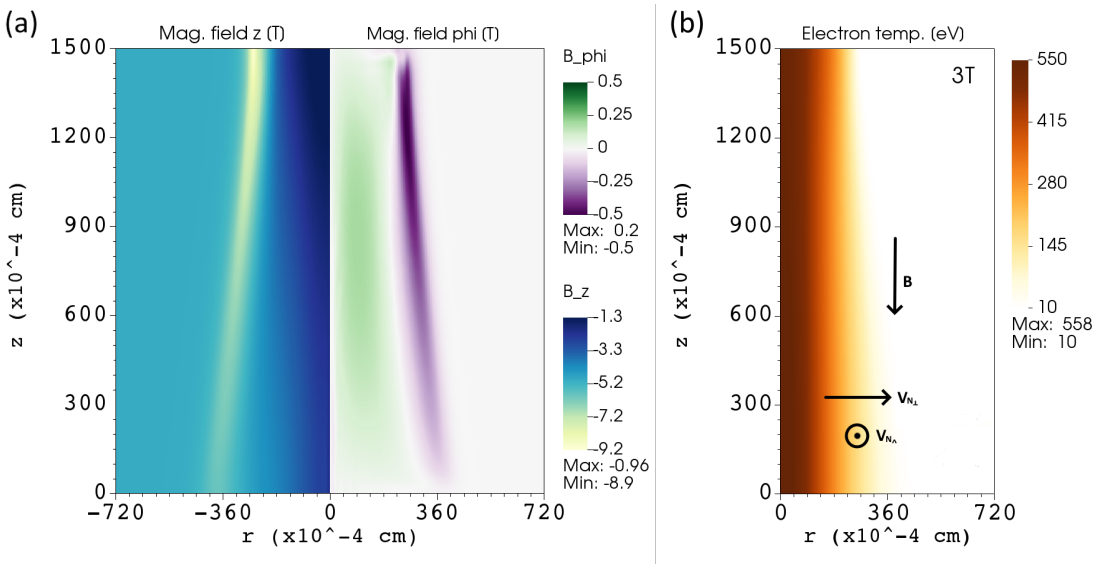


Figure 5.3: The result of Cross-field Nernst test problem, with 3 T external magnetic field, using full ExMHD model at time $t = 0.5$ ns. (a) the axial component of the magnetic field (left) and the angular component of the magnetic field (right). (b) electron temperature profile.

### 5.1.4 Righi-Leduc

The setup for the last test problem is similar to the first one. In order to observe the effect of the Righi-Leduc term in a simulation, a square-shaped laser spot is used instead of the circular one used in the previous problems. The laser focus is the same, but the circular spatial profile is cropped into a square of side length of $2\sigma = 150\,\mu$m. The applied magnetic field is again uniform with a magnitude of 1 T in $z$ direction. The simulation was performed in computational domain of size $1000\,\mu\text{m} \times 1000\,\mu\text{m} \times 20\,\mu\text{m}$ on 3D $256 \times 256 \times 4$ uniform mesh with 262144 laser beam rays.

Figure 5.4 shows the magnitude of magnetic field and temperature profile at time $t = 0.5$ ns. The temperature profile is visibly rotated more than 45° in a clockwise direction, due to the Righi-Leduc heat transport in the perpendicular direction to both the magnetic field and gradient of temperature. As in the Nernst effect test problem, the magnetic field is strongly advected away from the highly

heated region of plasma resulting in near complete cavitation. The magnetic field magnitude profile also resembles a rotated square shape. Along the edge of the cavitation region, wave-like structures are created. An instability was observed, when the stronger magnetic field was applied, which corresponds to the instability connected with Righi-Leduc and Nernst effect [47], discussed in Section 2.8. The same observation is made in [9], where the waves are also visible in the temperature profile. Thus, we conclude that the wave-like structures are created due to this unstable perturbation growth.

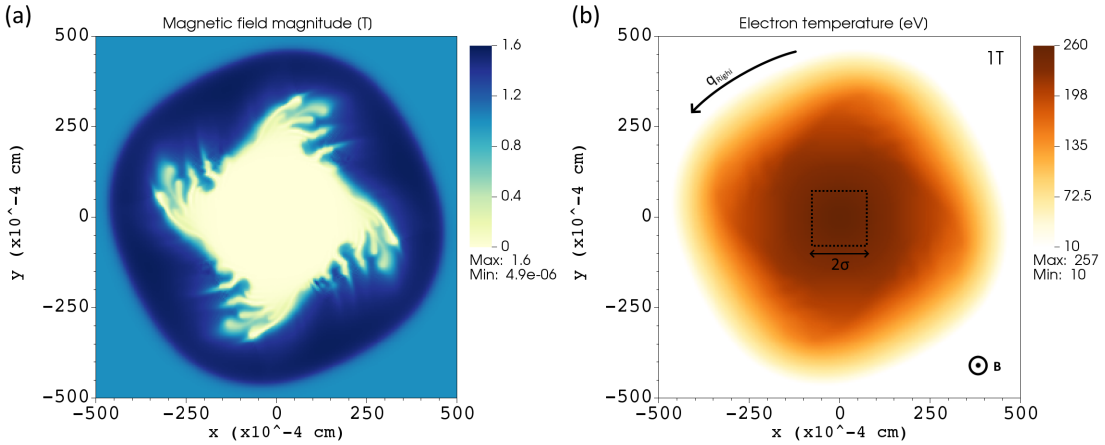


Figure 5.4: The result of Righi-Leduc test problem, with 1 T external magnetic field, using full ExMHD model at time $t = 0.5$ ns. (a) magnetic field magnitude. (b) electron temperature profile.

## 5.2 Thermoelectric terms

This section presents the results of problems that study in detail the dynamics and coupling of the Nernst terms in internal energy conservation and induction equations. In the first result (Figure 5.5), the finite element scheme from Section 3.2 was applied on model equations (3.4). The model describes two advection processes. The first one is the advection of magnetic field with the Nernst velocity $V_x^B$ and the second is the advection of temperature with velocity $V_x^T$. The scheme is implemented in standalone code using the MFEM library [51]. Simulations are performed in 2D, however, there is a symmetry along the $y$ axis and thus they are effectively 1D.

The first problem is of pure numerical character, thus the values do not have direct physical meaning. The constant Nernst coefficient is set to $\beta_\wedge = 1$ implying advection velocities of form $V_x^B = 1\frac{k_B c}{e}\partial_x T_e$ and $V_x^T = 1\frac{k_B c}{e}\partial_x B_z$ (see equations (3.5) and (3.8)). The initial state is a constant magnetic field $\boldsymbol{B} = (0, 0, 1)$ and Gaussian-shaped temperature profile with the maximum value of 1 at $x = 0.5$. Simulations were carried out in a domain of size $1 \times 1$ on uniform mesh $64 \times 64$.

Figure 5.5 shows results using the finite element framework, while Figure 5.6 shows results using the finite-volume framework used by the FLASH code. The first two plots ((a) and (b)) are the initial state at time $t = 0$, while the other two are plots of temperature and magnetic field at a later time, which differs for these two simulations as the two different schemes result in slightly different time-stepping. Both of the results show the development of instability. Due to the initial temperature gradients, the magnetic field is advected from the central region $x \approx 0.5$ (similarly as in Figure 5.2) creating a valley in the field profile. This results in non-zero $\partial_x B_z$ pointing to the middle line $x = 0.5$, thus non-zero velocity $V_x^T$ of opposite direction compared to the $V_x^B$. From this, one can intuit that any perturbation of some frequency in the temperature profile will cause perturbation in the magnetic field profile with the same frequency, but with the phase shifted by $\pi$. The perturbation in the magnetic field in turn feeds the perturbation in temperature through $V_x^T$, resulting in positive feedback and growth of both perturbations.

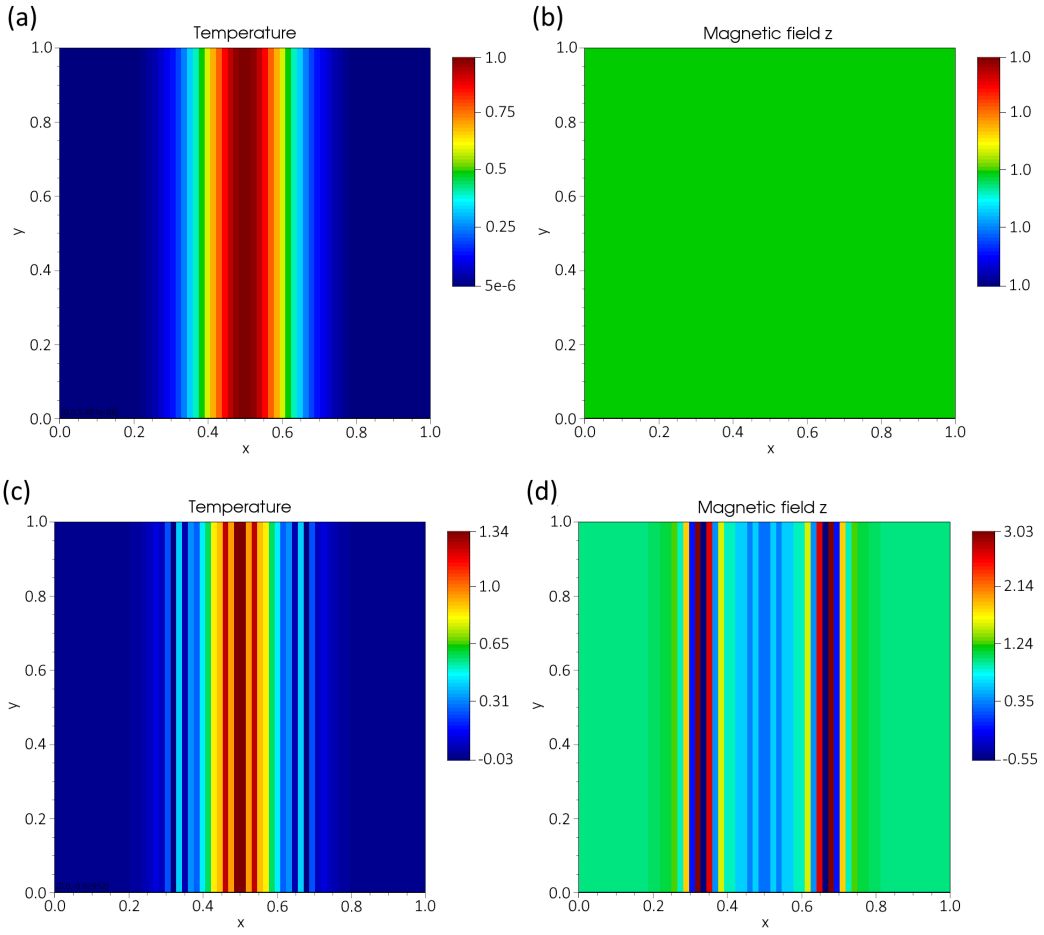


Figure 5.5: The result of the first (numerical) problem in finite element framework. Initial temperature (a) and magnetic field (b) at time $t = 0$. Temperature (c) and magnetic field (d) at time $t = 7.4 \times 10^{-7}$.

In Figure 5.5, the simulation is stopped at time $t = 7.4 \times 10^{-7}$ when strong oscillations in both profiles are visible. Figure 5.6 shows the result using the FLASH code, which due to negative temperature stops the simulation at an earlier time $t = 5.9 \times 10^{-7}$. The simulation in the FLASH code is setup to correspond to the previous one. Development of the oscillations can again be observed in the temperature and magnetic field profile.

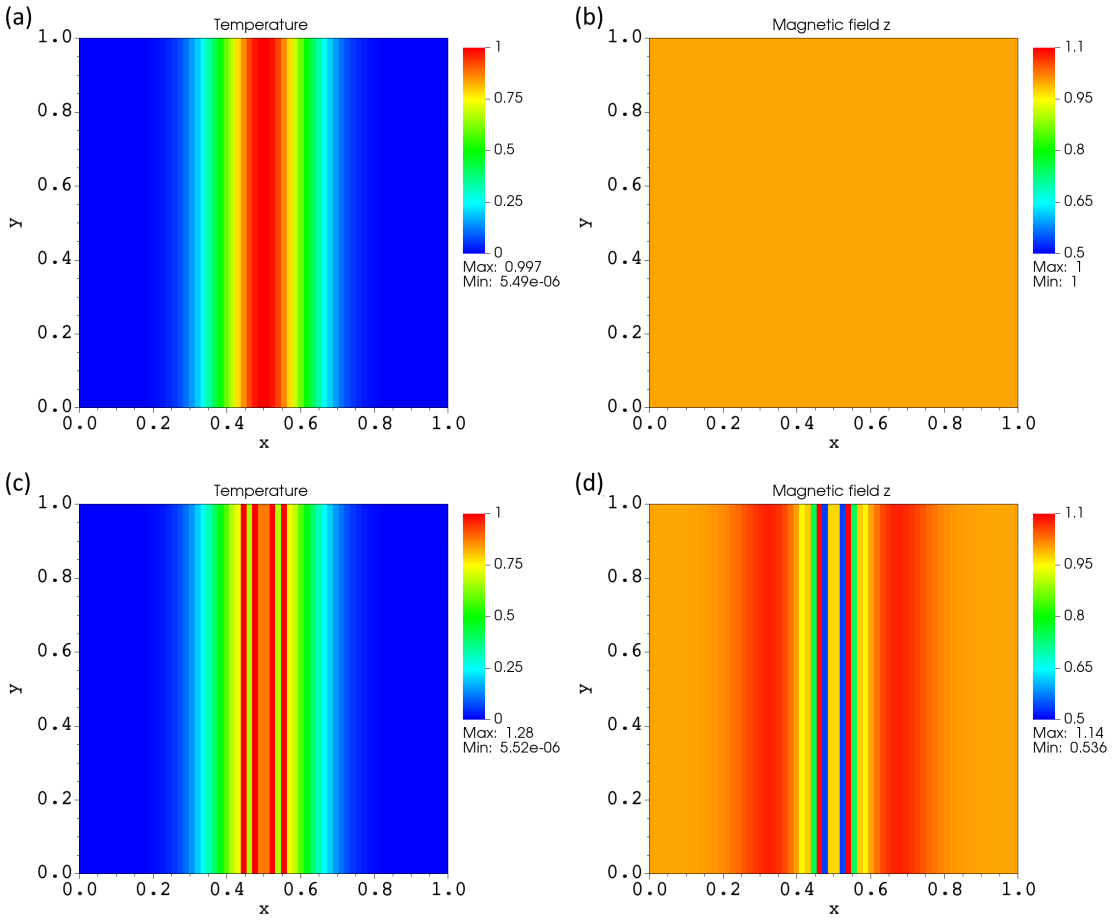


Figure 5.6: The result of the first (numerical) problem using the FLASH code. Initial temperature (a) and magnetic field (b) at time $t = 0$. Temperature (c) and magnetic field (d) at time $t = 5.9 \times 10^{-7}$.

The next two simulations utilize a modified setup in order to imitate the configuration from Section 5.1.2. However, in this modified setup, only equations (3.4) are solved, thus no laser heating and no other terms are considered. Additionally, the last problem includes thermal and magnetic diffusion. The Nernst coefficient $\beta_\wedge$ is now not constant and the initial state consists of the constant magnetic field $\boldsymbol{B} = (0, 0, 1)$ T and Gaussian shaped temperature profile imitating laser-heated low-density gas with a maximum value of $4.0 \times 10^6$ K $\approx 345$ eV at $x = 0.5$. Other parameters are the same or similar to those in the Nernst problem (Section 5.1.2).

Simulations were carried out in domain of size $144\,\mu$m $\times$ $144\,\mu$m on uniform mesh $128 \times 128$.

In Figure 5.7, the instability can also be observed. Figure 5.8 shows results for the same problem but with added thermal and magnetic diffusion terms. The diffusion dominates compared to advection velocities $V_x^B$ and $V_x^T$, and the instability does not develop in this simulation.

The instability is presumably not of numerical origin and differs from instabilities presented in Section 2.8. From the equation (2.45) one can observe that in the case of $Z = 1$, the heat flux dominates over the Nernst advection for any value of magnetization. A calculation reveals that this is also the case for $Z = 13$, although the fraction (2.45) has a slightly lower value. Thus, we conclude that this instability is not important for laser plasma, nevertheless, it provides insight into the coupling between the Nernst effect contributions to the magnetic field advection and heat flux. We utilized this knowledge in other simulations performed in this thesis for selecting the appropriate flux limiter for the Nernst advection term and the heat flux.

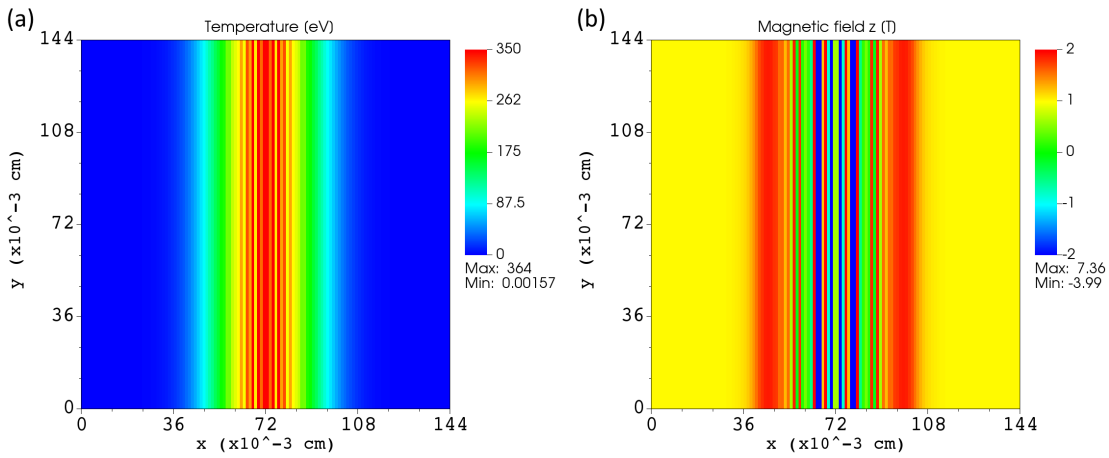


Figure 5.7: The result of the second problem without diffusion using FLASH code. Temperature (a) and magnetic field (b) at time $t = 10^{-9}$ s.

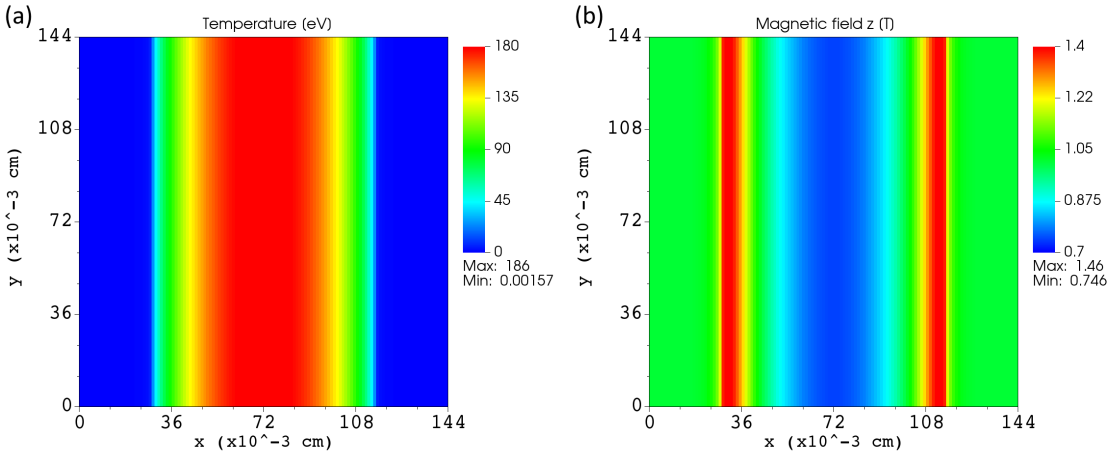


Figure 5.8: The result of the third problem with diffusion using FLASH code. Temperature (a) and magnetic field (b) at time $t = 10^{-9}$ s.

## 5.3 Laser-target simulations

All the simulations in this section are based on the laser-target problem defined in [39] that corresponds to real experiments performed at the PALS laser facility [61]. In the problem setup, laser pulse with energy 100 J and wavelength 438 $\mu$m is assumed. Laser beam irradiates solid aluminium target with 400 $\mu$m radius and 30 $\mu$m thickness. The pulse has a Gaussian profile in time with FWHM of 400 ps and is focused on the target with radius of the focal spot $r_f = 100\,\mu$m (corresponding to FWHM $\doteq 131\,\mu$m) and reaches maximum intensity (irradiance) of $1.2 \times 10^{15}$ W cm$^{-2}$ at time 400 ps. The spatial profile of the laser beam is also Gaussian. Further, the ideal gas equation of state with $\gamma = 5/3$, initial room temperature $T = 0.025$ eV and constant ionization is assumed.

In the FLASH code, the differential equations are solved in the Eulerian frame, thus a static computational mesh is employed. Due to the static mesh, additional material, into which plasma will expand, needs to be put on top of the target in the computational domain. The FLASH code allows inserting multiple different materials into the simulation domain and implements corresponding multi-material equations of state. In real experiments, the target is put in a vacuum chamber with inside pressure of order $10^{-3}$ Pa [61]. In performed simulations, the vacuum is approximated by helium gas with low density $5 \times 10^{-7}$ g cm$^{-3}$ that corresponds to pressure around 9 kPa. As is shown in the following results, the artificial vacuum causes the formation of a shock wave propagating into the helium gas in the chamber while artificially heating the surface of the plasma corona. However, as was shown in [38], this should not significantly influence the plasma evolution inside the expanding corona. Additionally, Section 2.8 showed that the more diluted part of the laser plasma is not accurately described by used transport models. Therefore, one should

be careful when interpreting the simulation results and keep in mind that profiles of the plasma dynamics inside the dense corona are better resolved.

For these parameters, the critical density is $n_c = 0.02\,\mathrm{g\,cm^{-3}}$ (for $Z = 13$). The computational domain is of size $400\,\mu\mathrm{m} \times 800\,\mu\mathrm{m}$ discretized using uniform mesh with resolution $128 \times 256$. Simulations were performed in 2D cylindrical geometry. The aluminium target is put at the bottom of the domain with a laser beam entering into the domain from above with parallel beam rays.

Heat transport is limited using flux limiter with coefficient $f_T = 0.06$ that is motivated by results of kinetic simulations of thermal transport [32]. Typical values used for the flux-limiter coefficient are from the range $(0.05 - 0.1)$. As was demonstrated in Section 5.2, instabilities can appear when the Nernst advection velocity is higher compared to the heat flux velocity. Thus, it seems reasonable to utilize the same flux-limiter coefficient for the thermoelectric terms $f_N = f_T$. This means, that we assume that the thermoelectric effect is limited in the same way as heat transport in the case of laser plasmas. However, it should be noted that this value is not based on any experimental or other findings.

In all following laser-target simulations the Hall term is neglected, as it generates high-frequency waves (see Section 2.5) in the lower density part of the plasma corona. A similar situation is for the Biermann battery term (see Section 2.6). Thus, the source version of its implementation (see Section 3.1) is adopted, which does not generate the high-frequency waves [13] and does not compute the source term at shock fronts (regions with large density gradients). Therefore, the simulation is not limited by tiny time steps that are the consequence of explicit numerical schemes for these two contributions.

The first part of this section compares different models of thermal and electric conduction in the resistive MHD with the Biermann effect framework. The second part studies the influence of the external magnetic field on the laser-plasma evolution. These results show laser-target simulations in the full extended MHD framework (except for the Hall effect). Additionally, due to the thermomagnetic instability (see Section 2.8), either the Biermann battery or the Righi-Leduc term is neglected. The instability always appeared when using both of these terms, leading to the early stopping of the simulation due to negative electron internal energy. In the last part, the hot electron model addition to the ExMHD model is presented using different simulation setups to observe its effect on the total magnetic field distribution.

All the presented figures contain profiles of given physical quantities in the computational domain at time 400 ps, corresponding to the time of maximum laser intensity. The attention is given predominantly to the comparison of magnetic field profiles between different setup cases.

### 5.3.1 Extended MHD

In this subsection, two different models for transport processes are compared with connection to the generation of magnetic field via the Biermann battery effect. The first, isotropic, transport models are based on the Spitzer's collision rate and named *SpitzerHighZ* in the FLASH code. In these, plasma with zero magnetization is assumed, thus only parallel transport coefficients are used. In these, the thermoelectric transport terms are neglected. The second, anisotropic, models are those included in the ExMHD model, presented in Chapter 1, which include complex dependences on magnetization and direction of the magnetic field. The implementation of thermal transport coefficients is based on [16] and thus called *JiHeld*, while thermoelectric and resistive coefficients are based on [17] and named *DaviesWen*. We show that the generated magnetic field through the cross-gradient term $\nabla T_e \times \nabla n_e$ greatly depends on the form of the thermal and magnetic transport terms.

Figure 5.9 shows the simulation result of the laser-target problem using the resistive MHD model with SpitzerHighZ transport models. The laser beam, with a maximum intensity of $1.2 \times 10^{15}\,\mathrm{W\,cm^{-2}}$, penetrates the plasma up to the critical surface (represented by the solid black line), where most of the laser energy is deposited and ray is reflected back into the helium gas. Heated aluminium material expands into the helium gas up to $z \approx 525\,\mu$m and $r \approx 300\,\mu$m and creates close to spherical shaped corona. Below the critical surface, a shock wave propagating into the solid target, resulting from high ablation pressure (caused by emanating material from the ablation surface), can be observed in the density profile. The electron temperature approaches values close to 2670 eV inside the corona just above the critical density surface and in the intense part of the laser beam. This hot and plume-shaped region, which has around $200\,\mu$m in diameter and in the direction away from the target, is followed by the flat region with electron temperature around 1600 eV. The ion temperature reaches only values around 1200 eV, which is less than half compared to the electron temperature, while the ion heating is approximately of spherical shape (with the centre at the critical surface at $r = 0$). At the corona surface (depicted by the solid brown line that corresponds to the isosurface with the aluminium mass fraction of 0.5), helium gas is compressed and both electrons and ions are heated to large temperatures ($\geq 10\,$keV) exceeding the temperatures inside the plasma corona. Due to the spherical-like shape of the plasma corona, gradients of electron temperature and number density are aligned further from the target (for $z \geq 200\,\mu$m). However, at the edge of the corona (for $r \approx 200\,\mu$m and $z \approx 100\,\mu$m) the density gradient is mostly axial while the temperature gradient is predominantly radial. This results in a strong generation of magnetic field via the Biermann effect, with the field reaching magnitudes around $B \approx 110\,$T in this region. The cylindrical geometry only permits the generation of the angular magnetic field, which is a direct consequence of the Biermann term form of cross gradients $\nabla T_e \times \nabla n_e$.

The generation of strong magnetic field of this form has been well known for many decades [6, 42]. This concludes the detailed description of the presented results for the first case in this subsection. For the following variations of the same problem,

only key differences will be described, as many of just described parameters are quite similar.

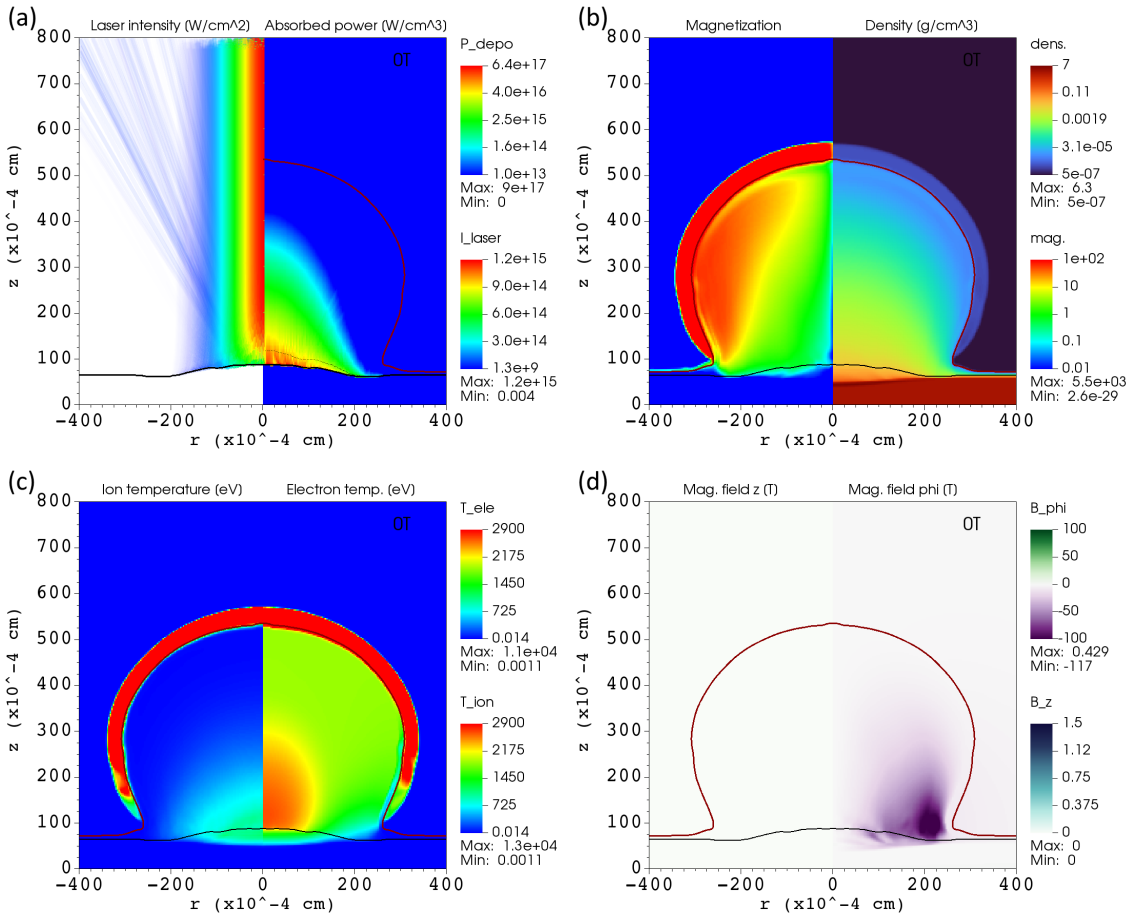


Figure 5.9: The result of the laser-target problem, at time $t = 400\,\mathrm{ps}$, using isotropic model (SpitzerHighZ) for thermal and electric conductivity, resistive MHD model with Biermann framework and 0 T external field. (a) laser intensity profile (left) and absorbed power density (right). (b) magnetization (left) and density profile (right). (c) electron (left) and ion (right) temperature. (d) axial (left) and angular (right) components of the magnetic field. The black line represents the critical surface and the brown line divides aluminium and helium plasma (isosurface of 0.5 mass fraction of aluminium).

Figure 5.10 shows the result of the simulation adopting the ExMHD model, however, only the new transport models together with Biermann battery terms are considered. In this case, the corona expands radially only up to $r \approx 260\,\mu\mathrm{m}$, making the plasma corona more plume-like. While the magnetic magnitude reaches slightly lower values of 100 T, the field generation is strong even in the region above $z \geq 200\,\mu\mathrm{m}$ and magnetic field profile is overall quite different compared to the previous case. The strong magnetic field visibly reduces the heat transport inside the corona,

and thus electron temperature attains significantly higher values around 3500 eV in the now elongated plume-shaped hot region, which stretches up to $z = 400\,\mu$m. The flat temperature region is replaced by a gradual decrease till the corona surface. All these changes result from the different transport models and we conclude that they are important for the laser plasma evolution. The strong magnetic field at the front of the corona is in better agreement with laser-target experiments [59].

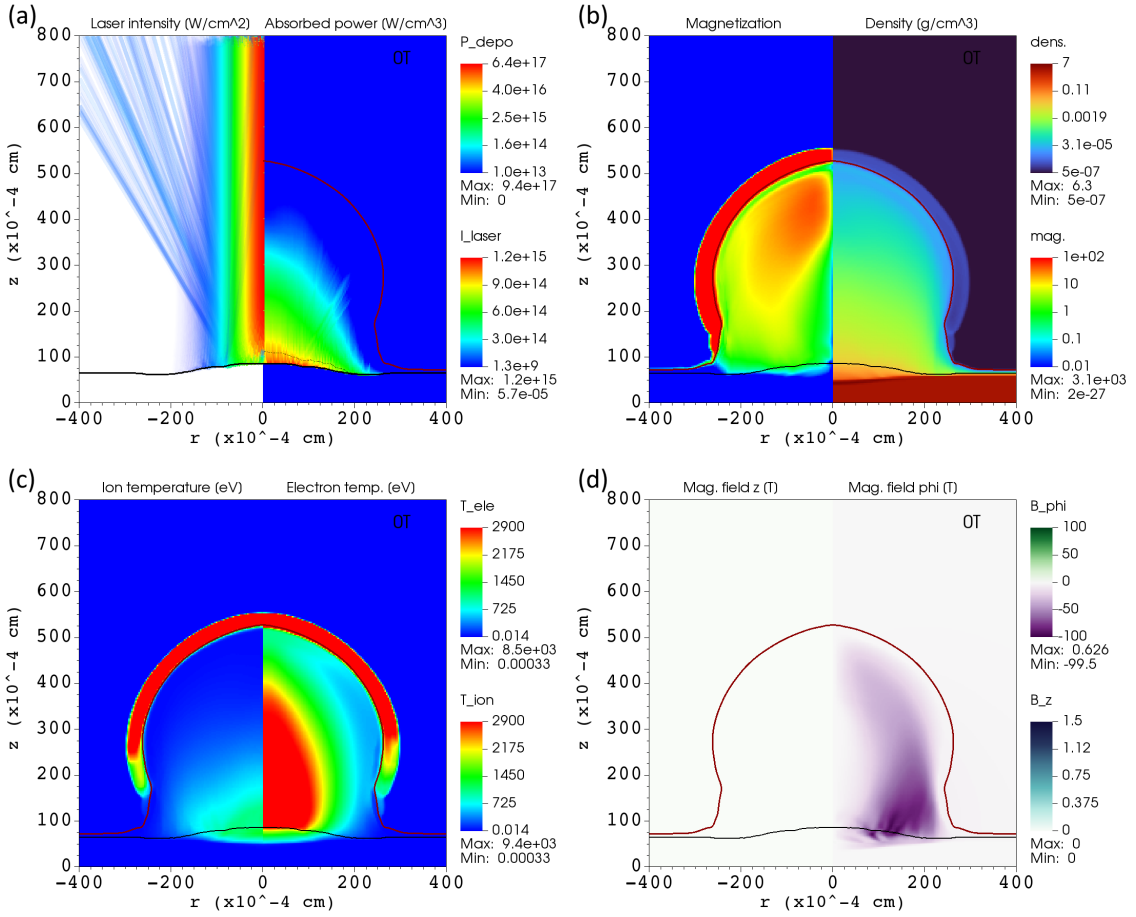


Figure 5.10: The result of the laser-target problem, at time $t = 400\,$ps, using anisotropic models (JiHeld and DaviesWen) for thermal (without Righi-Leduc) and electric conductivity, the ExMHD model with only Biermann and 0 T external field. (a) laser intensity profile (left) and absorbed power density (right). (b) magnetization (left) and density profile (right). (c) electron (left) and ion (right) temperature. (d) axial (left) and angular (right) components of the magnetic field. The black line represents the critical surface and the brown line divides aluminium and helium plasma (isosurface of 0.5 mass fraction of aluminium).

### 5.3.2 External magnetic field

In the following simulations, the full extended-MHD model is adopted, except for the Hall effect term. Due to the instabilities that can appear in plasma described by this model (see Section 2.8), we chose to consider either the Biermann effect or Righi-Leduc separately and studied the impact of those terms on laser plasma in an external magnetic field. Thus, the first two setups neglect the Righi-Leduc heat transport, while the other two neglect the generation of a magnetic field via the Biermann battery and the Seebeck effect, which also can take part in the generation of the angular magnetic field. Before the laser beam irradiates the target, an axial and uniform magnetic field of magnitude 1 T or 100 T is applied in order to examine its influence on laser-produced plasma.

#### Without Righi-Leduc effect

In Figure 5.11, the result of the case when using the full ExMHD model without Righi-Leduc and with 1 T applied magnetic field is presented. The shape of the corona is practically the same as for the case in Figure 5.10, hinting that the applied magnetic field does not significantly influence plasma expansion. However, electron temperature reaches only about 2720 eV and the plume-shaped hot region has a diameter of 360 $\mu$m (higher temperature than 2000 eV). Similarly to the Nernst effect problem simulations in Section 5.1.2, the axial component of the magnetic field is compressed and strongly advected to the edge of the plasma corona resulting in a near zero magnetic field inside the corona. At the surface of the plasma corona, we observe perturbation-like structures presumably hinting at the appearance of instability, which however could be of numerical origin. Finally, the generated angular magnetic field is also advected towards the edge of the corona together with light field compression. The key difference here, compared to Figure 5.10, is that an even stronger angular magnetic field of magnitude around 200 T is created below the critical surface and just behind the shock wave travelling into the target. This field was not observed in the previous simulations and can be explained by the combined action of the Biermann effect and Nernst effect, which advects the generated magnetic field towards the edge of the electron temperature profile (in this case in the direction of the ablation surface). The compressed magnetic field above the ablation surface suppresses the heat flux, resulting in stronger magnetic field generation, as the electron temperature gradient becomes more radial and misaligned with the electron density gradient in this region. This can be observed in the electron temperature profile when comparing Figures 5.10 and 5.11.

In conclusion, the Nernst effect significantly influences the distribution of the angular magnetic field while also inducing a strong generation below the critical surface. The external magnetic field of 1 T does not seem to significantly alter the laser plasma evolution and the result is almost the same as for zero axial magnetic fields (the result for this case is not presented in this work).

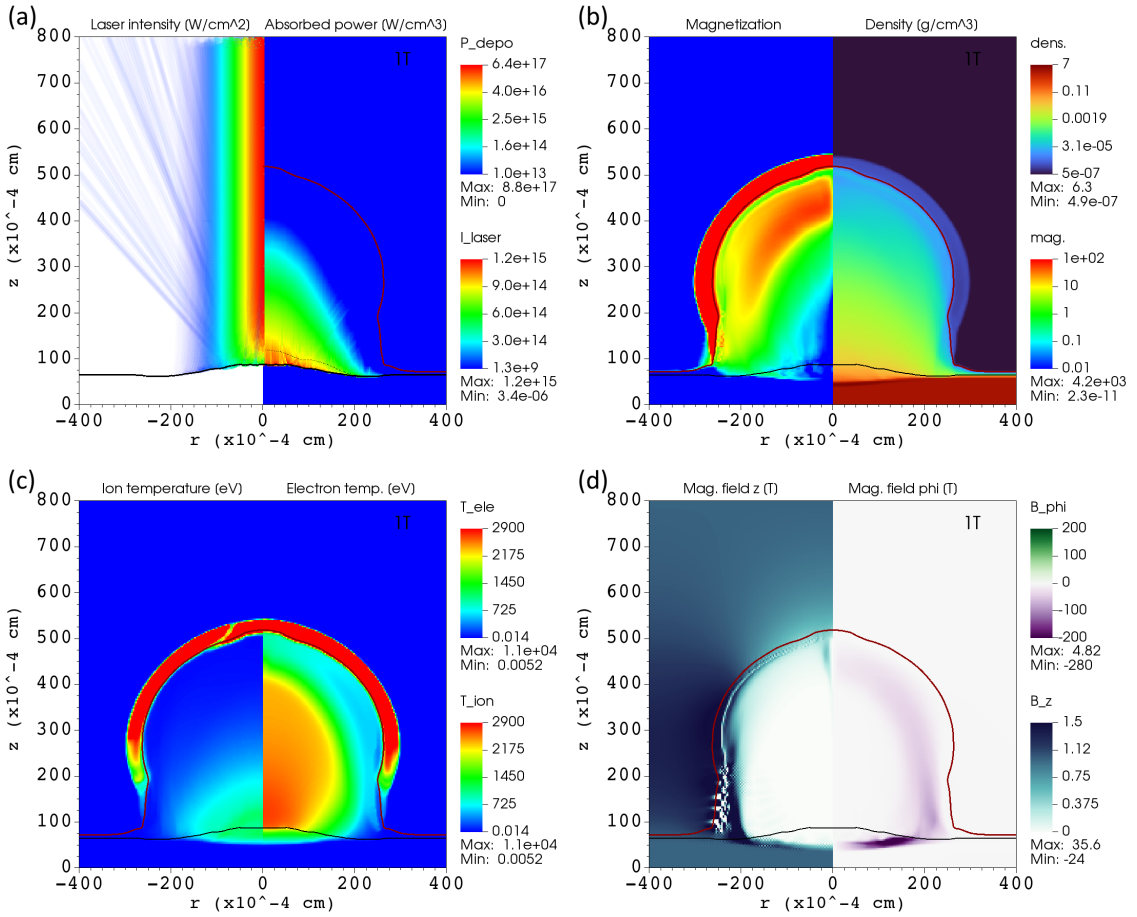


Figure 5.11: The result of the laser-target problem, at time $t = 400\,\mathrm{ps}$, using anisotropic models (JiHeld and DaviesWen) for thermal (without Righi-Leduc) and electric conductivity, the full ExMHD model and 1 T external field. (a) laser intensity profile (left) and absorbed power density (right). (b) magnetization (left) and density profile (right). (c) electron (left) and ion (right) temperature. (d) axial (left) and angular (right) components of the magnetic field. The black line represents the critical surface and the brown line divides aluminium and helium plasma (isosurface of 0.5 mass fraction of aluminium).

In Figure 5.12, the result of the case when using the full ExMHD model without Righi-Leduc and with 100 T applied magnetic field is presented. Compared to the previous case, the very strong axial magnetic field visibly alters the plasma expansion. The shape of the plasma corona is elongated in the $z$ direction and spreads up to $z \approx 580\,\mu\mathrm{m}$. Conversely, expansion in the radial direction is suppressed in the highly magnetized region of the corona (above $z \geq 300\,\mu\mathrm{m}$). Due to the increased magnetization, Nernst advection is weakened and the axial component of the magnetic field is not fully advected from inside the plasma corona. This significantly limits the heat transport in the transverse (radial) direction, resulting in higher electron temperatures of around 3020 eV near the $z$ axis. The hot region spans up to

the edge of the corona in the $z$ direction while its diameter is only around 200 $\mu$m in diameter. The angular magnetic field is also not advected and compressed at the corona edge as in the previous case (Figure 5.11) and is distributed throughout the corona in a similar fashion as in Figure 5.10. However, there are small regions in between the critical and ablation surfaces, where strong local angular fields are generated. The origins of these fields are not entirely clear.

Concluding this comparison, a very strong external field reduces the impact of the Nernst effect and significantly alters the expansion motion of the laser plasma.

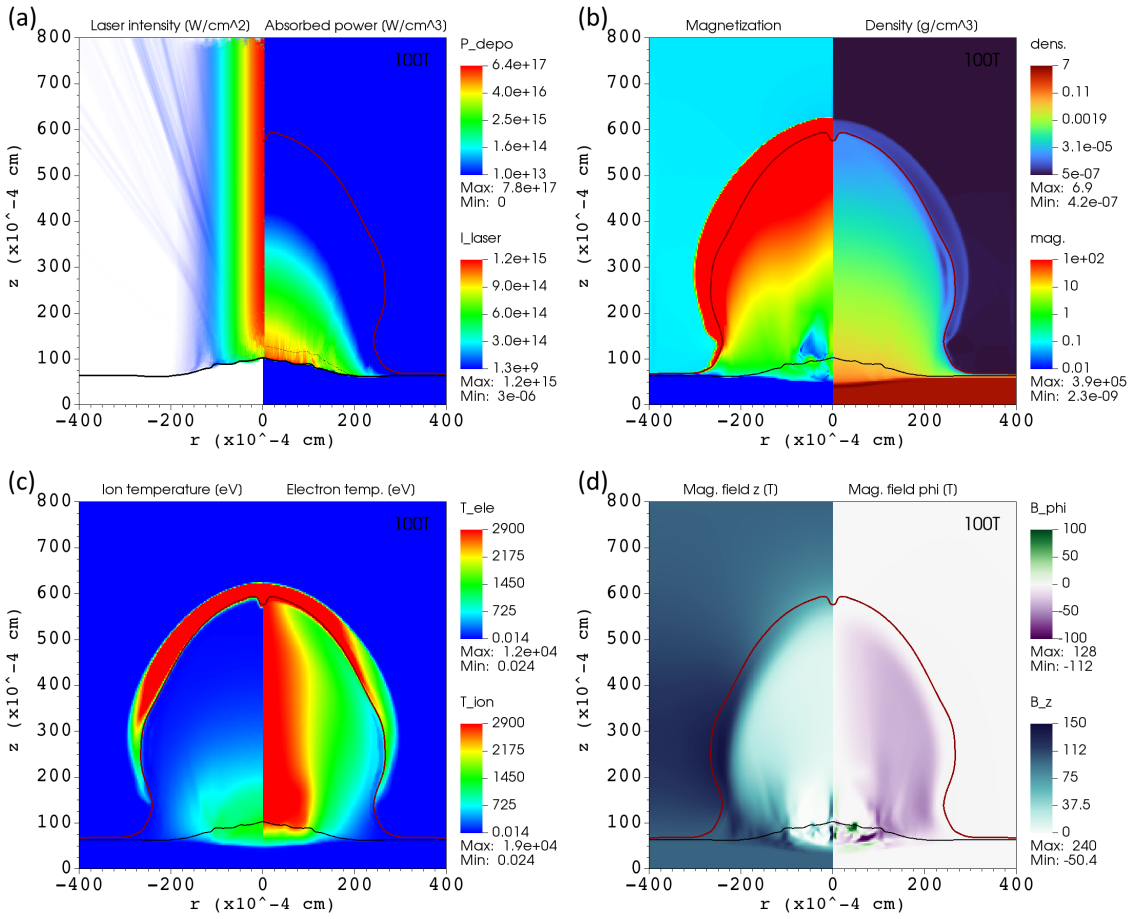


Figure 5.12: The result of the laser-target problem, at time $t = 400\,\text{ps}$, using anisotropic models (JiHeld and DaviesWen) for thermal (without Righi-Leduc) and electric conductivity, the full ExMHD model and 100 T external field. (a) laser intensity profile (left) and absorbed power density (right). (b) magnetization (left) and density profile (right). (c) electron (left) and ion (right) temperature. (d) axial (left) and angular (right) components of the magnetic field. The black line represents the critical surface and the brown line divides aluminium and helium plasma (isosurface of 0.5 mass fraction of aluminium).

### Without the Biermann battery and Seebeck effect

In Figure 5.13, the result of the case when using the full ExMHD model without Biermann battery and Seebeck effect and with 1 T applied magnetic field is presented. Without the magnetic field generating term $\nabla T_e \times \nabla n_e$, this result is more similar to the first case utilizing isotropic transport models (Figure 5.9) than to the other cases that use the ExMHD transport models (Figure 5.11). This can be interpreted as it is the interplay between the Biermann effect and the anisotropic transport coefficient that makes the difference between results in Figure 5.9 and 5.10. The ExMHD transport models depend on magnetization, while the isotropic transport models do not. The negligible influence of the axial magnetic field of 1 T is clearly visible here, as the temperature profiles and the corona shape are almost identical to the result in Figure 5.9. The axial field is again advected to the edge of the plasma corona and compared to the result in Figure 5.11, there are no visible strong perturbations along the corona surface. Thus, those perturbations are probably connected to the Biermann effect.

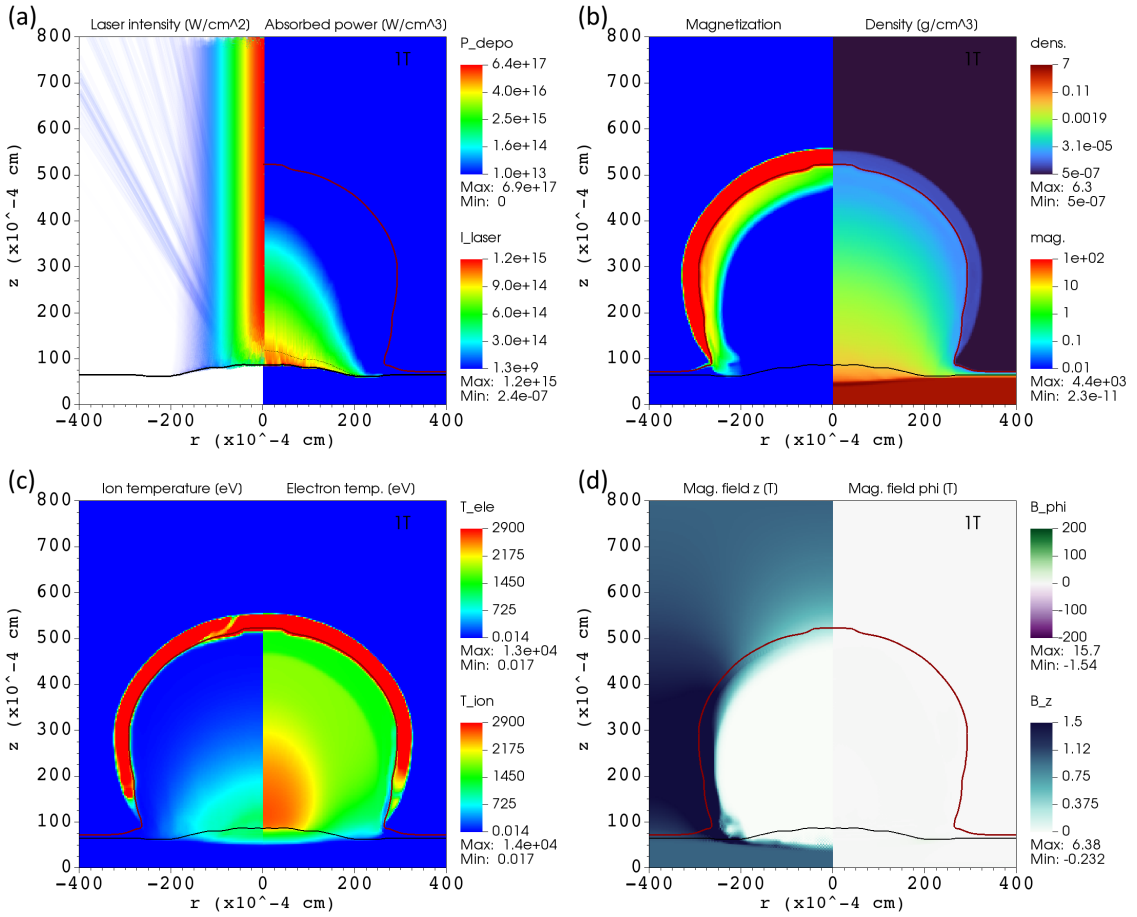


Figure 5.13: The result of the laser-target problem, at time $t = 400\,\mathrm{ps}$, using anisotropic models (JiHeld and DaviesWen) for thermal and electric conductivity, the full ExMHD model without Biermann effect and 1 T external field. (a) laser intensity profile (left) and absorbed power density (right). (b) magnetization (left) and density profile (right). (c) electron (left) and ion (right) temperature. (d) axial (left) and angular (right) components of the magnetic field. The black line represents the critical surface and the brown line divides aluminium and helium plasma (isosurface of 0.5 mass fraction of aluminium).

In Figure 5.14, the result of the case when using the full ExMHD model without Biermann battery and Seebeck effect and with 1 T applied magnetic field is presented. This result is very similar to the one in Figure 5.12. The only differences are associated with the absence of an angular magnetic field. The reached electron temperatures are slightly lower (3060 eV) and the hot region is wider as there is no angular field to limit the radial heat flux. However, at the critical surface, the hot region is actually narrower and rotated clockwise under the critical surface. This presumably arises due to the Righi-Leduc term, which is significant for large electron temperature gradients and magnetization of around $\chi \approx 1$. Figure 5.14 shows, that this is really the case (see panels (b) and (c)). Despite neglecting the magnetic field

generation terms, strong angular magnetic fields appear in the region between critical and ablation surfaces. This magnetic field points mainly in the opposite direction compared to the Biermann-generated angular magnetic field. The conditions in this region also play in hand to the Cross-Nernst term, as the magnetization values and strong electron temperature gradients allow this term to twist (advect in transverse direction to the field) the axial magnetic field creating the angular components (see Section 5.1.3). Therefore, this explains the observed angular magnetic field. As the magnetic field seems to be compressed just above the ablation surface, there could also be some interplay together with the Nernst effect. In this case, these findings are just an attempt for interpretation and the mechanism that leads to the creation of this field is not studied in detail here.

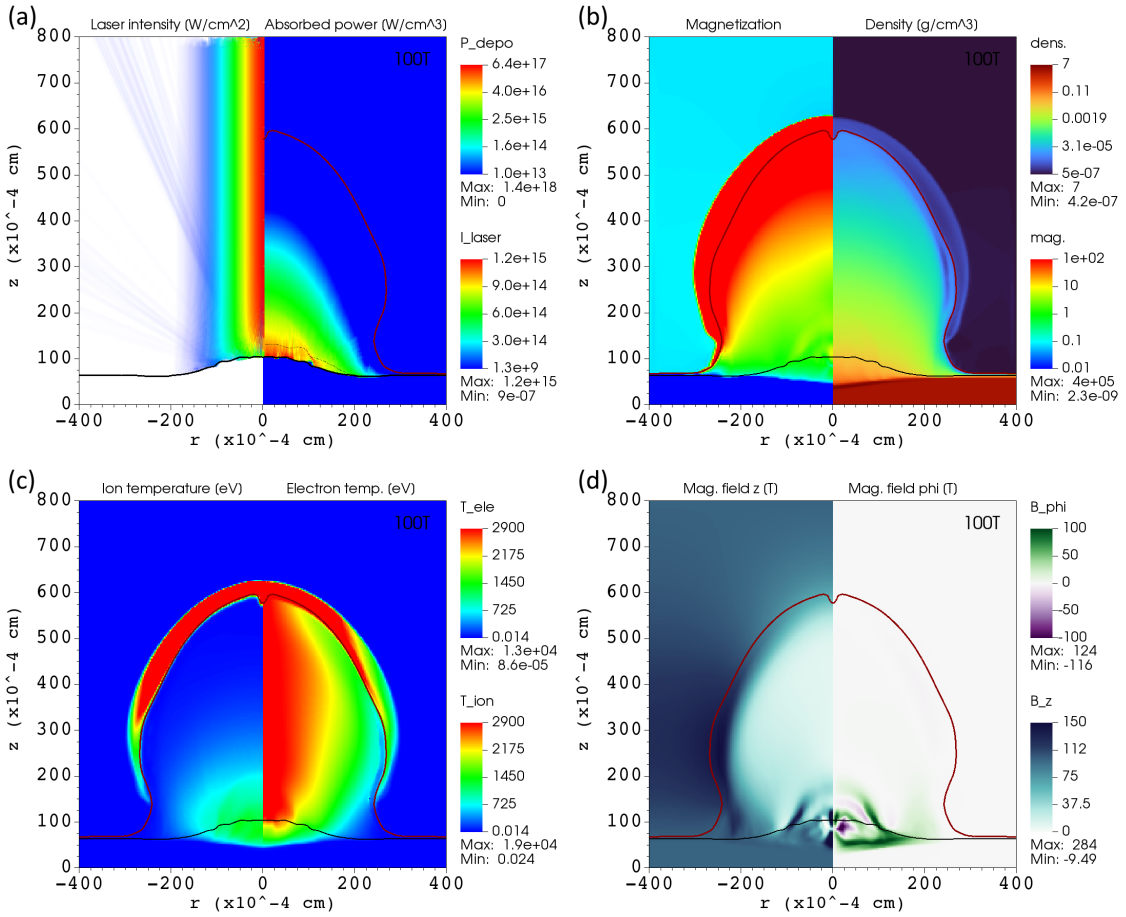


Figure 5.14: The result of the laser-target problem, at time $t = 400\,\mathrm{ps}$, using anisotropic models (JiHeld and DaviesWen) for thermal and electric conductivity, the full ExMHD model without Biermann effect and 100 T external field. (a) laser intensity profile (left) and absorbed power density (right). (b) magnetization (left) and density profile (right). (c) electron (left) and ion (right) temperature. (d) axial (left) and angular (right) components of the magnetic field. The black line represents the critical surface and the brown line divides aluminium and helium plasma (isosurface of 0.5 mass fraction of aluminium).

### 5.3.3 Hot electrons

The following simulations are motivated by [55], where simple addition of hot electron current into the MHD model is demonstrated. We used the same method, which was described in detail in Section 4.4.1, to add the hot electron current into the ExMHD model. The hot electron temperature of $T_h \approx 5\,\mathrm{keV}$ is estimated using relation for short pulses (4.20) and is considered to be constant along the critical surface. This approximation of constant hot electron temperature is chosen in order to simplify the implementation and due to the observation that electron tempera-

ture is mostly constant along the critical surface in the region of large laser intensity. Moreover, the absorption fraction is set to $\eta_a = 2 \times 10^{-3}$ (estimated according to experimental results in [60]) and leads to similar hot electron currents values as in [55] that significantly influence magnetic field distribution. The added current direction is constant and only axial, which results in the generation of only an angular magnetic field and is inserted only inside the plasma corona. Correspondingly to [55], only the current of hot electrons moving against the laser beam (in $z$ direction) from the critical surface is considered here. Finally, the anomalous resistivity is also considered (see Section 4.3), which increases resistivity in the low-density region of the plasma corona, allowing a stronger field, resulting from the hot electron current, to develop. In [55] was demonstrated, that without anomalous resistivity, the generated magnetic field is negligible. Thus, it is considered in all simulations in this section. Additionally, no external magnetic field is applied here.

Figure 5.15 shows the case of using the isotropic transport models in resistive MHD with the Biermann effect. This result is now compared to the one in Figure 5.9. The laser plasma expansion is slightly suppressed in both radial and axial direction with the surface reaching $r \approx 275\,\mu$m and $z \approx 480\,\mu$m. This can be attributed to the newly present angular field, which fills the front region of the corona where the Biermann magnetic field is not present. Maximum electron temperature reaches around 2620 eV. The hot electron current attains values of $1.35\,\mathrm{A\,m^{-2}}$ and introduces (through magnetic diffusion) a return current of the opposite direction carried by cold electrons inside the plasma. This return current then generates a corresponding field in the opposite direction compared to the cross-gradient magnetic field, which reaches magnitudes of about 60 T. The separation of these differently produced magnetic fields is visible in the magnetization profile where the isosurface of the zero magnetization line can be observed.

In conclusion, the hot electron current slightly alters the expansion rate and introduces a magnetic field in the front of the plasma corona of similar strength and opposite direction to the Biermann magnetic field. These findings are in agreement with the results in [55]. Although we have considered significantly different laser-target problem configurations, the character of the field generated by the hot electron current is very similar.

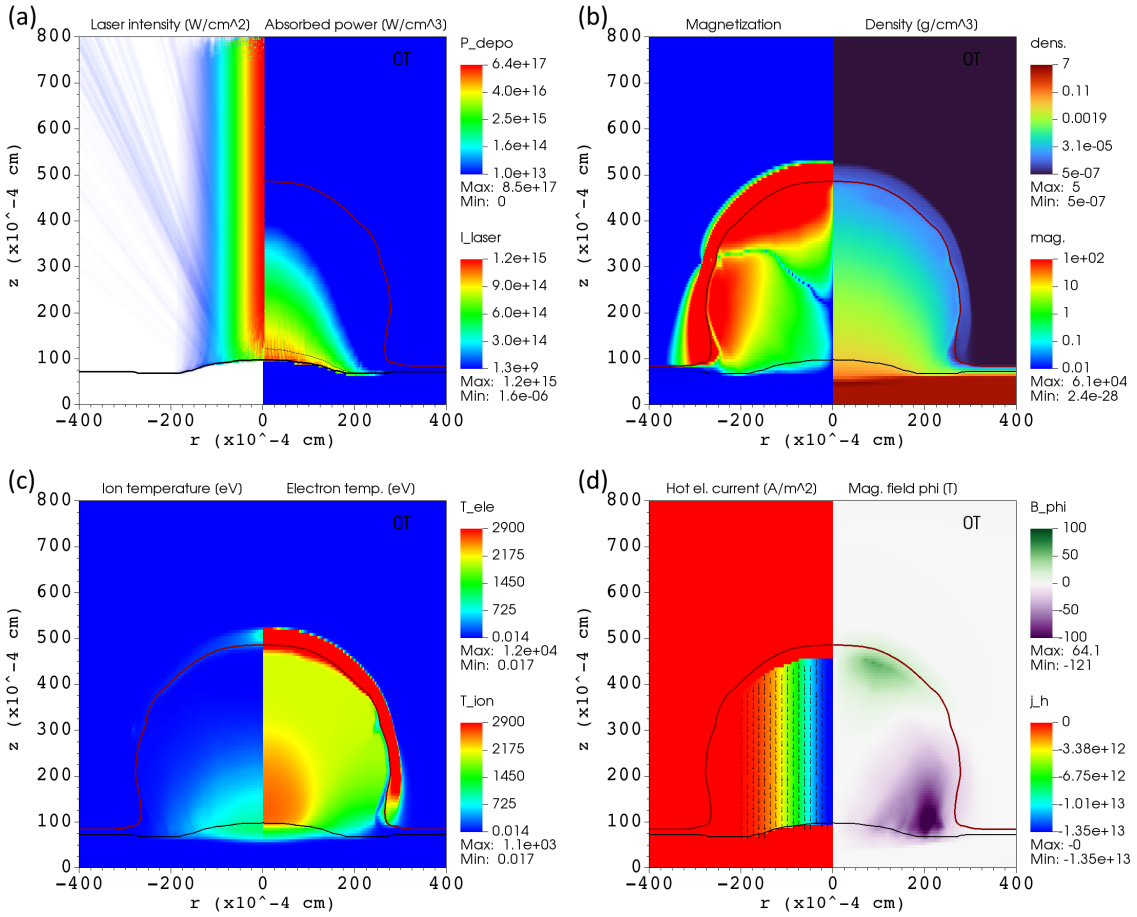


Figure 5.15: The result of the laser-target problem, at time $t = 400\,\text{ps}$, using isotropic model (SpitzerHighZ) for thermal and electric conductivity, resistive MHD model with Biermann effect. (a) laser intensity profile (left) and absorbed power density (right). (b) magnetization (left) and density profile (right). (c) electron (left) and ion (right) temperature. (d) axial (left) and angular (right) components of the magnetic field. The black line represents the critical surface and the brown line divides aluminium and helium plasma (isosurface of 0.5 mass fraction of aluminium).

In Figure 5.16, the result of the case when using anisotropic transport models in the ExMHD model with just the Biermann battery and without Righi-Leduc and with added hot electron current. Similarly to the previous case, the expansion is slightly suppressed in both radial and axial directions compared to the result in Figure 5.10. Maximum electron temperature reaches around 3300 eV. The hot electron current generates a magnetic field of slightly lower magnitude of around 50 T, which arises from the opposite direction compared to the Biermann magnetic field, which in this case reaches up to the front of the plasma corona. In conclusion, the only visible effect of the hot electron current is the reduced expansion and altered distribution of the magnetic field.

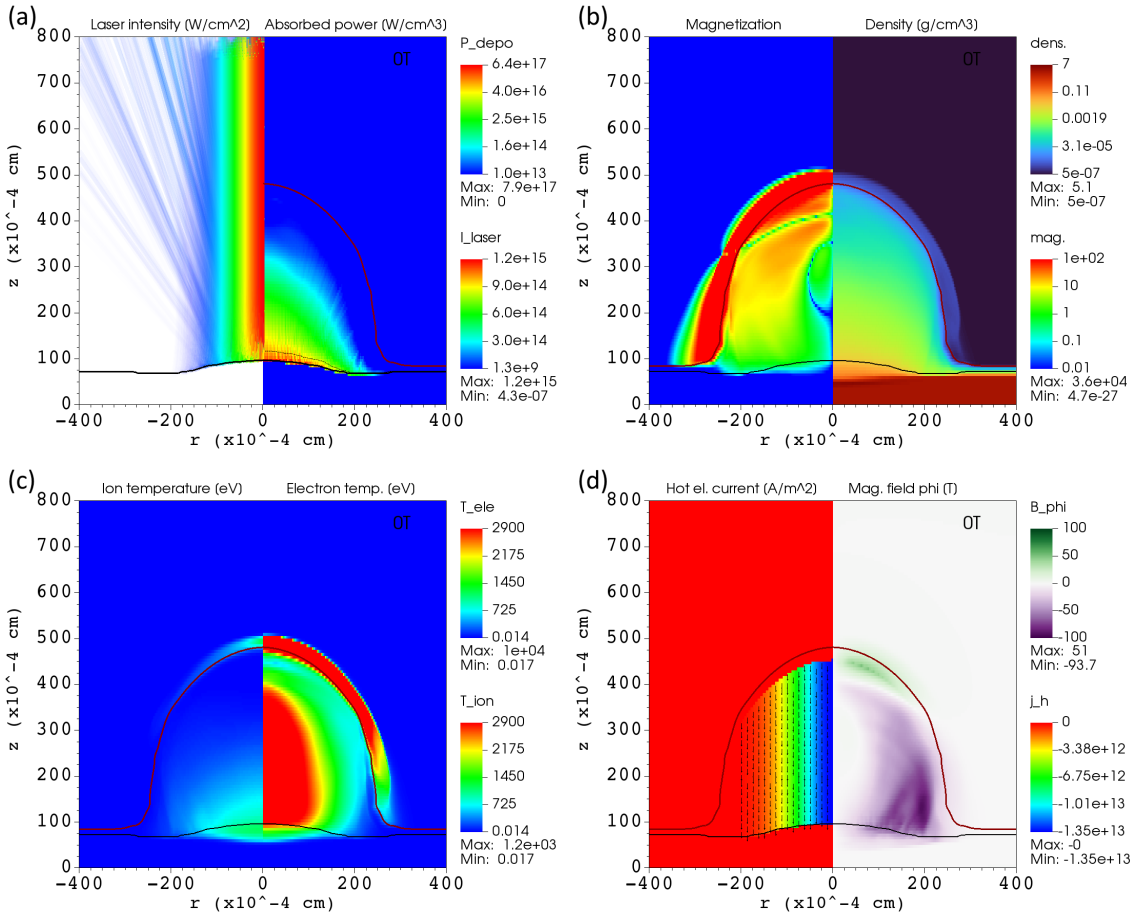


Figure 5.16: The result of the laser-target problem, at time $t = 400\,\mathrm{ps}$, using anisotropic models (JiHeld and DaviesWen) for thermal and electric conductivity, resistive MHD model with Biermann effect. (a) laser intensity profile (left) and absorbed power density (right). (b) magnetization (left) and density profile (right). (c) electron (left) and ion (right) temperature. (d) axial (left) and angular (right) components of the magnetic field. The black line represents the critical surface and the brown line divides aluminium and helium plasma (isosurface of 0.5 mass fraction of aluminium).

Figure 5.17 shows the result of the case when using the full ExMHD model without Righi-Leduc and with added hot electron current. As in previous cases, the expansion is reduced in both directions. Maximum electron temperature reaches around 2640 eV. The axial magnetic field, generated by cross-gradients, has a similar shape as in Figure 5.11, however, is reduced in the front of the plasma corona where the magnetic field from the hot electron current acts in the opposite direction and reaches 50 T. Compared to the previous case (Figure 5.16), this field is slightly more spread out along the corona front, presumably due to the magnetic field advection via the Nernst effect.

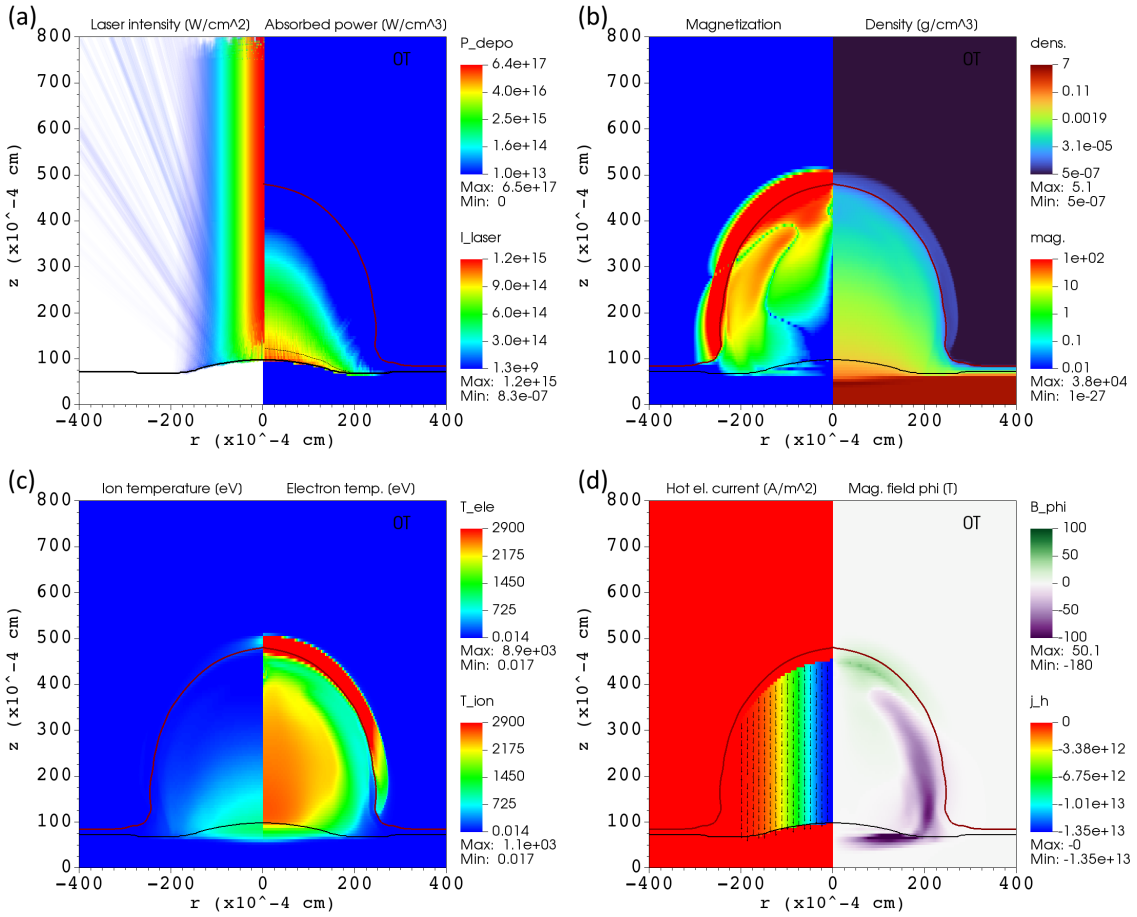


Figure 5.17: The result of the laser-target problem, at time $t = 400\,\mathrm{ps}$, using anisotropic models (JiHeld and DaviesWen) for thermal and electric conductivity, full ExMHD model. (a) laser intensity profile (left) and absorbed power density (right). (b) magnetization (left) and density profile (right). (c) electron (left) and ion (right) temperature. (d) axial (left) and angular (right) components of the magnetic field. The black line represents the critical surface and the brown line divides aluminium and helium plasma (isosurface of 0.5 mass fraction of aluminium).

# Conclusions

In this thesis, the extended-MHD model was studied in detail theoretically and by performing numerous laser plasma and laser-target simulations. The focus was on testing the newly added terms to the already present resistive MHD model in the FLASH code and on the analysis of acquired numerical results.

In the first part, various test problems including low-density laser plasma were simulated to assess the implementation of the added transport coefficients into the code. The individual impacts of different effects on laser-produced plasma were presented. Concretely, the cavitation of the magnetic field in the laser plasma due to the Nernst advection term together with magnetic field twisting, which results from aligned temperature gradient and magnetic field, was observed under appropriate plasma conditions. Further, the impact of anisotropic thermal transport in an external magnetic field was analysed. The development of an instability connected to the Righi-Leduc and Nerst effect was examined.

Secondly, a custom numerical scheme for the Nernst effect terms was introduced in order to study the coupling between the induction and electron internal energy conservation equation in detail. This novel scheme also presents the advantages of the finite element method, which allows the construction of a numerical scheme of arbitrary order. The examination of the Nernst effect showed a kind of instability that we have not found in literature yet. However, it was demonstrated that this instability is presumably not important for simulations related to ICF.

The last part consisted of numerous simulations of laser-target interaction in either an external magnetic field or with an addition of hot electron current. The influence of the added magnetic field, together with the inducted ones, on the plasma corona dynamics was studied in detail. The simulations showed that the external magnetic field influences the target expansion only for large magnitudes of order 100 T. The impact of the anisotropic transport, Nernst advection and Righi-Leduc term on angular magnetic field distribution was examined. The generation of the magnetic field by the added hot electron current was assessed together with the Biermann battery effect.

The magnetohydrodynamic model has been used for decades to model plasma dynamics. However, recent developments and extensions of the model bring new numerical challenges and there is still a lot to be done to obtain a robust model that describes magnetized laser plasma dynamics. Advances in this field could allow a better understanding, of how plasma behaves under extreme conditions and mitigate unwanted instabilities and other complications in ICF.

# Bibliography


[1] S. Atzeni, J. M. ter Vehn, The Physics of Inertial Fusion, repr Edition, Oxford science publications, Oxford University Press, Oxford [u.a.], 2004. doi:10.1093/acprof:oso/9780198562641.001.0001.

[2] Y. Wang, D. W. Hahn, A simple finite element model to study the effect of plasma plume expansion on the nanosecond pulsed laser ablation of aluminum, Applied Physics A 125 (9) (aug 2019). doi:10.1007/s00339-019-2951-8.

[3] C. Fendt, Mhd simulations of star-disk magnetospheres and the formation of outflows and jets, Proceedings of the International Astronomical Union 3 (S243) (2007) 265–276. doi:10.1017/s1743921307009623.

[4] H. Alfvén, Existence of Electromagnetic-Hydrodynamic Waves, Nature 150 (3805) (1942) 405–406. doi:10.1038/150405d0.

[5] L. Gao, E. Liang, Y. Lu, R. K. Follet, et al., Mega-Gauss Plasma Jet Creation Using a Ring of Laser Beams, The Astrophysical Journal 873 (2) (2019) L11. doi:10.3847/2041-8213/ab07bd.

[6] M. G. Haines, Magnetic-field generation in laser fusion and hot-electron transport, Canadian Journal of Physics 64 (8) (1986) 912–919. doi:10.1139/p86-160.

[7] C. Graziani, P. Tzeferacos, D. Lee, D. Q. Lamb, et al., The Biermann Catastrophe In Numerical Magnetohydrodynamics, The Astrophysical Journal 802 (1) (2015) 43. doi:10.1088/0004-637x/802/1/43.

[8] J. D. Moody, B. B. Pollock, H. Sio, D. J. Strozzi, et al., Increased Ion Temperature and Neutron Yield Observed in Magnetized Indirectly Driven D2-Filled Capsule Implosions on the National Ignition Facility, Physical Review Letters 129 (19) (2022) 195002. doi:10.1103/physrevlett.129.195002.

[9] C. A. Walsh, J. P. Chittenden, D. W. Hill, C. Ridgers, Extended-magnetohydrodynamics in under-dense plasmas, Physics of Plasmas 27 (2) (Feb. 2020). doi:10.1063/1.5124144.

[10] H. C. Watkins, R. J. Kingham, Magnetised thermal self-focusing and filamentation of long-pulse lasers in plasmas relevant to magnetised ICF experiments, Physics of Plasmas 25 (9) (2018) 092701. doi:10.1063/1.5049229.

[11] A. Y. Chirkov, S. V. Ryzhkov, The Plasma Jet/Laser Driven Compression of Compact Plasmoids to Fusion Conditions, Journal of Fusion Energy 31 (1) (2011) 7–12. doi:10.1007/s10894-011-9411-6.

[12] V. T. Tikhonchuk, M. Bailly-Grandvaux, J. J. Santos, A. Poyé, Quasistationary magnetic field generation with a laser-driven capacitor-coil assembly, Physical Review E 96 (2) (2017) 023202. doi:10.1103/physreve.96.023202.

[13] FLASH User's Guide Version 4.7., University of Rochester, 1st Edition (2023). URL https://flash.rochester.edu/site/flashcode/

[14] E. F. Toro, Riemann Solvers and Numerical Methods for Fluid Dynamics, Springer Berlin Heidelberg, 2009. doi:10.1007/b79761.

[15] S. I. Braginskii, Transport processes in a plasma, Reviews of Plasma Physics 1 (1965) 205, edited by M. A. Leontovich (Consultants Bureau, New York, 1965).

[16] J.-Y. Ji, E. D. Held, Closure and transport theory for high-collisionality electron-ion plasmas, Physics of Plasmas 20 (4) (2013) 042114. doi:10.1063/1.4801022.

[17] J. R. Davies, H. Wen, J.-Y. Ji, E. D. Held, Transport coefficients for magnetic-field evolution in inviscid magnetohydrodynamics, Physics of Plasmas 28 (1) (Jan. 2021). doi:10.1063/5.0023445.

[18] J. D. Sadler, C. A. Walsh, H. Li, Symmetric set of transport coefficients for collisional magnetized plasma, Physical Review Letters 126 (7) (2021) 075001. doi:10.1103/physrevlett.126.075001.

[19] E. M. Epperlein, M. G. Haines, Plasma transport coefficients in a magnetic field by direct numerical solution of the Fokker–Planck equation, Physics of Fluids 29 (4) (1986) 1029. doi:10.1063/1.865901.

[20] C. Walsh, J. Sadler, J. Davies, Updated magnetized transport coefficients: impact on laser-plasmas with self-generated or applied magnetic fields, Nuclear Fusion 61 (11) (2021) 116025. doi:10.1088/1741-4326/ac25c1.

[21] S. M. Copplestone, M. Pfeiffer, S. Fasoulas, C.-D. Munz, High-order Particle-In-Cell simulations of laser-plasma interaction, The European Physical Journal Special Topics 227 (14) (2019) 1603–1614. doi:10.1140/epjst/e2019-800160-y.

[22] O. Klimo, J. Psikal, J. Limpouch, V. T. Tikhonchuk, Monoenergetic ion beams from ultrathin foils irradiated by ultrahigh-contrast circularly polarized laser pulses, Physical Review Special Topics - Accelerators and Beams 11 (3) (2008) 031301. doi:10.1103/physrevstab.11.031301.

[23] D. Wu, X. T. He, W. Yu, S. Fritzsche, Particle-in-cell simulations of laser–plasma interactions at solid densities and relativistic intensities: the role of atomic processes, High Power Laser Science and Engineering 6 (2018). doi:10.1017/hpl.2018.41.

[24] D. R. Nicholson, Introduction to plasma theory, Wiley series in plasma physics, Wiley & Sons, New York u.a., 1983, literaturangaben.

[25] S. Chapman, T. G. Cowling, The Mathematical Theory of Non-uniform Gases, Cambridge University Press, 1991.

[26] G. Belmont, R. Grappin, F. Mottez, F. Pantellini, et al., Collisionless Plasmas in Astrophysics, Wiley & Sons, Incorporated, John, Hoboken, New Jersey, 2014.

[27] A. Alvarez-Laguna, N. Ozak, A. Lani, N. N. Mansour, et al., A Versatile Numerical Method for the Multi-Fluid Plasma Model in Partially- and Fully-Ionized Plasmas, Journal of Physics: Conference Series 1031 (2018) 012015. doi:10.1088/1742-6596/1031/1/012015.

[28] F. F. Chen, Introduction to Plasma Physics and Controlled Fusion, Springer London, Limited, 2016. doi:10.1007/978-3-319-22309-4.

[29] S. Galtier, Introduction to Modern Magnetohydrodynamics, Cambridge University Press, Cambridge, 2016. doi:10.1017/cbo9781316665961.

[30] S. Eliezer, The Interaction of High-Power Lasers with Plasmas, Series in plasma physics, Taylor & Francis Group, Bristol, 2002.
URL http://site.ebrary.com/lib/alltitles/docDetail.action?docID=10144639

[31] Y. Komatsu, T. Sasaki, T. Kikuchi, N. Harada, et al., Changes of implosion dynamics derived by difference of equation of state, EPJ Web of Conferences 59 (2013) 04010. doi:10.1051/epjconf/20135904010.

[32] R. P. Drake, High-Energy-Density Physics, second edition Edition, Graduate Texts in Physics, Springer-Verlag GmbH, 2018. doi:10.1007/978-3-319-67711-8.

[33] S. P. Lyon, J. D. Johnson, Sesame: the Los Alamos National Laboratory equation of state database, Technical Report LA-UR-92-3407, Los Alamos (1992).

[34] R. M. More, K. H. Warren, D. A. Young, G. B. Zimmerman, A new quotidian equation of state (QEOS) for hot dense matter, Physics of Fluids 31 (10) (1988) 3059. doi:10.1063/1.866963.

[35] L. Spitzer, R. Härm, Transport Phenomena in a Completely Ionized Gas, Physical Review 89 (5) (1953) 977–981. doi:10.1103/physrev.89.977.

[36] Y. T. Lee, R. M. More, An electron conductivity model for dense plasmas, Physics of Fluids 27 (5) (1984) 1273. doi:10.1063/1.864744.

[37] J.-Y. Ji, E. D. Held, Ion closure theory for high collisionality revisited, Physics of Plasmas 22 (6) (Jun. 2015). doi:10.1063/1.4922755.

[38] J. Löffelmann, Eulerovské modelování interakce laserového záření s plazmatem, bachelor thesis, České vysoké učení technické v Praze, Fakulta jaderná a fyzikálně inženýrská, Katedra fyzikální elektroniky, Praha (2021).

[39] J. Velechovský, Modelování absorpce laserového záření v plazmatu, výzkumný úkol, České vysoké učení technické v Praze, Fakulta jaderná a fyzikálně inženýrská, Katedra fyzikální elektroniky, Praha (2010).

[40] M. Sherlock, J. Bissell, Suppression of the biermann battery and stabilization of the thermomagnetic instability in laser fusion conditions, Physical Review Letters 124 (5) (2020) 055001. doi:10.1103/physrevlett.124.055001.

[41] J. D. Huba, Hall Magnetohydrodynamics - A Tutorial, Springer Berlin Heidelberg, pp. 166–192. doi:10.1007/3-540-36530-3_9.

[42] S. Atzeni, The physical basis for numerical fluid simulations in laser fusion, Plasma Physics and Controlled Fusion 29 (11) (1987) 1535–1604. doi:10.1088/0741-3335/29/11/001.

[43] G. J. Pert, Self-generated magnetic fields in plasmas, Journal of Plasma Physics 18 (2) (1977) 227–241. doi:10.1017/s0022377800021024.

[44] A. L. Velikovich, J. L. Giuliani, S. T. Zalesak, Nernst thermomagnetic waves in magnetized high energy density plasmas, Physics of Plasmas 26 (11) (Nov. 2019). doi:10.1063/1.5122178.

[45] K. Behnia, H. Aubin, Nernst effect in metals and superconductors: a review of concepts and experiments, Reports on Progress in Physics 79 (4) (2016) 046502. doi:10.1088/0034-4885/79/4/046502.

[46] D. A. Tidman, R. A. Shanny, Field-generating thermal instability in laser-heated plasmas, The Physics of Fluids 17 (6) (1974) 1207–1210. doi:10.1063/1.1694866.

[47] J. J. Bissell, C. P. Ridgers, R. J. Kingham, Field compressing magnetothermal instability in laser plasmas, Physical Review Letters 105 (17) (2010) 175001. doi:10.1103/physrevlett.105.175001.

[48] J. R. Davies, M. Fajardo, M. Kozlová, T. Mocek, et al., Filamented plasmas in laser ablation of solids, Plasma Physics and Controlled Fusion 51 (3) (2009) 035013. doi:10.1088/0741-3335/51/3/035013.

[49] M. Fatenejad, A. Bell, A. Benuzzi-Mounaix, R. Crowston, et al., Modeling HEDLA magnetic field generation experiments on laser facilities, High Energy Density Physics 9 (1) (2013) 172–177. doi:10.1016/j.hedp.2012.11.002.

[50] J. Nikl, M. Kuchařík, S. Weber, High-order curvilinear finite element magneto-hydrodynamics I: A conservative Lagrangian scheme, Journal of Computational Physics 464 (2022) 111158. doi:10.1016/j.jcp.2022.111158.

[51] MFEM: Modular finite element methods library (2023).
URL https://mfem.org/

[52] J. Nikl, M. Kuchařík, S. Weber, Self-generated magnetic fields modelling within high-order lagrangianmagneto-hydrodynamics, in: Europhysics Conference Abstracts – 47th EPS Conference on Plasma Physics, European PhysicalSociety, 2021.

[53] H. Brysk, Electron-ion equilibration in a partially degenerate plasma, Plasma Physics 16 (10) (1974) 927–932. doi:10.1088/0032-1028/16/10/005.

[54] K. Eidmann, J. M. ter Vehn, T. Schlegel, S. Hüller, Hydrodynamic simulation of subpicosecond laser interaction with solid-density matter, Physical Review E 62 (1) (2000) 1202–1214. doi:10.1103/physreve.62.1202.

[55] K. Jach, T. Pisarczyk, W. Stępniewski, R. Świerczyński, et al., 2D MHD simulation of spontaneous magnetic fields generated during interaction of 1315.2-nm laser radiation with copper slabs at $10^{16}$ $\mathrm{W\,cm^{-2}}$, Physics of Plasmas 28 (9) (2021) 092704. doi:10.1063/5.0054283.

[56] V. Bychenkov, V. Silin, S. Uryupin, Ion-acoustic turbulence and anomalous transport, Physics Reports 164 (3) (1988) 119–215. doi:10.1016/0370-1573(90)90122-i.

[57] A. B. Langdon, Nonlinear inverse bremsstrahlung and heated-electron distributions, Physical Review Letters 44 (9) (1980) 575–579. doi:10.1103/physrevlett.44.575.

[58] P. Gibbon, Short Pulse Laser Interactions with Matter, World Scientific Publishing Company, 2005. doi:10.1142/p116.

[59] T. Pisarczyk, S. Y. Gus'kov, T. Chodukowski, R. Dudzak, et al., Kinetic magnetization by fast electrons in laser-produced plasmas at sub-relativistic intensities, Physics of Plasmas 24 (10) (2017) 102711. doi:10.1063/1.4995044.

[60] T. Pisarczyk, S. Gus'kov, R. Dudzak, O. Renner, et al., Wavelength dependence of laser plasma interaction related to shock ignition approach, Laser and Particle Beams 36 (3) (2018) 405–426. doi:10.1017/s0263034618000447.

[61] K. Jungwirth, A. Cejnarova, L. Juha, B. Kralikova, et al., The Prague Asterix Laser System, Physics of Plasmas 8 (5) (2001) 2495–2501. doi:10.1063/1.1350569.